Diversity systems for mobile communication in a large room

tu/e
Research Report
ISSN 0167-9708
Coden: TEUEDE

Eindhoven
University of Technology
Netherlands

Faculty of Electrical Engineering

Diversity Systems for Mobile Communication in a Large Room

by
G. Dolmans

EUT Report 96-E-297
ISBN 90-6144-297-4
March 1996

Eindhoven University of Technology Research Reports
EINDHOVEN UNIVERSITY OF TECHNOLOGY

Faculty of Electrical Engineering
Eindhoven The Netherlands

ISSN 0167-9708 Coden: TEUEDE

Diversity Systems for Mobile Communication in a Large Room

by

G. Dolmans

EUT Report 96-E-297
ISBN 90-6144-297-4

EINDHOVEN
MARCH 1996

CIP-DATA KONINKLIJKE BIBLIOTHEEK, DEN HAAG

Dolmans, G.

Diversity systems for mobile communication in a large room /
by G. Dolmans. - Eindhoven : Eindhoven University of
Technology, Faculty of Electrical Engineering. - Fig.,
tab. - (EUT report / Eindhoven University of Technology,
Faculty of Electrical Engineering, ISSN 0167-9708 ; 96-E-297)
With ref.
ISBN 90-6144-297-4
NUGI 832
Subject headings: mobile radio systems / indoor radio /
diversity reception.

Diversity systems for mobile communication in a large room

G. Dolmans

Abstract

In this report, wave propagation inside a perfectly conducting room with two homogeneous dielectric walls has been studied. The thicknesses and losses of the dielectric walls are arbitrary, therefore it is possible to model wave phenomena inside various indoor environments. Green's function technique is used to calculate the electric fields excited by point sources and half wave dipole transmitters. In order to design an optimal receiver, the interaction between the electromagnetic fields and the receiving antenna must be modelled. The Lorentz reciprocity theorem is used to predict the received voltage, which depends on the location of the receiver inside the room.

The fluctuations of the received voltages inside the room can be reduced by using diversity techniques. Switching diversity, selection diversity, equal gain combining and maximal ratio combining have been compared to each other. Finally, the signal-to-noise ratio and the bit error rate of a DECT receiver have been presented.

Keywords: mobile radio systems / radiowave propagation / indoor radio / diversity reception

Dolmans, G.
DIVERSITY SYSTEMS FOR MOBILE COMMUNICATION IN A LARGE ROOM.
Eindhoven: Eindhoven University of Technology, Faculty of Electrical Engineering,
The Netherlands, 1996.
EUT Report 96-E-297, ISBN 90-6144-297-4

Address of the author
Department of Electromagnetics
Faculty of Electrical Engineering, Eindhoven University of Technology, EH 6.27
P.O. Box 513
5600 MB Eindhoven
The Netherlands
E-mail: G.Dolmans@em.ele.tue.nl

Acknowledgements

This research was supported by Philips Research Laboratories. The author wishes to thank Dr. M. Jeuken and Ir. L. Leyten for the helpful discussions.

Contents

Chapter 1

Introduction

Inventions such as radio, television and telephones have a great impact on the lives of people. The continuous growth of information generates a need for communication devices usable at every place and each moment. One way of providing in these communication services is to use a mobile radio system. Mobile radio is one of the great successes in recent years and there is a constant need for sophisticated equipment and services.

In this report, the fundamental processes of wave propagation inside a room will be discussed. In such a configuration, a variable signal level will be received by the mobile radio unit. It is important to study the electromagnetic fields inside a room in order to obtain a better understanding of the problems that can arise. It is not sufficient to study electromagnetic fields only, because the received signal depends on the type of receiving antenna also. Therefore, a Thévenin representation is used for modelling the interaction between the electromagnetic fields and the receiving antenna. The received voltage at the port of the antenna is obtained by using the Lorentz reciprocity theorem. The electromagnetic fields and the received voltage depend strongly on the location of the receiver inside the room.

The maximum errorless rate of data transmission over a mobile radio channel is determined by the amount of thermal noise. The signal-to-noise ratio can be calculated from the absolute value of the received voltage and the noise power levels. The probability of error (digital transmission) depends on the signal-to-noise ratio of the telecommunication link. The bit error rate of a DECT (Digital European Cordless Telephone) receiver as a function of the position inside the room is presented in this report.

The structure of this report is as follows:

In chapter two, the Green's function technique has been used for modelling the electromagnetic fields in a room with two lossy, dielectric walls. The properties of the dielectric walls can be changed, which can be used to study the scattering and absorption of electromagnetic waves at various material interfaces (for example concrete walls or walls made out of bricks). Green's functions are solutions of the electromagnetic fields caused by a point source, subjected to boundary conditions. The Green's functions for this configuration are described by double series. The infinite series have to be replaced by partial sums for calculating the electromagnetic fields on a computer. An estimate is given for the accuracy of the fields. It is shown that the computational time is independent of one dimension of the room. This means that propagation in a large room can be calculated very efficiently with the presented Green's function. The point source is not the only transmitter that has been analysed, in section 2.6 the electromagnetic fields caused by a half wave dipole antenna are discussed.

The interaction between the electromagnetic field and the receiving antenna is described in section 2.7. For this purpose, a Thévenin representation of the receiving antenna is obtained by using the Lorentz reciprocity theorem. The antenna is modelled as an accessible port for which a voltage and a current is defined in the network sense. The received voltage is calculated analytically for a half wave dipole receiver, which improves the required computational speed of the calculations. A measure of performance is given by the signal-to-noise ratio at the receiver output. The signal-to-noise ratio is calculated from the signal power absorbed in the load of the antenna and the noise power level. The bit error rate of a DECT (Digital European Cordless Telephone) receiver depends on the signal-to-noise ratio. The probability of error of this receiver is presented in section 2.7.3.

In chapter three, the electric fields, the received voltages, the signal- to-noise ratios and bit error rates for various configurations are presented. In section 3.2, it is shown that the electromagnetic field caused by a point source vanish at some points in the room. The electromagnetic field inside a room with two dielectric walls is compared to the field levels inside a perfectly conducting room. Furthermore, the electromagnetic field generated by a half-wave dipole antenna is analysed in section 3.3. The electromagnetic fields and the received voltage (section 3.4) for the two types of sources are very irregular inside the room. In section 3.5, methods for reducing these signal fluctuations are considered to obtain acceptable transmission of data, speech or other services. The effect of fading is reduced by transmitting a signal from a single antenna to a number of receiving antennas. This kind of diversity is called space-diversity reception.

Four space diversity receivers are described; switch diversity, selection diversity, equal gain combining and maximal ratio combining. The gains obtained by the four diversity receivers are compared to the conventional half-wave dipole receiver. The maximal ratio combiner gives the greatest improvement in received signal power. Switch diversity yields the slightest improvement in performance; however, this diversity technique is easy to implement.

Finally, the signal-to-noise ratio of a DECT receiver inside a large room is presented in section 3.7.

Chapter 2

Green's functions of a perfectly conducting room with two dielectric walls

2.1 Introduction

In [Dolmans 95], wave propagation inside a perfectly conducting room has been studied. As a first step, the transmitting antenna was modelled by a point-source. The electromagnetic fields transmitted by a point-source are described by Green's functions. It is shown in [Dolmans 95] that the Green's functions of a rectangular perfectly conducting room consist of double series. In [Kant 94], Green's functions for a perfectly conducting room with one lossy, dielectric wall have been described.

In this chapter, the concept of [Kant 94] will be used to obtain the Green's functions of a perfectly conducting room with two dielectric walls. It will be shown that the Green's functions for this configuration are again described by double series. These infinite series are replaced by partial sums for implementation on a computer. An estimate is given for the accuracy of the electromagnetic fields (calculated with the partial sums). Also, some error estimates for various configurations are presented in section 2.5.

In practice, dipole antennas are often used as transmitting or receiving devices for indoor telecommunication links. The electromagnetic fields generated by an antenna are obtained by performing an integration of the Green's functions weighted by the surface currents on the antenna. In section 2.6, these electromagnetic fields are calculated analytically which will improve the computational speed of the calculations.

The signal-to-noise ratio and the bit error rate are important parameters for characterizing the quality of an indoor telecommunication link. The bit error rate depends on the signal-to-noise ratio (influenced by the modulation scheme and the error coding). The signal-to-noise ratio can be calculated when the noise temperature, noise bandwidth and the port voltage at the receiving antenna are known. The receiving port voltage is a function of the electromagnetic fields inside the room, but also depends on the type of used antenna system. The interaction between an antenna system and the irregular indoor fields is an important issue which will be extensively studied in this report. In section 2.7, a Thévenin representation of a receiving antenna is given by using the Lorentz reciprocity theorem. Using this Thévenin representation, the port voltage of a half-wave dipole is calculated analytically.

2.2 Model description

The geometry of a perfectly conducting room with two dielectric walls is shown in figure 2.1 and figure 2.2 along with the used notation.

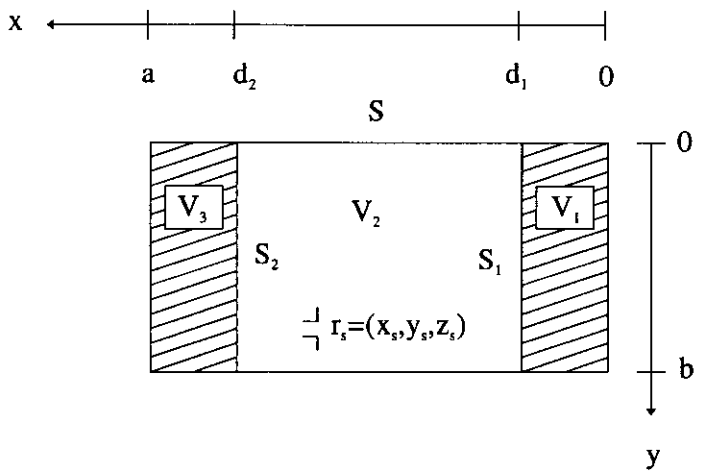

Figure 2.1: *Top-view of room*

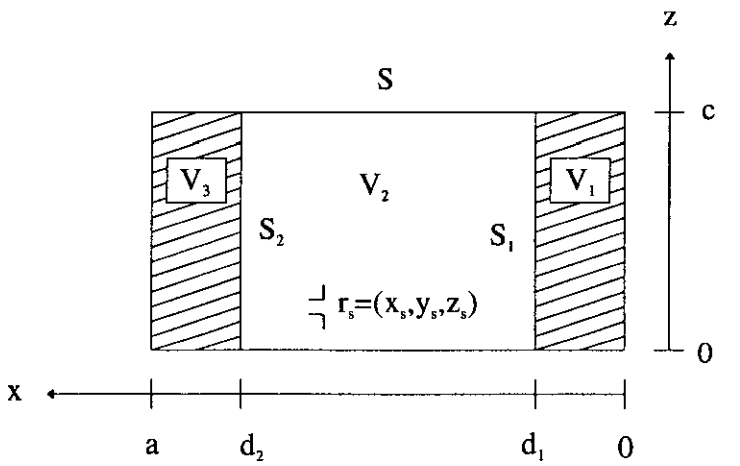

Figure 2.2: *Side-view of room*

The dimensions of the room in the $x-$, $y-$ and $z-$ directions are denoted by a, b and c, respectively. The boundary S is made of perfectly electric conducting walls ($\sigma \rightarrow \infty$). The volumes V_1 (enclosed by S_1 and S) and V_3 (enclosed by S_2 and S), consist of lossy dielectric material. The volume V_2 (enclosed by S, S_1 and S_2), which occupies the largest amount of space, consists of free space.

The volumes are described by the following mathematical expressions:

$$V_1 := \{\vec{r} \in \mathbb{R}^3 \,|\, 0 < x < d_1,\ 0 < y < b,\ 0 < z < c\},$$

$$V_2 := \{\vec{r} \in \mathbb{R}^3 \,|\, d_1 < x < d_2,\ 0 < y < b,\ 0 < z < c\},$$

$$V_3 := \{\vec{r} \in \mathbb{R}^3 \,|\, d_2 < x < a,\ 0 < y < b,\ 0 < z < c\}.$$

The first dielectric wall is bounded by the surfaces S and S_1, the thickness of the wall is denoted by d_1. The second dielectric wall is bounded by the surfaces S and S_2 and the thickness of this wall is given by $a - d_2$. The normal unit $\vec{n}$ to the surface S is oriented away from the volumes V_i. The normal unit $\vec{n}$ to the surfaces S_1 and S_2 is directed to the dielectric walls.

In a future publication, the Green's functions of another configuration (two rooms divided by a dielectric wall) will be analysed. Therefore, three permittivities will be used for the description of the three layers. In this way, the analysis for the two configurations can be constructed using the same procedures. Furthermore, the results can be compared to the results described in [Dolmans 95] and [Kant 94] more easily.

The permittivities of the three regions are given by

$$\varepsilon(\vec{r}) = \begin{cases} \varepsilon_1 = \varepsilon_1' - j\varepsilon_1'', & \vec{r} \in V_1, \\ \varepsilon_2 = \varepsilon_2' - j\varepsilon_2'', & \vec{r} \in V_2, \\ \varepsilon_3 = \varepsilon_3' - j\varepsilon_3'', & \vec{r} \in V_3. \end{cases} \tag{2.1}$$

The permeabilities of the three regions are presented by

$$\mu(\vec{r}) = \begin{cases} \mu_1 = \mu_1' - j\mu_1'', & \vec{r} \in V_1, \\ \mu_2 = \mu_2' - j\mu_2'', & \vec{r} \in V_2, \\ \mu_3 = \mu_3' - j\mu_3'', & \vec{r} \in V_3. \end{cases} \tag{2.2}$$

The coordinates of the source, which is located in volume V_2, are given by $\vec{r}_s = (x_s, y_s, z_s)$.

2.3 The magnetic vector potential

The electric field $\vec{E}(\vec{r})$ and the magnetic field $\vec{H}(\vec{r})$ satisfy Maxwell's equations:

$$\nabla \times \vec{E}_i(\vec{r}) = -j\omega\mu_i\vec{H}_i(\vec{r}), \qquad \vec{r} \in V_i, \tag{2.3}$$

$$\nabla \times \vec{H}_i(\vec{r}) = j\omega\varepsilon_i\vec{E}_i(\vec{r}) + \vec{J}_e(\vec{r}), \qquad \vec{r} \in V_i, \tag{2.4}$$

$$\nabla \cdot \varepsilon_i\vec{E}_i(\vec{r}) = \rho_e(\vec{r}), \qquad \vec{r} \in V_i, \tag{2.5}$$

$$\nabla \cdot \mu_i\vec{H}_i(\vec{r}) = 0, \qquad \vec{r} \in V_i, \tag{2.6}$$

where i =1,2,3. The electric charge density and the electric current density are denoted by the symbols ρ_e and $\vec{J}_e$, respectively. Furthermore, a harmonic time dependence of the form $e^{j\omega t}$ is assumed, where ω is the angular frequency.

The vector wave equations are obtained by taking the curl of equation (2.3) and substitution in (2.4):

$$\begin{aligned}
&\nabla \times \nabla \times \vec{E}_1(\vec{r}) - k_1^2 \vec{E}_1(\vec{r}) = \vec{0}, \\
&\nabla \times \nabla \times \vec{E}_2(\vec{r}) - k_2^2 \vec{E}_2(\vec{r}) = -j\omega\mu_2 \vec{J}_e(\vec{r}), \\
&\nabla \times \nabla \times \vec{E}_3(\vec{r}) - k_3^2 \vec{E}_3(\vec{r}) = \vec{0},
\end{aligned} \tag{2.7}$$

where $k_i = \omega\sqrt{\epsilon_i \mu_i}$ denotes the wave number of the region i. The boundary conditions for the perfect conductors are given by:

$$\vec{n} \times \vec{E}_i(\vec{r}) = \vec{0}, \qquad \vec{r} \in S, \qquad (i = 1, 2, 3). \tag{2.8}$$

The electromagnetic fields at the intersection of the volumes V_i satisfy the following relationships:

$$\vec{n} \times \begin{Bmatrix} \vec{E}_1(\vec{r}) \\ \vec{H}_1(\vec{r}) \end{Bmatrix} = \vec{n} \times \begin{Bmatrix} \vec{E}_2(\vec{r}) \\ \vec{H}_2(\vec{r}) \end{Bmatrix}, \qquad \vec{r} \in S_1, \tag{2.9}$$

$$\vec{n} \times \begin{Bmatrix} \vec{E}_2(\vec{r}) \\ \vec{H}_2(\vec{r}) \end{Bmatrix} = \vec{n} \times \begin{Bmatrix} \vec{E}_3(\vec{r}) \\ \vec{H}_3(\vec{r}) \end{Bmatrix}, \qquad \vec{r} \in S_2. \tag{2.10}$$

A magnetic vector potential is introduced to solve equations (2.7) - (2.10). Using $\nabla \cdot (\mu_i \vec{H}_i) = 0$, the magnetic fields can be written in terms of the magnetic vector potential $\vec{A}_i$

$$\vec{H}_i(\vec{r}) = \frac{1}{\mu_i} \nabla \times \vec{A}_i(\vec{r}). \tag{2.11}$$

The electric field is written in terms of the magnetic vector potential $\vec{A}_i$ and the scalar potential Φ_i by using (2.3) and (2.11)

$$\vec{E}_i(\vec{r}) = -j\omega \vec{A}_i - \nabla \Phi_i. \tag{2.12}$$

The scalar potential Φ_i can be related to the divergence of the vector potential $\vec{A}_i$ using the Lorentz gauge

$$\nabla \cdot \vec{A}_i = -j\omega \epsilon_i \mu_i \Phi_i. \tag{2.13}$$

Substituting the Lorentz gauge ([Harrington 61], p. 77) in equation (2.12) yields

$$\vec{E}_i(\vec{r}) = -j\omega \left[\vec{A}_i(\vec{r}) + \frac{1}{k_i^2} \nabla \nabla \cdot \vec{A}_i(\vec{r}) \right]. \tag{2.14}$$

Using the previous results, we may conclude that the electromagnetic fields can be obtained from the magnetic vector potential.

The vector potentials are solutions of the following partial differential equations:

$$\begin{aligned} \nabla^2\vec{A}_1(\vec{r}) + k_1^2\vec{A}_1(\vec{r}) &= \vec{0}, && \vec{r} \in V_1, \\ \nabla^2\vec{A}_2(\vec{r}) + k_2^2\vec{A}_2(\vec{r}) &= -\mu_2\vec{J}_e(\vec{r}), && \vec{r} \in V_2, \\ \nabla^2\vec{A}_3(\vec{r}) + k_3^2\vec{A}_3(\vec{r}) &= \vec{0}, && \vec{r} \in V_3. \end{aligned} \tag{2.15}$$

In the remainder of this section, the vector potentials will be solved for arbitrary directed electric point-sources. The point-sources are located at the coordinates $\vec{r}_s = (x_s, y_s, z_s)$ inside region two.

The vector potential can be expressed in terms of the dyadic Green's function $\bar{\bar{G}}_A(\vec{r}, \vec{r}_s)$

$$\vec{A}_i(\vec{r}) = \int\int\int \bar{\bar{G}}_{Ai}(\vec{r}, \vec{r}_s) \cdot \vec{J}_e(\vec{r}_s) dV_s, \tag{2.16}$$

where V_s is a volume that encloses the source current. In general, the dyadic Green's function can be written in the following form:

$$\bar{\bar{G}}_{Ai} = \begin{bmatrix} G_{Aixx} & G_{Aixy} & G_{Aixz} \\ G_{Aiyx} & G_{Aiyy} & G_{Aiyz} \\ G_{Aizx} & G_{Aizy} & G_{Aizz} \end{bmatrix}. \tag{2.17}$$

For our configuration, not all of the components of the Green's dyad are needed to calculate the electromagnetic field. In case the transmitter is a x-directed point-source (perpendicular directed to the dielectric walls), only one component of the vector potential is needed to solve the set of differential equations. For point-sources directed along the dielectric walls, two components of the vector potential are necessary to solve the Helmholtz equations for this configuration. Therefore, these two cases will be described separately in this chapter. The dyad can be expressed as:

$$\bar{\bar{G}}_{Ai} = \begin{bmatrix} G_{Aixx} & G_{Aixy} & G_{Aixz} \\ 0 & G_{Aiyy} & 0 \\ 0 & 0 & G_{Aizz} \end{bmatrix}. \tag{2.18}$$

case 1: electric source in the x-direction

The volume current distribution for a x-directed dipole is given by

$$\vec{J}_e(\vec{r}) = \vec{e}_x \delta(x - x_s)\delta(y - y_s)\delta(z - z_s). \tag{2.19}$$

Only a single component of the vector potential is needed for a x-directed source; $\vec{A}_i(\vec{r}) = G_{Aixx}\vec{e}_x$.

Using the boundary condition for the perfectly conducting wall (2.8), the boundary conditions of the vector potentials are written as [Kant 94], [Sommerfeld 64]:

$$\begin{aligned} &G_{Aixx}(x,0,z)=0, && G_{Aixx}(x,b,z)=0,\\ &G_{Aixx}(x,y,0)=0, && G_{Aixx}(x,y,c)=0, \end{aligned} \tag{2.20}$$

$$\frac{\partial}{\partial x}G_{A1xx}(x,y,z)\Big|_{x=0}=0, \tag{2.21}$$

$$\frac{\partial}{\partial x}G_{A3xx}(x,y,z)\Big|_{x=a}=0. \tag{2.22}$$

with i=1,2,3. At the interfaces between the various materials, G_{Aixx} satisfies the following boundary conditions [Kant 94]:

$$\frac{1}{k_1^2}\frac{\partial}{\partial x}G_{A1xx}(x,y,z)\Big|_{x=d_1}=\frac{1}{k_2^2}\frac{\partial}{\partial x}G_{A2xx}(x,y,z)\Big|_{x=d_1}, \tag{2.23}$$

$$\frac{1}{k_2^2}\frac{\partial}{\partial x}G_{A2xx}(x,y,z)\Big|_{x=d_2}=\frac{1}{k_3^2}\frac{\partial}{\partial x}G_{A3xx}(x,y,z)\Big|_{x=d_2}, \tag{2.24}$$

$$\frac{1}{\mu_1}G_{A1xx}(d_1,y,z)=\frac{1}{\mu_2}G_{A2xx}(d_1,y,z), \tag{2.25}$$

$$\frac{1}{\mu_2}G_{A2xx}(d_2,y,z)=\frac{1}{\mu_3}G_{A3xx}(d_2,y,z). \tag{2.26}$$

As stated earlier, the assumption is made that the electromagnetic fields can be obtained from one component of the vector potential. This implies that the vector Helmholtz equations are reduced to scalar Helmholtz equations:

$$\nabla^2 G_{A1xx}(\vec{r},\vec{r}_s)+k_1^2 G_{A1xx}(\vec{r},\vec{r}_s)=0, \tag{2.27}$$

$$\nabla^2 G_{A2xx}(\vec{r},\vec{r}_s)+k_2^2 G_{A2xx}(\vec{r},\vec{r}_s)=-\mu_2\delta(x-x_s)\delta(y-y_s)\delta(z-z_s), \tag{2.28}$$

$$\nabla^2 G_{A3xx}(\vec{r},\vec{r}_s)+k_3^2 G_{A3xx}(\vec{r},\vec{r}_s)=0. \tag{2.29}$$

Equations (2.27) and (2.29) are homogeneous differential equations. Therefore, the solutions of these equations can be expressed as a linear combination of elementary functions. Using the theory of Fourier series and the boundary conditions (2.20) gives

$$G_{A1xx}=\sum_{m=1}^{\infty}\sum_{n=1}^{\infty}\sin(k_{ym}y)\sin(k_{zn}z)F_{1mn}(x), \tag{2.30}$$

$$G_{A3xx}=\sum_{m=1}^{\infty}\sum_{n=1}^{\infty}\sin(k_{ym}y)\sin(k_{zn}z)F_{3mn}(x), \tag{2.31}$$

where $k_{ym} = \frac{m\pi}{b}$ and $k_{zn} = \frac{n\pi}{c}$. A convenient way to solve the inhomogeneous equation (2.28) is to first look at the homogeneous solution:

$$G_{A2xx} = \sum_{m=1}^{\infty}\sum_{n=1}^{\infty} \sin(k_{ym}y)\sin(k_{zn}z)F_{2mn}(x). \tag{2.32}$$

The right-hand side of (2.28) can be written as a Fourier series [Morse 53]:

$$\begin{aligned} \delta(y - y_s) &= \sum_{m=1}^{\infty} A_m \sin(k_{ym}y), \qquad && y \in [0, b], \\ \delta(z - z_s) &= \sum_{n=1}^{\infty} B_n \sin(k_{zn}z), && z \in [0, c]. \end{aligned} \tag{2.33}$$

The coefficients A_m and B_n are found by solving the following orthogonality relationships:

$$\int_0^b \sin(\frac{n\pi}{b}y)\delta(y - y_s)dy = \sum_{m=1}^{\infty} A_m \int_0^b \sin(\frac{m\pi}{b}y)\sin(\frac{n\pi}{b}y)dy, \tag{2.34}$$

$$\int_0^c \sin(\frac{m\pi}{c}z)\delta(z - z_s)dz = \sum_{n=1}^{\infty} B_n \int_0^c \sin(\frac{m\pi}{c}z)\sin(\frac{n\pi}{c}z)dz. \tag{2.35}$$

The coefficients A_m and B_m are given by

$$A_m = \frac{2}{b}\sin(k_{ym}y_s), \qquad B_n = \frac{2}{c}\sin(k_{zn}z_s). \tag{2.36}$$

The source current is now expressed as

$$\delta(\vec{r} - \vec{r}_s) = \frac{4}{bc}\sum_{m=1}^{\infty}\sum_{n=1}^{\infty} \sin(k_{ym}y)\sin(k_{ym}y_s)\sin(k_{zn}z)\sin(k_{zn}z_s)\delta(x - x_s). \tag{2.37}$$

Substitution of (2.30) - (2.32) and (2.37) in equations (2.27) - (2.29) results in the following set of one-dimensional differential equations:

$$\frac{d^2}{dx^2}F_{1mn}(x) + k_{1x}^2 F_{1mn}(x) = 0, \tag{2.38}$$

$$\frac{d^2}{dx^2}F_{2mn}(x) + k_{2x}^2 F_{2mn}(x) = -\frac{4\mu_2}{bc}\sin(k_{ym}y_s)\sin(k_{zn}z_s)\delta(x - x_s), \tag{2.39}$$

$$\frac{d^2}{dx^2}F_{3mn}(x) + k_{3x}^2 F_{3mn}(x) = 0, \tag{2.40}$$

where $k_{1x} = \sqrt{k_1^2 - k_{ym}^2 - k_{zn}^2}$, $k_{2x} = \sqrt{k_2^2 - k_{ym}^2 - k_{zn}^2}$ and $k_{3x} = \sqrt{k_3^2 - k_{ym}^2 - k_{zn}^2}$.
The solutions of the inhomogeneous differential equation (2.39) will be divided into two parts:

$$F_{2mn}(x) = \begin{cases} F_{2mn}^1(x) & d_1 < x \le x_s \\ F_{2mn}^2(x) & x_s < x < d_2 \end{cases} \tag{2.41}$$

Using the boundary conditions for the vector potential (2.21) and (2.22), the solutions of (2.38) - (2.40) are linear combinations of elementary functions:

$$F_{1mn}(x) = A_{1mn}\cos(k_{1x}x), \tag{2.42}$$

$$F^1_{2mn}(x) = A^1_{2mn}\cos(k_{2x}(x-d_1)) + B^1_{2mn}\sin(k_{2x}(x-d_1)), \tag{2.43}$$

$$F^2_{2mn}(x) = A^2_{2mn}\cos(k_{2x}(x-d_2)) + B^2_{2mn}\sin(k_{2x}(x-d_2)), \tag{2.44}$$

$$F_{3mn}(x) = A_{3mn}\cos(k_{3x}(x-a)). \tag{2.45}$$

Note that four boundary conditions (2.23) - (2.26) are still unused. The two complementary boundary conditions, needed to solve the six unknowns in (2.42) - (2.45), are obtained from the differential equation (2.39). If $F_{2mn}(x)$ is a solution of (2.39), $F_{2mn}(x)$ has to be continuous at $x = x_s$. The derivative of $F_{2mn}(x)$ has a jump of size $-\frac{4\mu_2}{bc}\sin(k_{ym}y_s)\sin(k_{zn}z_s)$ at $x = x_s$. Therefore, the two boundary conditions at $x = x_s$ are given by:

$$F^1_{2mn}(x_s) = F^2_{2mn}(x_s), \tag{2.46}$$

$$\frac{d}{dx}F^1_{2mn}(x)\bigg|_{x=x_s} - \frac{d}{dx}F^2_{2mn}(x)\bigg|_{x=x_s} = -\frac{4\mu_2}{bc}\sin(k_{ym}y_s)\sin(k_{zn}z_s). \tag{2.47}$$

At this point, six boundary conditions are available for solving the six unknowns in (2.42) - (2.45). First, the boundary conditions of the dielectric interface at $x = d_1$ (equations (2.23) and (2.25)) will be used. Consequently, the following two equations are obtained:

$$\frac{1}{\mu_1}A_{1mn}\cos(k_{1x}d_1) = \frac{1}{\mu_2}A^1_{2mn}, \tag{2.48}$$

$$-\frac{k_{1x}}{k_1^2}A_{1mn}\sin(k_{1x}d_1) = \frac{k_{2x}}{k_2^2}B^1_{2mn}. \tag{2.49}$$

Substitution of (2.48) in (2.49) results in the following relationships between A^1_{2mn} and B^1_{2mn}:

$$B^1_{2mn} = \frac{Z_{1mn}}{k_{2x}}A^1_{2mn}, \tag{2.50}$$

where $Z_{1mn} = -\frac{\varepsilon_2 k_{1x}}{\varepsilon_1}\tan(k_{1x}d_1)$. The solution for A_{1mn} can be obtained from

$$A_{1mn} = \frac{\mu_1}{\mu_2\cos(k_{1x}d_1)}A^1_{2mn}. \tag{2.51}$$

The boundary conditions of the dielectric interface at $x = d_2$ (namely (2.24) and (2.26)) will be used:

$$\frac{1}{\mu_2}A^2_{2mn} = \frac{1}{\mu_3}A_{3mn}\cos(k_{3x}(d_2-a)), \tag{2.52}$$

$$-\frac{k_{3x}}{k_3^2}A_{3mn}\sin(k_{3x}(d_2-a)) = \frac{k_{2x}}{k_2^2}B^2_{2mn}. \tag{2.53}$$

Substitution of (2.52) in (2.53) gives

$$B^2_{2mn} = \frac{Z_{2mn}}{k_{2x}} A^2_{2mn}, \tag{2.54}$$

where $Z_{2mn} = -\frac{\varepsilon_2 k_{3x}}{\varepsilon_3} \tan(k_{3x}(d_2 - a))$. The solution for A_{3mn} is obtained from

$$A_{3mn} = \frac{\mu_3}{\mu_2} \frac{A^2_{2mn}}{\cos(k_{3x}(d_2 - a))}. \tag{2.55}$$

To obtain the relationships between the coefficients A^1_{2mn} and A^2_{2mn}, the boundary condition at $x = x_s$ (2.46) and equations (2.50), (2.54) will be used:

$$A^1_{2mn} = A^2_{2mn} \frac{k_{2x}\cos(k_{2x}(x_s - d_2)) + Z_{2mn}\sin(k_{2x}(x_s - d_2))}{k_{2x}\cos(k_{2x}(x_s - d_1)) + Z_{1mn}\sin(k_{2x}(x_s - d_1))}. \tag{2.56}$$

The second boundary condition at $x = x_s$ (2.47) and equations (2.50), (2.54) results in the second relationship between the coefficients A^1_{2mn} and A^2_{2mn}:

$$\begin{aligned} &A^1_{2mn}\left(-k_{2x}\sin(k_{2x}(x_s - d_1)) + Z_{1mn}\cos(k_{2x}(x_s - d_1))\right) = \\ &A^2_{2mn}\left(-k_{2x}\sin(k_{2x}(x_s - d_2)) + Z_{2mn}\cos(k_{2x}(x_s - d_2))\right) - \tfrac{4\mu_2}{bc}\sin(k_{ym}y_s)\sin(k_{zn}z_s). \end{aligned} \tag{2.57}$$

Elimination of A^1_{2mn} from (2.56) and (2.57) gives

$$A^2_{2mn} = -\frac{4\mu_2}{bc} \frac{\sin(k_{ym}y_s)\sin(k_{zn}z_s)\left[k_{2x}\cos(k_{2x}(x_s - d_1)) + Z_{1mn}\sin(k_{2x}(x_s - d_1))\right]}{\sin(k_{2x}(d_2 - d_1))(-k^2_{2x} - Z_{1mn}Z_{2mn}) + \cos(k_{2x}(d_2 - d_1))(k_{2x}Z_{1mn} - k_{2x}Z_{2mn})}. \tag{2.58}$$

The coefficient A^1_{2mn} is given by

$$A^1_{2mn} = -\frac{4\mu_2}{bc} \frac{\sin(k_{ym}y_s)\sin(k_{zn}z_s)\left[k_{2x}\cos(k_{2x}(x_s - d_2)) + Z_{2mn}\sin(k_{2x}(x_s - d_2))\right]}{\sin(k_{2x}(d_2 - d_1))(-k^2_{2x} - Z_{1mn}Z_{2mn}) + \cos(k_{2x}(d_2 - d_1))(k_{2x}Z_{1mn} - k_{2x}Z_{2mn})}. \tag{2.59}$$

All six coefficients (A_{1mn}, A^1_{2mn}, A^2_{2mn}, B^1_{2mn}, B^2_{2mn} and A_{3mn}) are given by the equations (2.50), (2.51), (2.54), (2.55), (2.58) and (2.59). The component G_{Aixx} of the Green's dyad can now be calculated:

Interval 1: $0 \le x \le d_1$

$$\begin{aligned} G_{A1xx} = -\frac{4\mu_1}{bc} \sum_{m=1}^{\infty}\sum_{n=1}^{\infty} &\sin(k_{ym}y)\sin(k_{ym}y_s)\sin(k_{zn}z)\sin(k_{zn}z_s)\cdot \\ &\frac{\cos(k_{1x}x)\left[k_{2x}\cos(k_{2x}(x_s - d_2)) + Z_{2mn}\sin(k_{2x}(x_s - d_2))\right]}{D_{mn}\cos(k_{1x}d_1)} \end{aligned} \tag{2.60}$$

Interval 2: $d_1 < x \leq x_s$

$$G^1_{A2xx} = -\frac{4\mu_2}{bc}\sum_{m=1}^{\infty}\sum_{n=1}^{\infty}\sin(k_{ym}y)\sin(k_{ym}y_s)\sin(k_{zn}z)\sin(k_{zn}z_s)\frac{1}{D_{mn}k_{2x}}\cdot$$
$$[\cos(k_{2x}(x_s-d_2))\,(k_{2x}^2\cos(k_{2x}(x-d_1)+k_{2x}Z_{1mn}\sin k_{2x}(x-d_1))+$$
$$\sin(k_{2x}(x_s-d_2))\,(k_{2x}Z_{2mn}\cos(k_{2x}(x-d_1))+Z_{1mn}Z_{2mn}\sin k_{2x}(x-d_1))] \tag{2.61}$$

Interval 3: $x_s < x \leq d_2$

$$G^2_{A2xx} = -\frac{4\mu_2}{bc}\sum_{m=1}^{\infty}\sum_{n=1}^{\infty}\sin(k_{ym}y)\sin(k_{ym}y_s)\sin(k_{zn}z)\sin(k_{zn}z_s)\frac{1}{D_{mn}k_{2x}}\cdot$$
$$[\cos(k_{2x}(x-d_2))\,(k_{2x}^2\cos(k_{2x}(x_s-d_1)+k_{2x}Z_{1mn}\sin k_{2x}(x_s-d_1))+$$
$$\sin(k_{2x}(x-d_2))\,(k_{2x}Z_{2mn}\cos(k_{2x}(x_s-d_1))+Z_{1mn}Z_{2mn}\sin k_{2x}(x_s-d_1))] \tag{2.62}$$

Interval 4: $d_2 < x \leq a$

$$G_{A3xx} = -\frac{4\mu_3}{bc}\sum_{m=1}^{\infty}\sum_{n=1}^{\infty}\sin(k_{ym}y)\sin(k_{ym}y_s)\sin(k_{zn}z)\sin(k_{zn}z_s)\cdot$$
$$\frac{\cos(k_{3x}(x-a))\,[Z_{1mn}\sin(k_{2x}(x_s-d_1))+k_{2x}\cos(k_{2x}(x_s-d_1))]}{D_{mn}\cos(k_{3x}(d_2-a))} \tag{2.63}$$

with

$$k_{1x} = \sqrt{k_1^2-(\tfrac{m\pi}{b})^2-(\tfrac{n\pi}{c})^2},$$
$$k_{2x} = \sqrt{k_2^2-(\tfrac{m\pi}{b})^2-(\tfrac{n\pi}{c})^2},$$
$$k_{3x} = \sqrt{k_3^2-(\tfrac{m\pi}{b})^2-(\tfrac{n\pi}{c})^2},$$
$$Z_{1mn} = -\tfrac{\varepsilon_2 k_{1x}}{\varepsilon_1}\tan(k_{1x}d_1), \tag{2.64}$$
$$Z_{2mn} = -\tfrac{\varepsilon_2 k_{3x}}{\varepsilon_3}\tan(k_{3x}(d_2-a)),$$
$$D_{mn} = \sin(k_{2x}(d_2-d_1))(-k_{2x}^2-Z_{1mn}Z_{2mn})+\cos(k_{2x}(d_2-d_1))(k_{2x}Z_{1mn}-k_{2x}Z_{2mn}).$$

At this moment, the solution for one of the five unknown components of the Green's dyad has been found. We will now consider the situation of a point-source directed parallel to the dielectric walls. For this case, it is not sufficient to use one component of the magnetic vector potential. Instead, two components of the vector potentials are needed to solve the Helmholtz equations and the boundary conditions.

case 2a: electric source in the z-direction

The electric current density of a z-directed point-source can be expressed as:

$$\vec{J}_e(\vec{r}) = \vec{e}_z \delta(x - x_s)\delta(y - y_s)\delta(z - z_s). \tag{2.65}$$

Using (2.16), the vector potential is now written as:

$$\vec{A}_i(\vec{r}) = \begin{bmatrix} G_{Aixz} \\ 0 \\ G_{Aizz} \end{bmatrix}. \tag{2.66}$$

The scalar Helmholtz equations for all components of the magnetic vector potential are given by

$$\nabla^2 G_{A1zz}(\vec{r},\vec{r}_s) + k_1^2 G_{A1zz}(\vec{r},\vec{r}_s) = 0, \tag{2.67}$$

$$\nabla^2 G_{A2zz}(\vec{r},\vec{r}_s) + k_2^2 G_{A2zz}(\vec{r},\vec{r}_s) = -\mu_2 \delta(x - x_s)\delta(y - y_s)\delta(z - z_s), \tag{2.68}$$

$$\nabla^2 G_{A3zz}(\vec{r},\vec{r}_s) + k_3^2 G_{A3zz}(\vec{r},\vec{r}_s) = 0, \tag{2.69}$$

$$\nabla^2 G_{A1xz}(\vec{r},\vec{r}_s) + k_1^2 G_{A1xz}(\vec{r},\vec{r}_s) = 0, \tag{2.70}$$

$$\nabla^2 G_{A2xz}(\vec{r},\vec{r}_s) + k_2^2 G_{A2xz}(\vec{r},\vec{r}_s) = 0, \tag{2.71}$$

$$\nabla^2 G_{A3xz}(\vec{r},\vec{r}_s) + k_3^2 G_{A3xz}(\vec{r},\vec{r}_s) = 0. \tag{2.72}$$

Two situations will be distinguished; A) solutions for G_{Aizz} and B) solutions for G_{Aixz}

A) Calculation of G_{Aizz}

In order to solve the set of differential equations (2.67) - (2.69), it is necessary to derive the boundary conditions for the magnetic vector potential. For this purpose, the relation between the electric field and the vector potential (2.14) is substituted in the boundary condition for the perfectly conducting walls (2.8). In this way, the boundary conditions for G_{Aizz} are obtained [Kant 94]

$$\begin{aligned}
&G_{Aizz}(x,0,z) = 0, && G_{Aizz}(x,b,z) = 0, && i = (1,2,3),\\
&\frac{\partial}{\partial z} G_{Aizz}(x,y,z) = 0\Big|_{z=0}, && \frac{\partial}{\partial z} G_{Aizz}(x,y,z) = 0\Big|_{z=c}, && i = (1,2,3),\\
&G_{A1zz}(0,y,z) = 0, && G_{A3zz}(a,y,z) = 0.
\end{aligned} \tag{2.73}$$

At the interfaces between the volumes V_i, the boundary conditions for G_{Aizz} are given by

$$G_{A1zz}(d_1, y, z) = G_{A2zz}(d_1, y, z), \tag{2.74}$$

$$G_{A3zz}(d_2, y, z) = G_{A2zz}(d_2, y, z), \tag{2.75}$$

$$\frac{1}{\mu_2}\frac{\partial}{\partial x}G_{A2zz}(x, y, z)\Big|_{x=d_1} = \frac{1}{\mu_1}\frac{\partial}{\partial x}G_{A1zz}(x, y, z)\Big|_{x=d_1}, \tag{2.76}$$

$$\frac{1}{\mu_2}\frac{\partial}{\partial x}G_{A2zz}(x, y, z)\Big|_{x=d_2} = \frac{1}{\mu_3}\frac{\partial}{\partial x}G_{A3zz}(x, y, z)\Big|_{x=d_2}. \tag{2.77}$$

The solution of (2.67) - (2.69) can be expressed as a linear combination of elementary functions:

$$G_{Aizz} = \sum_{m=1}^{\infty}\sum_{n=0}^{\infty} \sin(k_{ym}y)\cos(k_{zn}z)F_{imn}(x), \qquad i = (1,2,3). \tag{2.78}$$

Rewriting the right-hand side of (2.68) into a Fourier-series, the following set of one-dimensional differential equations is obtained

$$\frac{d^2}{dx^2}F_{1mn}(x) + k_{1x}^2 F_{1mn}(x) = 0, \tag{2.79}$$

$$\frac{d^2}{dx^2}F_{2mn}(x) + k_{2x}^2 F_{2mn}(x) = -\frac{2\mu_2\epsilon_{0n}}{bc}\sin(k_{ym}y_s)\cos(k_{zn}z_s)\delta(x - x_s), \tag{2.80}$$

$$\frac{d^2}{dx^2}F_{3mn}(x) + k_{3x}^2 F_{3mn}(x) = 0, \tag{2.81}$$

where ϵ_{0n} is called Neumann-factor. $\epsilon_{0n} = 1$ for $n = 0$ and $\epsilon_{0n} = 2$ for $n \neq 0$. The function $F_{2mn}(x)$ will again be divided into two parts; $F_{2mn}^1(x)$ for $d_1 < x \leq x_s$ and $F_{2mn}^2(x)$ for $x_s < x \leq d_2$. The solution of $F_{imn}^j(x)$ is given by

$$F_{1mn}(x) = A_{1mn}\sin(k_{1x}x), \tag{2.82}$$

$$F_{2mn}^1(x) = A_{2mn}^1\cos(k_{2x}(x - d_1)) + B_{2mn}^1\sin(k_{2x}(x - d_1)), \tag{2.83}$$

$$F_{2mn}^2(x) = A_{2mn}^2\cos(k_{2x}(x - d_2)) + B_{2mn}^2\sin(k_{2x}(x - d_2)), \tag{2.84}$$

$$F_{3mn}(x) = A_{3mn}\sin(k_{3x}(x - a)). \tag{2.85}$$

The two boundary conditions at $x = x_s$ are given by:

$$F_{2mn}^1(x_s) = F_{2mn}^2(x_s), \tag{2.86}$$

$$\frac{d}{dx}F_{2mn}^1(x)\Big|_{x=x_s} - \frac{d}{dx}F_{2mn}^2(x)\Big|_{x=x_s} = -\frac{2\epsilon_{0n}\mu_2}{bc}\sin(k_{ym}y_s)\cos(k_{zn}z_s). \tag{2.87}$$

Six boundary conditions (namely (2.74) - (2.77), (2.86) and (2.87)) are available for solving the equations (2.82) - (2.85).

The procedure for solving the linear equations is essentially the same as described in case 1 (electric source in the x-direction), therefore it will not be repeated here. The component G_{Aizz} is given by

Interval 1: $0 \leq x \leq d_1$

$$G_{A1zz} = -\frac{2\mu_2}{bc} \sum_{m=1}^{\infty} \sum_{n=0}^{\infty} \epsilon_{0n} \sin(k_{ym}y) \sin(k_{ym}y_s) \cos(k_{zn}z) \cos(k_{zn}z_s) \cdot \frac{Y_{1mn} \sin(k_{1x}x) \left[k_{2x}Y_{2mn} \cos(k_{2x}(x_s - d_2)) + \sin(k_{2x}(x_s - d_2))\right]}{J_{mn} \sin(k_{1x}d_1)} \tag{2.88}$$

Interval 2: $d_1 < x \leq x_s$

$$G^1_{A2zz} = -\frac{2\mu_2}{bc} \sum_{m=1}^{\infty} \sum_{n=0}^{\infty} \epsilon_{0n} \sin(k_{ym}y) \sin(k_{ym}y_s) \cos(k_{zn}z) \cos(k_{zn}z_s) \frac{1}{J_{mn}k_{2x}} \cdot \left[k_{2x}Y_{1mn} \cos(k_{2x}(x - d_1)) + \sin(k_{2x}(x - d_1))\right] \cdot \left[\sin(k_{2x}(x_s - d_2)) + k_{2x}Y_{2mn} \cos(k_{2x}(x_s - d_2))\right] \tag{2.89}$$

Interval 3: $x_s < x \leq d_2$

$$G^2_{A2zz} = -\frac{2\mu_2}{bc} \sum_{m=1}^{\infty} \sum_{n=0}^{\infty} \epsilon_{0n} \sin(k_{ym}y) \sin(k_{ym}y_s) \cos(k_{zn}z) \cos(k_{zn}z_s) \frac{1}{J_{mn}k_{2x}} \cdot \left[k_{2x}Y_{2mn} \cos(k_{2x}(x - d_2)) + \sin(k_{2x}(x - d_2))\right] \cdot \left[\sin(k_{2x}(x_s - d_1)) + k_{2x}Y_{1mn} \cos(k_{2x}(x_s - d_1))\right] \tag{2.90}$$

Interval 4: $d_2 < x \leq a$

$$G_{A3zz} = -\frac{2\mu_2}{bc} \sum_{m=1}^{\infty} \sum_{n=0}^{\infty} \epsilon_{0n} \sin(k_{ym}y) \sin(k_{ym}y_s) \cos(k_{zn}z) \cos(k_{zn}z_s) \cdot \frac{Y_{2mn} \sin(k_{3x}(x - a)) \left[\sin(k_{2x}(x_s - d_1)) + k_{2x}Y_{1mn} \cos(k_{2x}(x_s - d_1))\right]}{J_{mn} \sin(k_{3x}(d_2 - a))} \tag{2.91}$$

with

$$
\begin{aligned}
k_{1x} &= \sqrt{k_1^2 - \left(\tfrac{m\pi}{b}\right)^2 - \left(\tfrac{n\pi}{c}\right)^2}, \\
k_{2x} &= \sqrt{k_2^2 - \left(\tfrac{m\pi}{b}\right)^2 - \left(\tfrac{n\pi}{c}\right)^2}, \\
k_{3x} &= \sqrt{k_3^2 - \left(\tfrac{m\pi}{b}\right)^2 - \left(\tfrac{n\pi}{c}\right)^2}. \\
Y_{1mn} &= \tfrac{\mu_1}{\mu_2 k_{1x}} \tan(k_{1x} d_1), \\
Y_{2mn} &= \tfrac{\mu_3}{\mu_2 k_{3x}} \tan(k_{3x}(d_2 - a)), \\
J_{mn} &= \cos(k_{2x}(d_2 - d_1))(k_{2x} Y_{2mn} - k_{2x} Y_{1mn}) - \sin(k_{2x}(d_2 - d_1))(1 + k_{2x}^2 Y_{1mn} Y_{2mn}).
\end{aligned}
\tag{2.92}
$$

B) Calculation of G_{Aixz}

The magnetic vector potential G_{Aixz} will now be calculated in order to complete the analysis for a z-directed current source. The boundary conditions for G_{Aixz} are obtained by combining (2.14) with (2.8) - (2.10). Note that the differential equations for G_{Aixz} are homogeneous, this means that no boundary conditions are needed at $x = x_s$. The boundary conditions for G_{Aixz} at the perfectly conducting walls are given by [Kant 94]

$$
\begin{aligned}
&G_{Aixz}(x,0,z) = 0, && G_{Aixz}(x,b,z) = 0, && i = (1,2,3), \\
&G_{Aixz}(x,y,0) = 0, && G_{Aixz}(x,y,c) = 0, && i = (1,2,3), \\
&\frac{\partial}{\partial x} G_{A1xz}(x,y,z) = 0\Big|_{x=0}, && \frac{\partial}{\partial x} G_{A3xz}(x,y,z) = 0\Big|_{x=a}.
\end{aligned}
\tag{2.93}
$$

At the dielectric interfaces, the boundary conditions for G_{Aixz} are expressed as

$$
\frac{1}{\mu_2} G_{A2xz}(d_1,y,z) = \frac{1}{\mu_1} G_{A1xz}(d_1,y,z), \tag{2.94}
$$

$$
\frac{1}{\mu_2} G_{A2xz}(d_2,y,z) = \frac{1}{\mu_3} G_{A3xz}(d_2,y,z), \tag{2.95}
$$

$$
\begin{aligned}
&\frac{1}{k_2^2} \frac{\partial}{\partial x} G_{A2xz}(x,y,z)\Big|_{x=d_1} - \frac{1}{k_1^2} \frac{\partial}{\partial x} G_{A1xz}(x,y,z)\Big|_{x=d_1} = \\
&\left(\frac{1}{k_1^2} - \frac{1}{k_2^2}\right) \frac{\partial}{\partial z} G_{A2zz}(x,y,d_1),
\end{aligned}
\tag{2.96}
$$

$$
\begin{aligned}
&\frac{1}{k_3^2} \frac{\partial}{\partial x} G_{A3xz}(x,y,z)\Big|_{x=d_2} - \frac{1}{k_2^2} \frac{\partial}{\partial x} G_{A2xz}(x,y,z)\Big|_{x=d_2} = \\
&\left(\frac{1}{k_2^2} - \frac{1}{k_3^2}\right) \frac{\partial}{\partial z} G_{A3zz}(x,y,d_2).
\end{aligned}
\tag{2.97}
$$

Notice that the equations (2.96) and (2.97) relate the vector potential G_{Aixz} to the vector potential G_{Aizz}. Therefore, the results obtained in the previous sections will be used to calculate the potential G_{Aixz}. The solution of (2.70) - (2.72) is expressed as a Fourier series:

$$G_{Aixz} = \sum_{m=1}^{\infty}\sum_{n=1}^{\infty} \sin(k_{ym}y)\sin(k_{zn}z)F_{imn}(x). \tag{2.98}$$

Using the boundary conditions (2.93), $F_{imn}(x)$ is given by

$$F_{1mn}(x) = A_{1mn}\cos(k_{1x}x), \tag{2.99}$$

$$F_{2mn}(x) = A_{2mn}\cos(k_{2x}(x-d_2)) + B_{2mn}\sin(k_{2x}(x-d_2)), \tag{2.100}$$

$$F_{3mn}(x) = A_{3mn}\cos(k_{3x}(x-a)). \tag{2.101}$$

Notice that $F_{imn}(x)$ consists of three parts (instead of four parts in the previous analysis) due to the fact that $F_{imn}(x)$ results from homogeneous differential equations. Four boundary conditions (2.94) - (2.97) are available for solving the equations (2.99) - (2.101). The final expressions for G_{Aixz} are given by

Interval 1: $0 \le x \le d_1$

$$\begin{aligned} G_{A1xz} = {} & \frac{4\mu_1}{bc}\sum_{m=1}^{\infty}\sum_{n=1}^{\infty}\frac{n\pi}{c}\sin(k_{ym}y)\sin(k_{ym}y_s)\sin(k_{zn}z)\cos(k_{zn}z_s)\cos(k_{1x}x)\frac{1}{K_{mn}}\cdot \\ & [(k_2^2-k_1^2)M_{mn}\,[k_{2x}k_3^2\mu_2\cos(k_{3x}(d_2-a))\cos(k_{2x}(d_1-d_2)) \\ & -k_{3x}k_2^2\mu_3\sin(k_{3x}(d_2-a))\sin(k_{2x}(d_1-d_2))] + \\ & (k_3^2-k_2^2)\mu_2 L_{mn}\cos(k_{3x}(d_2-a))k_{2x}k_1^2\mu_2] \end{aligned} \tag{2.102}$$

Interval 2: $d_1 < x \le d_2$

$$\begin{aligned} G_{A2xz} = {} & \frac{4\mu_2}{bc}\sum_{m=1}^{\infty}\sum_{n=1}^{\infty}\frac{n\pi}{c}\sin(k_{ym}y)\sin(k_{ym}y_s)\sin(k_{zn}z)\cos(k_{zn}z_s)\frac{1}{K_{mn}}\cdot \\ & [(k_2^2-k_1^2)M_{mn}\cos(k_{1x}d_1)\,[k_{2x}k_3^2\mu_2\cos(k_{3x}(d_2-a))\cos(k_{2x}(x-d_2)) \\ & -k_{3x}k_2^2\mu_3\sin(k_{3x}(d_2-a))\sin(k_{2x}(x-d_2))] \\ & +(k_3^2-k_2^2)L_{mn}\mu_2\cos(k_{3x}(d_2-a))\,[k_{1x}k_2^2\mu_1\sin(k_{1x}d_1)\sin(k_{2x}(d_1-x)) \\ & +k_{2x}k_1^2\mu_2\cos(k_{1x}d_1)\cos(k_{2x}(d_1-x))]] \end{aligned} \tag{2.103}$$

Interval 3: $d_2 < x \leq a$

$$
\begin{aligned}
&G_{A3xz} = \frac{4\mu_3}{bc} \sum_{m=1}^{\infty} \sum_{n=1}^{\infty} \frac{n\pi}{c} \sin(k_{ym} y) \sin(k_{ym} y_s) \sin(k_{zn} z) \cos(k_{zn} z_s) \cos(k_{3x}(x-a)) \frac{1}{K_{mn}} \cdot \\
&[(k_2^2 - k_1^2) M_{mn} k_{2x} k_3^2 \mu_2 \cos(k_{1x} d_1) \\
&+(k_3^2 - k_2^2) L_{mn} \mu_2 \left[k_{1x} k_2^2 \mu_1 \sin(k_{1x} d_1) \sin(k_{2x}(d_1 - d_2)) \right. \\
&\left. +k_{2x} k_1^2 \mu_2 \cos(k_{1x} d_1) \cos(k_{2x}(d_1 - d_2))\right]]
\end{aligned}
\tag{2.104}
$$

with

$$
\begin{aligned}
k_{1x} &= \sqrt{k_1^2 - \left(\tfrac{m\pi}{b}\right)^2 - \left(\tfrac{n\pi}{c}\right)^2}, \\
k_{2x} &= \sqrt{k_2^2 - \left(\tfrac{m\pi}{b}\right)^2 - \left(\tfrac{n\pi}{c}\right)^2}, \\
k_{3x} &= \sqrt{k_3^2 - \left(\tfrac{m\pi}{b}\right)^2 - \left(\tfrac{n\pi}{c}\right)^2}, \\
Y_{1mn} &= \frac{\mu_1}{\mu_2 k_{1x}} \tan(k_{1x} d_1), \\
Y_{2mn} &= \frac{\mu_3}{\mu_2 k_{3x}} \tan(k_{3x}(d_2 - a)), \\
J_{mn} &= \cos(k_{2x}(d_2 - d_1))(k_{2x} Y_{2mn} - k_{2x} Y_{1mn}) - \sin(k_{2x}(d_2 - d_1))(1 + k_{2x}^2 Y_{1mn} Y_{2mn}), \\
M_{mn} &= Y_{1mn}[\sin(k_{2x}(x_s - d_2)) + k_{2x} Y_{2mn} \cos(k_{2x}(x_s - d_2))]/J_{mn}, \\
L_{mn} &= Y_{2mn}[\sin(k_{2x}(x_s - d_1)) + k_{2x} Y_{1mn} \cos(k_{2x}(x_s - d_1))]/J_{mn}, \\
K_{mn} &= k_{3x} k_2^2 \mu_3 \sin(k_{3x}(a - d_2)) \cdot \\
&[k_{2x} k_1^2 \mu_2 \cos(k_{1x} d_1) \cos(k_{2x}(d_2 - d_1)) - k_{1x} k_2^2 \mu_1 \sin(k_{1x} d_1) \sin(k_{2x}(d_2 - d_1))] \\
&+k_{2x} k_3^2 \mu_2 \cos(k_{3x}(a - d_2)) \cdot \\
&[k_{2x} k_1^2 \mu_2 \cos(k_{1x} d_1) \sin(k_{2x}(d_2 - d_1)) + k_{1x} k_2^2 \mu_1 \sin(k_{1x} d_1) \cos(k_{2x}(d_2 - d_1))] .
\end{aligned}
\tag{2.105}
$$

case 2b: electric source in the y-direction

Two components of the Green's dyad $\bar{\bar{G}}_{Ai}$ are still unknown, namely G_{Aiyy} and G_{Aixy}. It is possible to calculate these functions using the analysis of the previous section. However, the y-directed source is, just like the z-directed dipole, positioned along the dielectric interface. Therefore, it is more convenient to make use of the symmetry of the problem. The functions G_{Aiyy} and G_{Aixy} can be obtained from the functions G_{Aizz} and G_{Aixz} by using the substitutions

$$
c := b,\ b := -c,\ z_s := y_s,\ y_s := -z_s,\ z := y,\ y := -z,\ \vec{e}_z := \vec{e}_y \text{ and } \vec{e}_y := -\vec{e}_z \tag{2.106}
$$

In this way, the geometry has been rotated along the x-axis. One problem that remains unsolved is the correct expansion of the delta-distribution into a Fourier-series. In (2.37), the assumption is made that the room dimensions represented by b and c are positive. Therefore, it is necessary to change the factors $\frac{1}{bc}$ (occurring before the summations) into the factors $\frac{1}{|bc|}$.

All components of the Green's dyad $\bar{\bar{G}}_{Ai}$ are now known. In the next section, the electromagnetic fields will be calculated using the dyad $\bar{\bar{G}}_{Ai}$.

2.4 Electromagnetic fields

As stated earlier, the electromagnetic fields are obtained from the vector potential by using the following expression

$$\vec{E}_i(\vec{r}) = -j\omega \left[\vec{A}_i(\vec{r}) + \frac{1}{k_i^2} \nabla\nabla \cdot \vec{A}_i(\vec{r}) \right]. \tag{2.107}$$

where the vector potential may be written in terms of the dyadic Green's function $\bar{\bar{G}}_{Ai}(\vec{r}, \vec{r}_s)$.

$$\vec{A}_i(\vec{r}) = \int\int\int \bar{\bar{G}}_{Ai}(\vec{r}, \vec{r}_s) \cdot \vec{J}_e(\vec{r}_s) dV_s. \tag{2.108}$$

Substitution of (2.108) in (2.107) gives

$$\vec{E}_i(\vec{r}) = -j\omega \int\int\int_{V_s} \left[\bar{\bar{G}}_{Ai} + \frac{1}{k_i^2} \nabla\nabla \cdot \bar{\bar{G}}_{Ai} \right] \cdot \vec{J}_e dV_s. \tag{2.109}$$

The electric field generated by an unit point-source can also be written in terms of an electric dyadic function $\bar{\bar{G}}_{Ei}(\vec{r}, \vec{r}_s)$

$$\vec{E}_i(\vec{r}) = -j\omega \int\int\int \bar{\bar{G}}_{Ei}(\vec{r}, \vec{r}_s) \cdot \vec{J}_e(\vec{r}_s) dV_s. \tag{2.110}$$

The electric Green's dyad is represented by a 3 x 3 matrix of the following form

$$\bar{\bar{G}}_{Ei} = \begin{bmatrix} G_{Eixx} & G_{Eixy} & G_{Eixz} \\ G_{Eiyx} & G_{Eiyy} & G_{Eiyz} \\ G_{Eizx} & G_{Eizy} & G_{Eizz} \end{bmatrix}. \tag{2.111}$$

The previous analysis implies that the electric dyadic Green's function $\bar{\bar{G}}_{Ei}$ can be found from

$$\bar{\bar{G}}_{Ei}(\vec{r}, \vec{r}_s) = \bar{\bar{G}}_{Ai}(\vec{r}, \vec{r}_s) + \frac{1}{k_i^2} \nabla\nabla \cdot \bar{\bar{G}}_{Ai}(\vec{r}, \vec{r}_s). \tag{2.112}$$

The nine components of the electric Green's dyad can be calculated by using the results from the previous section. The functions G_{Eixx}, G_{Eiyy} and G_{Eizz} need some further consideration.

For example, the function G_{Eixx} is obtained by

$$G_{Eixx} = G_{Aixx} + \frac{1}{k_i^2}\frac{\partial^2}{\partial x^2} G_{Aixx}, \tag{2.113}$$

where

$$G_{Aixx} = \sum_{m=1}^{\infty}\sum_{n=1}^{\infty} \sin(k_{ym}y)\sin(k_{zm}z) F_{imn}(x). \tag{2.114}$$

From (2.47), it is clear that the derivative of the function $F_{imn}(x)$ has a jump of size $\frac{4\mu_2}{bc}\sin(k_{ym}y_s)\sin(k_{zn}z_s)$ at $x = x_s$. Therefore, the second derivative of $F_{imn}(x)$ must contain a delta distribution. In order to calculate G_{Eixx} correctly, $F_{2mn}(x)$ is written in the following form [Signalen 1]

$$F_{2mn}(x) = F^1_{2mn}(x)\left[1 - u(x - x_s)\right] + F^2_{2mn}(x)\left[1 - u(x_s - x)\right], \tag{2.115}$$

where

$$u(x) = \begin{cases} 1, & \text{for } x > 0 \\ 0, & \text{for } x < 0 \end{cases} \tag{2.116}$$

The first derivative of $F_{2mn}(x)$ with respect to x is

$$\frac{d}{dx}F_{2mn}(x) = \frac{dF^1_{2mn}}{dx}\left[1 - u(x - x_s)\right] + \frac{dF^2_{2mn}}{dx}\left[1 - u(x_s - x)\right]. \tag{2.117}$$

The second derivative of $F_{2mn}(x)$ is given by

$$\begin{aligned} \frac{d^2}{dx^2}F_{2mn}(x) &= \frac{d^2F^1_{2mn}}{dx^2}\left[1 - u(x - x_s)\right] + \frac{d^2F^2_{2mn}}{dx^2}\left[1 - u(x_s - x)\right] \\ &-\frac{4\mu_2}{bc}\sin(k_{ym}y_s)\sin(k_{zn}z_s)\delta(x - x_s). \end{aligned} \tag{2.118}$$

The function G_{Eixx} is now written as

$$\begin{aligned} G_{Eixx} &= G_{Aixx} + \frac{1}{k_i^2}\sum_{m=1}^{\infty}\sum_{n=1}^{\infty}\sin(k_{ym}y)\sin(k_{zn}z)\frac{d^2}{dx^2}F_{imn}(x) \\ &-\frac{\mu_2}{k_2^2}\delta(\vec{r} - \vec{r}_s). \end{aligned} \tag{2.119}$$

In a similar way, the functions G_{Eiyy} and G_{Eizz} contain also delta-function dependencies. It is not practical to present all nine components of the electric Green's dyad, because this would result in many pages of formulas. Therefore, two components of the dyad have been selected, namely G_{Eixx} and G_{Eixz}. The function G_{Eixx} is presented in the appendix. This function results from the relative simple expression of G_{Aixx}. The function G_{Eixz} is also presented in the appendix. G_{Eixz} has a more complicated form, because the function G_{Aixz} has to be used for the calculation of G_{Eixz}.

The magnetic fields can be expressed in terms of the vector potential by

$$\vec{H}_i(\vec{r}) = \frac{1}{\mu_i}\nabla \times \vec{A}_i(\vec{r}), \tag{2.120}$$

where the vector potential can be written as

$$\vec{A}_i(\vec{r}) = \int\int\int \bar{\bar{G}}_{Ai}(\vec{r},\vec{r}_s) \cdot \vec{J}_e(\vec{r}_s) dV_s. \tag{2.121}$$

Substitution of (2.121) in (2.120) results in

$$\vec{H}_i(\vec{r}) = \frac{1}{\mu_i}\int\int\int \nabla \times \bar{\bar{G}}_{Ai}(\vec{r},\vec{r}_s) \cdot \vec{J}_e dV_s. \tag{2.122}$$

The magnetic field generated by a point-source is written in terms of a magnetic dyadic function $\bar{\bar{G}}_{Hi}(\vec{r},\vec{r}_s)$

$$\vec{H}_i(\vec{r}) = \int\int\int \bar{\bar{G}}_{Hi}(\vec{r},\vec{r}_s) \cdot \vec{J}_e(\vec{r}_s) dV_s. \tag{2.123}$$

The magnetic Green's dyad is represented by a 3 x 3 matrix

$$\bar{\bar{G}}_{Hi} = \begin{bmatrix} G_{Hixx} & G_{Hixy} & G_{Hixz} \\ G_{Hiyx} & G_{Hiyy} & G_{Hiyz} \\ G_{Hizx} & G_{Hizy} & G_{Hizz} \end{bmatrix}. \tag{2.124}$$

So the magnetic Green's dyad $\bar{\bar{G}}_A$ can be found from

$$\bar{\bar{G}}_{Hi}(\vec{r},\vec{r}_s) = \frac{1}{\mu_i}\nabla \times \bar{\bar{G}}_{Ai}(\vec{r},\vec{r}_s). \tag{2.125}$$

Two components of the magnetic Green's dyad are presented in the appendix, namely G_{Hzx} and G_{Hyz}. These two functions are selected, because of the differences in complexity between the two functions. The function G_{Hyz} has a more complicated form than G_{Hzx}.

Numerical results of the electromagnetic fields due to a point-source are presented in chapter 3. The electromagnetic fields generated by a half-wave dipole are calculated analytically in section 2.6. These fields are obtained by evaluating the equations (2.110) and (2.123). Some results for this type of source are given in chapter 3.

2.5 Estimate of the truncation error

In the previous sections, it has been shown that the electromagnetic fields inside a perfectly conducting room are described by double series. We will use a computer to obtain numerical results for the electromagnetic fields of several rooms, various sources, etc. In computations, we work with a finite number of digits and use finitely many steps. Therefore, the numerical result is an approximate value of the (unknown) exact result.

Depending on the source of errors, we can distinguish between

- Experimental errors. (for example errors in input data)
- Round-off errors. (caused by the process of rounding off during computation)
- Programming errors (errors in software or mistakes from the programmer)
- Truncation errors (errors caused by prematurely breaking off a series of computational steps)

We will further investigate the consequences of truncation errors in this section. The infinite series, describing the electromagnetic fields in a room, are replaced by partial sums for implementation on a computer. First, the relatively simple case of a perfectly conducting room will be considered. For this configuration, an accurate estimate can be given for the accuracy of the computed electromagnetic fields. A numerical study will show that the actual error is in the same order as the predicted error. Second, an error estimate will be calculated for the electromagnetic fields in a room with two dielectric walls. In this case, the predicted truncation error differs much more to the actual error. The results obtained from the analysis of the truncation error will be used to improve the computer program. The program determines the minimal number of terms of the double series which will be needed for obtaining the desired level of accuracy (the accuracy is provided by the user of the program).

Error estimate for electromagnetic fields inside a perfectly conducting room

Only G_{Exx} (representing the x-component of the electric field generated by a point-source in the x-direction) will be considered in order to avoid an unnecessary large amount of formulas. An error estimate for the other components of the Green's dyad can be obtained in a similar way. The Green's function G_{Exx} is calculated by substituting the values $d_1 = 0$, $d_2 = a$, $\epsilon_1 = \epsilon_2 = \epsilon_3 = \epsilon_0$, $\mu_1 = \mu_2 = \mu_3 = \mu_0$ in equation (A.2). The Green's function has the following form

$$G_{Exx} = \frac{4\mu_0}{bck_0^2} \sum_{m=1}^{\infty} \sum_{n=1}^{\infty} (k_0^2 - k_x^2) \sin\frac{m\pi y}{b} \sin\frac{m\pi y_s}{b} \sin\frac{n\pi z}{c} \sin\frac{n\pi z_s}{c} \frac{\cos k_x(x_s - a)\cos(k_x x)}{k_x \sin(k_x a)}, \qquad \text{for } x \leq x_s, \tag{2.126}$$

with $k_x = \sqrt{k_0^2 - (\frac{m\pi}{b})^2 - (\frac{n\pi}{c})^2}$. The truncation error for G_{Exx} in the interval $x > x_s$ can be obtained in a similar way, therefore it will not be calculated here. Depending on the argument of $k_0^2 - (\frac{m\pi}{b})^2 - (\frac{n\pi}{c})^2$, we will distinguish between two situations [Leyten/Dolmans 95]

$$\underline{\text{Domain 1 } (D_1): \quad \left(\frac{m\pi}{b}\right)^2 + \left(\frac{n\pi}{c}\right)^2 - k_0^2 \leq 0} \tag{2.127}$$

$$G^a_{Exx} = \frac{4\mu_0}{bck_0^2} \sum_{m,n \in D_1} \sum (k_0^2 - \alpha_1^2) \sin\frac{m\pi y}{b} \sin\frac{m\pi y_s}{b} \sin\frac{n\pi z}{c} \sin\frac{n\pi z_s}{c} \times$$

$$\frac{\cos(\alpha_1 x)\ \cos\alpha_1(a - x_s)}{\alpha_1\ \sin(\alpha_1 a)},$$

where $\alpha_1 = \sqrt{k_0^2 - (\frac{m\pi}{b})^2 - (\frac{n\pi}{c})^2}$.

$$\text{Domain 2 } (D_2): \quad \left(\frac{m\pi}{b}\right)^2 + \left(\frac{n\pi}{c}\right)^2 - k_0^2 > 0 \tag{2.128}$$

$$G^b_{Exx} = \frac{-2\mu_0}{bck_0^2} \sum_{m,n\in D_2}\sum (k_0^2 + \alpha_2^2) \sin\frac{m\pi y}{b} \sin\frac{m\pi y_s}{b} \sin\frac{n\pi z}{c} \sin\frac{n\pi z_s}{c} \times$$

$$\frac{e^{\alpha_2(x-x_s)}\left[1 + e^{-2\alpha_2(a-x_s)}\right]\left[1 + e^{-2\alpha_2 x}\right]}{\alpha_2\left[1 - e^{-2\alpha_2 a}\right]},$$

where $\alpha_2 = \sqrt{\left(\frac{m\pi}{b}\right)^2 + \left(\frac{n\pi}{c}\right)^2 - k_0^2}$.

The closed domain D_1 and the open domain D_2 are presented in figure 2.3.

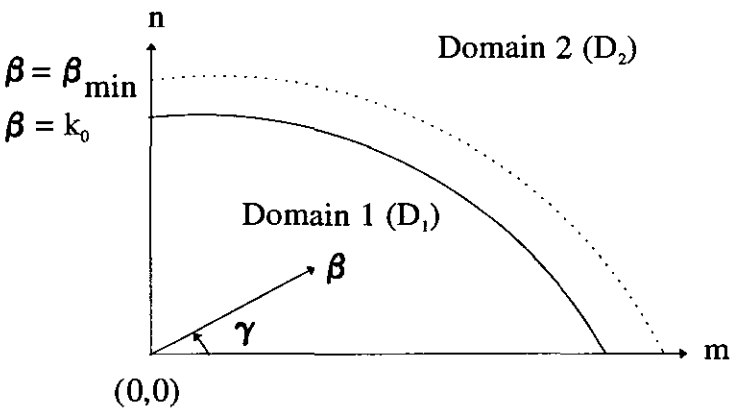

Figure 2.3: *Two dimensional grid ($\beta_{min} \geq k_0$).*

The assumption will be made that the computation is carried out in such a way that all the terms of the double series at the grid-points in D_1 are evaluated. So we will restrict our analysis to the Green's function in domain D_2. The following inequality is obtained for the Green's function in D_2

$$|G^b_{Exx}| \leq \frac{2\mu_0}{bck_0^2} \sum_{m,n\in D_2}\sum \left[\left(\frac{m\pi}{b}\right)^2 + \left(\frac{n\pi}{c}\right)^2\right] \frac{e^{\alpha_2(x-x_s)}\left[1 + e^{-2\alpha_2(a-x_s)}\right]\left[1 + e^{-2\alpha_2 x}\right]}{\alpha_2\left[1 - e^{-2\alpha_2 a}\right]}$$

The following functions are investigated more closely

$$g_1(\alpha_2) = \frac{[1 + e^{-2\alpha_2(a-x_s)}][1 + e^{-2\alpha_2 x}]}{1 - e^{-2\alpha_2 a}}, \tag{2.129}$$

$$g_2(\alpha_2) = \frac{[1 + e^{-2\alpha_2(a-x_s)}][1 - e^{-2\alpha_2 x}]}{1 - e^{-2\alpha_2 a}}, \tag{2.130}$$

$$g_3(\alpha_2) = \frac{[1 - e^{-2\alpha_2(a-x_s)}][1 - e^{-2\alpha_2 x}]}{1 - e^{-2\alpha_2 a}}. \tag{2.131}$$

An upper bound for the function $g_1(\alpha_2)$ for $\alpha_2 \geq \alpha_{2min}$ has to be found before an integral theorem can be used to calculate the error estimate. In this section, only the component G_{Exx} is presented. In case other field components will be calculated, functions comparable to $g_2(\alpha_2)$ and $g_3(\alpha_2)$ will appear in the Green's functions. Therefore, upper bounds for these two functions will also be given.

The following limits of $g_3(\alpha_2)$ are obtained

$$\lim_{\alpha_2 \downarrow 0} g_3(\alpha_2) = 0, \qquad \lim_{\alpha_2 \to \infty} g_3(\alpha_2) = 1. \tag{2.132}$$

The function $g_3(\alpha_2)$ will never exceed the value 1, therefore, the following inequality will be used: $g_3\ (\alpha_2)\ < 1$. Likewise, the function $g_2(\alpha_2) \leq 1 + e^{-2\alpha_{2min}(a-x_s)}$.

The upper bound for $g_1(\alpha_2)$ is found in a different way. First, the limit of $g_1(\alpha_2)$ is given by $\lim_{\alpha_2 \to \infty} g_1(\alpha_2) = 1$. Then, the derivative of $g_1(\alpha_2)$ with respect to α_2 is given by:

$$\frac{dg_1(\alpha_2)}{d\alpha_2} = -2\Big[(a - x_s)e^{-2\alpha_2(a-x_s)} + (a - x_s + x)e^{-2\alpha_2(a-x_s+x)} + x_s e^{-2\alpha_2(2a-x_s)} + \tag{2.133}$$

$$(x_s - x)e^{-2\alpha_2(2a-x_s+x)} + xe^{-2\alpha_2 x} + (a - x)e^{-2\alpha_2(x+a)} + ae^{-2\alpha_2 a}\Big]/(1 - e^{-2\alpha_2 a})^2 < 0. \tag{2.134}$$

Due to the fact that $g_1(\alpha_2)$ is a decreasing function, we can write $g_1(\alpha_2) \leq g_1(\alpha_{2min})$. Notice that in practice, the functions $g_i(x)$ (i=1,2,3) will be approximately equal to unity.

In order to get an integral representation, the following integral-theorem is used

If $f(x) > 0$ for $x \in [0, \infty)$, $f(x)$ real positive decreasing function , then
i. $S_N - f(1) \leq I_N \leq S_{N-1}$
ii. $\int_0^\infty f(t)dt$ converges $\Longleftrightarrow \sum_{n=1}^{\infty} f(n)$ converges
with $I_N = \int_1^N f(t)dt$ and $S_N = \sum_{n=1}^{N} f(n)$.

The variables m and n (summation-indices) are transformed to a new set of variables β and γ using the following equations

$$m = \frac{b}{\pi}\beta\cos\gamma, \qquad n = \frac{c}{\pi}\beta\sin\gamma. \tag{2.135}$$

After substitution of the variables γ and β in equation (2.128) the boundary between the two domains is given by $\beta = k_0$. When the numerical calculations are restricted to the domain $0 < \beta < \beta_{min}$, $0 \leq \gamma \leq \pi/2$, the absolute value of the truncation error is given by

$$\Big|\sum_{(\frac{m\pi}{b})^2+(\frac{n\pi}{c})^2>\beta_{min}^2}\sum G^b_{Exx}(m,n)\Big| \leq \frac{2\mu_0 g_1(\beta_{min})}{\pi^2 k_0^2}\int_{\beta_{min}}^{\infty}\int_0^{\frac{\pi}{2}} \frac{\beta^3\ e^{\sqrt{\beta^2-k_0^2}(x-x_s)}}{\sqrt{\beta^2 - k_0^2}}\, d\gamma\, d\beta. \tag{2.136}$$

Using the variable p, with $p^2 = \beta^2 - k_0^2$, we obtain

$$|\sum_{(\frac{m\pi}{b})^2+(\frac{n\pi}{c})^2>\beta_{min}^2} \sum G_{Exx}^b(m,n)| \leq \frac{\mu_0 g_1(\beta_{min})}{\pi k_0^2} \int_{\sqrt{\beta_{min}^2-k_0^2}}^{\infty} (p^2+k_0^2)\ e^{p(x-x_s)}\, dp. \tag{2.137}$$

Solving the integral results in

$$|\sum_{(\frac{m\pi}{b})^2+(\frac{n\pi}{c})^2>\beta_{min}^2} \sum G_{Exx}^b(m,n)| \leq \frac{\mu_0 g_1(\beta_{min})}{\pi k_0^2} \times \tag{2.138}$$

$$\left[\frac{-\beta_{min}^2 e^{\zeta}}{x-x_s} + \frac{2\sqrt{\beta_{min}^2-k_0^2}e^{\zeta}}{(x-x_s)^2} - \frac{2e^{\zeta}}{(x-x_s)^3} \right],$$

with $\zeta = \sqrt{\beta_{min}^2 - k_0^2}(x-x_s)$.
Two interesting observations can be made from (2.138):

- The number of terms needed to obtain a required accuracy increases for x approaches x_s.

- The error estimate (for $g_1(\beta_{min})$ approximately equal to unity) and the size of domain D_1 are independent of the variable a. This implies that for large values of the dimension a, the computational time does not increase for the presented Green's function. This means that propagation in corridors or tunnels can be calculated very efficiently with the presented Green's functions.

In the remainder of this report, the truncation error will be denoted by the symbol $\delta(\beta_{min})$. The 'exact' Green's function may be written as

$$G_{Exx}(\beta_{max}) = \tilde{G}_{Exx}(\beta_{min}) + \delta(\beta_{min}) \tag{2.139}$$

where $\tilde{G}_{Exx}$ is the computed Green's function and $\delta(\beta_{min})$ is the truncation error. The 'exact value' of the Green's function represented by $G_{Exx}(\beta_{max})$ will be calculated by summation of many terms. The error estimate predicts an exponential decay of the Green's functions with respect to β, therefore the partial sums can be used to represent the 'exact' value of the Green's function.
The predicted error will be compared to the actual error for the following configuration

- Dimensions of the room: $a = 5.13\text{m}, b = 4.04\text{m}, c = 3.02\text{m}$
- Location of the point-source: $(x_s, y_s, z_s) = (0.75\text{m}, 0.20\text{m}, 0.4\text{m})$
- Location of the observation point: $(x, y, z) = (2.0\text{m}, 0.50\text{m}, 2.3\text{m})$
- Frequency is 2.0 GHz which corresponds to the wavenumber $k_0 = 41.89\ \text{m}^{-1}$
- Partial sum representing 'exact value' calculated with $\beta_{max} = 80$

The predicted error is given by equation (2.138) and the actual absolute error is computed by

$$\delta_{actual,a}(\beta_{min}) = |G_{Exx}(\beta_{max}) - \tilde{G}_{Exx}(\beta_{min})| \tag{2.140}$$

The actual relative error is given by

$$\delta_{actual,r}(\beta_{min}) = \left| \frac{G_{Exx}(\beta_{max}) - \tilde{G}_{Exx}(\beta_{min})}{G_{Exx}(\beta_{max})} \right| \text{ x } 100\% \tag{2.141}$$

The two truncation errors (predicted and actual errors) as a function of the size of the grid β_{min} are compared to each other in figure 2.4.

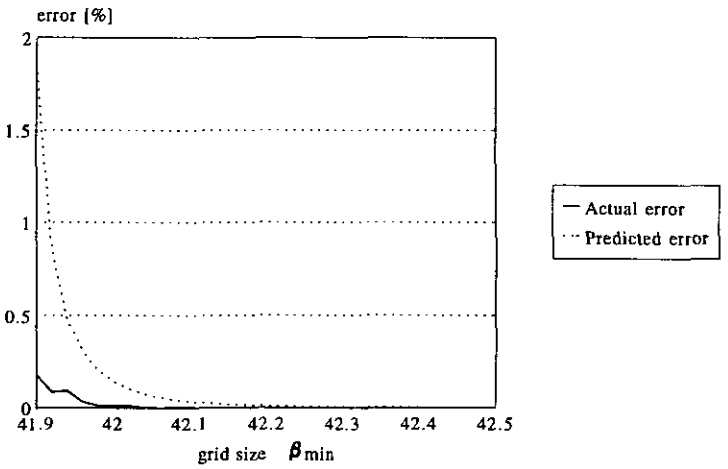

Figure 2.4: *Percentages of predicted and actual truncation errors*

As expected the actual error remains below the predicted error. Furthermore, figure 2.4 shows that the truncation error is less than 0.2 %. For this particular configuration, it is sufficient to restrict the computations to domain D_1. If the distance between the location of the transmitter and the location of the receiver becomes smaller (in particular the x-coordinates of the receiver and transmitter), the truncation error will increase. However, the truncation error will decrease rapidly as a function of the grid size (determined by β_{min}). We will now verify in a numerical way the assumption that the truncation error is not depending on the length of the room (denoted by the symbol a). For this purpose, the following configuration is used

- Dimensions of the room: $5\text{m} < a < 100\text{m}, b = 4.04\text{m}, c = 3.02\text{m}$
- Location of the point-source: $(x_s, y_s, z_s) = (0.75\text{m}, 0.20\text{m}, 0.4\text{m})$
- Location of the observation point: $(x, y, z) = (2.0\text{m}, 0.50\text{m}, 2.3\text{m})$
- Frequency is 2.0 GHz which corresponds to the wavenumber $k_0 = 41.89\ \text{m}^{-1}$
- Grid size $\beta_{min} = 42$

Figure 2.5 shows clearly that the accuracy of the computed electromagnetic fields is not depending on the length of the room. It can be concluded that the same computation time is needed for calculation of the fields in a small room or in a large tunnel.

The truncation error is calculated for a room with perfectly conducting walls. The next step is to obtain an error estimate for the electromagnetic fields inside a room with two dielectric walls.

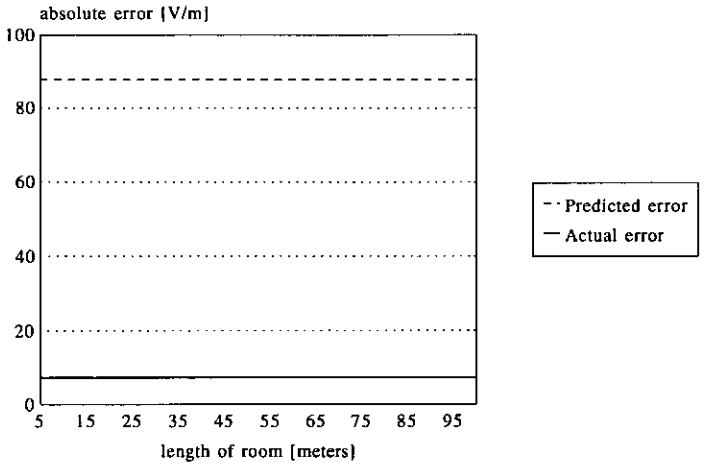

Figure 2.5: *Absolute values of predicted and actual truncation errors*

Error estimate for the electromagnetic fields inside a room with two dielectric walls

The assumption will be made that the dielectric losses of the walls are negligible. The consequences of this assumption will be evaluated at the end of this analysis. It is more difficult to obtain an error estimate due to fact that G_{Exx} consists of complicated expressions for a room with two dielectric walls (appendix A.1 - A.5). First we will use the same transformation as in the previous section:

$$m = \frac{b}{\pi}\beta\cos\gamma, \qquad n = \frac{c}{\pi}\beta\sin\gamma \tag{2.142}$$

The numerical calculation will be restricted to the domain $0 < \beta < \beta_{min}$, $0 \leq \gamma \leq \pi/2$. An error estimate will be derived for $\beta > \beta_{min}$. If $\beta >> max(k_1, k_2, k_3)$, we may write

$$\begin{aligned} k_{1x} &= -j\beta\sqrt{1 - \frac{k_1^2}{\beta^2}} \approx -j\beta \\ k_{2x} &= -j\beta\sqrt{1 - \frac{k_2^2}{\beta^2}} \approx -j\beta \\ k_{3x} &= -j\beta\sqrt{1 - \frac{k_3^2}{\beta^2}} \approx -j\beta \end{aligned} \tag{2.143}$$

The expressions Z_{1mn}, Z_{2mn} and D_{mn} (appendix A) are reduced to

$$Z_{1mn} = -\frac{\epsilon_2 k_{1x}}{\epsilon_1}\tan(k_{1x}d_1) \approx \frac{\epsilon_2\beta}{\epsilon_1} \tag{2.144}$$

$$Z_{2mn} = -\frac{\epsilon_2 k_{3x}}{\epsilon_3}\tan(k_{3x}(d_2 - a)) \approx \frac{\epsilon_2\beta}{\epsilon_3} \tag{2.145}$$

$$D_{mn} = \sin(k_{2x}(d_2 - d_1))(-k_{2x}^2 - Z_{1mn}Z_{2mn}) + \cos(k_{2x}(d_2 - d_1))(k_{2x}Z_{1mn} - k_{2x}Z_{2mn}) \approx \frac{e^{\beta(d_2-d_1)}}{2}\left[-j\beta^2 - j\frac{\epsilon_2^2\beta^2}{\epsilon_1\epsilon_3} - j\frac{\epsilon_2\beta^2}{\epsilon_1} - j\frac{\epsilon_2\beta^2}{\epsilon_3}\right] \tag{2.146}$$

Using the above approximations, we arrive at the following integrals

Interval 1: $0 \leq x \leq d_1$

$$\left|\sum_{(\frac{m\pi}{b})^2+(\frac{n\pi}{c})^2>\beta_{min}^2}\sum G_{Exx}^b(m,n)\right| \leq \frac{4\mu_1}{\pi^2 k_1^2}\int_{\beta_{min}}^{\infty}\int_0^{\frac{\pi}{2}} \beta^2\ e^{\beta(x_s-x)}\frac{-\frac{\epsilon_2}{\epsilon_3}-1}{-1-\frac{\epsilon_2^2}{\epsilon_1\epsilon_3}-\frac{\epsilon_2}{\epsilon_1}-\frac{\epsilon_2}{\epsilon_3}}\,d\gamma\,d\beta. \tag{2.147}$$

Solving the integrals results in

$$\left|\sum_{(\frac{m\pi}{b})^2+(\frac{n\pi}{c})^2>\beta_{min}^2}\sum G_{Exx}^b(m,n)\right| \leq \frac{2\mu_1}{\pi k_1^2}\frac{\epsilon_1}{\epsilon_1+\epsilon_2}\times \tag{2.148}$$

$$\left[\frac{-\beta_{min}^2 e^{\beta_{min}(x-x_s)}}{x-x_s} + \frac{2\beta_{min}e^{\beta_{min}(x-x_s)}}{(x-x_s)^2} - \frac{2e^{\beta_{min}(x-x_s)}}{(x-x_s)^3}\right].$$

The same procedure can be used for the error estimate in interval 2.

Interval 2: $d_1 < x \leq x_s$

$$\left|\sum_{(\frac{m\pi}{b})^2+(\frac{n\pi}{c})^2>\beta_{min}^2}\sum G_{Exx}^b(m,n)\right| \leq \frac{\mu_2}{\pi k_2^2}\times \tag{2.149}$$

$$\left[\frac{-\beta_{min}^2 e^{\beta_{min}(x-x_s)}}{x-x_s} + \frac{2\beta_{min}e^{\beta_{min}(x-x_s)}}{(x-x_s)^2} - \frac{2e^{\beta_{min}(x-x_s)}}{(x-x_s)^3}\right].$$

Interval 3: $x_s < x \leq d_2$

$$\left|\sum_{(\frac{m\pi}{b})^2+(\frac{n\pi}{c})^2>\beta_{min}^2}\sum G_{Exx}^b(m,n)\right| \leq \frac{\mu_2}{\pi k_2^2}\times \tag{2.150}$$

$$\left[\frac{-\beta_{min}^2 e^{\beta_{min}(x_s-x)}}{x_s-x} + \frac{2\beta_{min}e^{\beta_{min}(x_s-x)}}{(x_s-x)^2} - \frac{2e^{\beta_{min}(x_s-x)}}{(x_s-x)^3}\right].$$

Interval 4: $d_2 < x \leq a$

$$|\sum_{(\frac{m\pi}{b})^2+(\frac{n\pi}{c})^2>\beta_{min}^2} \sum G_{Exx}^b(m,n)| \leq \frac{2\mu_3}{\pi k_3^2} \frac{\epsilon_3}{\epsilon_2+\epsilon_3} \times \tag{2.151}$$

$$\left[\frac{-\beta_{min}^2 e^{\beta_{min}(x_s-x)}}{x_s-x} + \frac{2\beta_{min} e^{\beta_{min}(x_s-x)}}{(x_s-x)^2} - \frac{2e^{\beta_{min}(x_s-x)}}{(x_s-x)^3} \right].$$

Notice that the predicted error decreases for increasing values of the wavenumber k_i. Furthermore, there are now additional factors $\frac{\epsilon_1}{\epsilon_1+\epsilon_2}$ and $\frac{\epsilon_3}{\epsilon_2+\epsilon_3}$ present in the predicted errors for interval 1 and 4.

The predicted errors are valid for $\beta_{min} >> max(k_1, k_2, k_3)$. Such a large value of β_{min} becomes necessary for x approaches x_s. In this situation, β_{min} must be chosen very large to obtain the desired accuracy. To illustrate this, we will investigate the following configuration:

- Dimensions of the room: $a = 5.13\text{m}, b = 4.04\text{m}, c = 3.02\text{m}$
- Location of the point-source: $(x_s, y_s, z_s) = (0.75\text{m}, 0.20\text{m}, 0.4\text{m})$
- Location of the observation point: $(x, y, z) = (0.78\text{m}, 0.50\text{m}, 2.3\text{m})$
- Frequency is 2.0 GHz which corresponds to the wavenumber $k_0 = 41.89\ \text{m}^{-1}$
- Thicknesses of the two dielectric walls: $d_1 = a - d_2 = 40\text{cm}$
- Permittivity of each wall: $\epsilon_1 = \epsilon_3 = 3\epsilon_0$
- Grid size: $150 < \beta_{min} < 250$
- Partial sum representing 'exact value' calculated with $\beta_{max} = 350$

The predicted and actual truncation errors versus the size of the grid β_{min} are presented in the figures 2.6 and 2.7. Notice that the absolute errors are very large, this is due to the fact that an unrealistic source current strength of 1 A/m^2 generates very high electric fields inside the room. In practice, the source current at the feed point of the antenna will be lower, which causes smaller absolute errors. The source current strength does not influence the relative errors. The differences between the predicted and actual errors are larger for the configuration with the two dielectric walls than for the configuration with perfectly conducting walls. This is due to the fact that in the error estimate for the fields inside the room with two dielectric walls more approximations have been made. In the majority of the field computations for a room with perfectly conducting walls, the actual error is 10% of the predicted error. In most cases, the actual error is 1% of the predicted error for field computations in a room with two dielectric walls. For this configuration it can be concluded that the predicted error has a more 'conservative' nature.

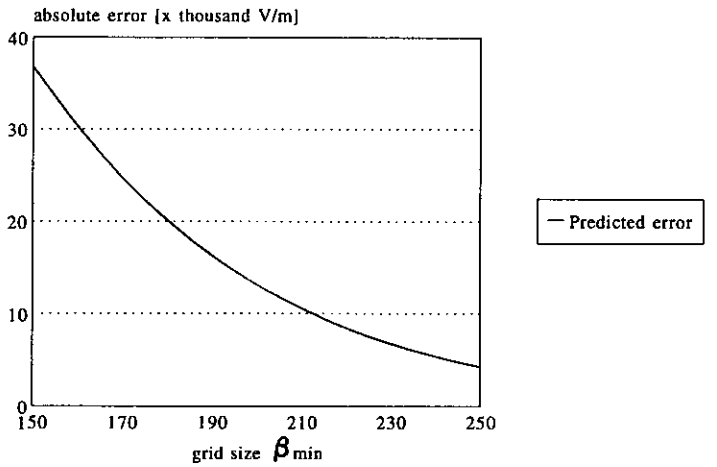

Figure 2.6: *Absolute value of predicted truncation error*

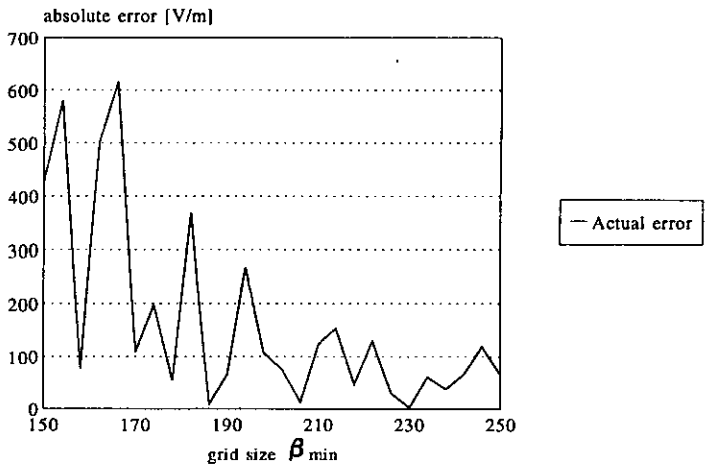

Figure 2.7: *Absolute value of actual truncation error*

We will now compute the truncation error of the electromagnetic fields inside a room with lossy, dielectric walls. In this case no predicted errors are available. Therefore, we will only show the actual error which is defined by

$$\delta_{actual} = G_{Exx}(\beta_{max} = 250) - \tilde{G}_{Exx}(\beta_{min} = 150) \tag{2.152}$$

- Dimensions of the room: $a = 5.13\text{m}, b = 4.04\text{m}, c = 3.02\text{m}$
- Location of the point-source: $(x_s, y_s, z_s) = (0.75\text{m}, 0.20\text{m}, 0.4\text{m})$
- Location of the observation point:
  situation A: $(x, y, z) = (0.78\text{m}, 0.50\text{m}, 2.3\text{m})$
  situation B: $(x, y, z) = (0.35\text{m}, 0.5\text{m}, 2.3\text{m})$
- Frequency is 2.0 GHz which corresponds to the wavenumber $k_0 = 41.89\ \text{m}^{-1}$

- Thickness of each dielectric wall: $d_1 = a - d_2 = 40\text{cm}$
- Permittivity of each wall: $\epsilon_1^{'} = \epsilon_3^{'} = 3\epsilon_0$
- Losses of the wall: $0 < \epsilon_1^{''} < 1$ and $0 < \epsilon_3^{''} < 1$
- Grid size: β_{min} =150
- Reference grid size: β_{max} = 250

The actual error versus the dielectric loss is presented in figure 2.8. The receiver is located in volume V_2.

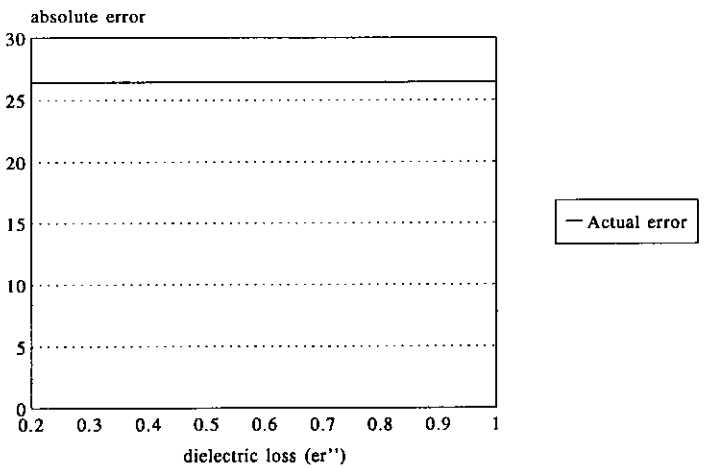

Figure 2.8: *Absolute value of actual truncation error (situation A)*

Figure 2.8 shows clearly that the dielectric loss has no influence on the accuracy of the computed fields. The error as a function of the dielectric loss for a receiver located inside the dielectric wall is shown in figure 2.9.

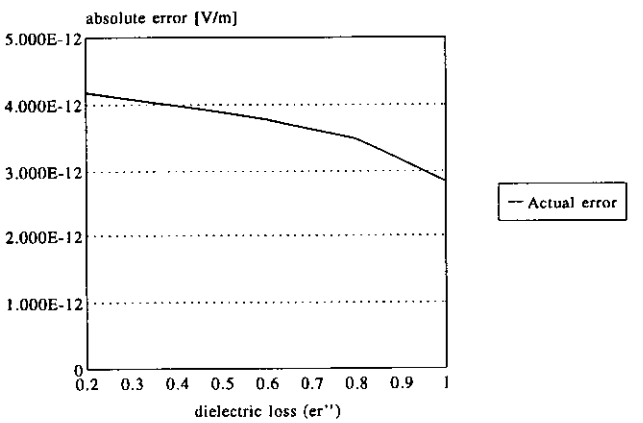

Figure 2.9: *Absolute value of actual truncation error (situation B)*

In this case, the truncation error decreases for increasing values of the dielectric losses. Therefore, it can be concluded that the inability of the error-estimate technique to model the dielectric losses has no significant impact on the accuracy of the computed fields.

The major advantage of using an error-estimation technique is that the calculations can now be done automatically. The user of the program defines a maximum absolute error which he wants to tolerate in the computed electromagnetic fields. The software program determines the size of the grid that corresponds to the given truncation error, after which the computations can start. The size of the grid is updated automatically for each observation-point in order to stay below the maximum truncation error.

The following conclusions can be drawn from the error-estimate analysis:

1) Due to the fact that the truncation error depends on the radius β_{min} only, it is more convenient to use an elliptical grid instead of a rectangular grid. In this way, the smallest amount of computations has to be carried out for obtaining the desired accuracy.

2) The truncation error increases for x approaches x_s, if the grid-size is kept at a constant level. This error is of the order $(x - x_s)^3$.

3) For large values of the length of the room, denoted by the symbol a, the computational time does not increase for the presented Green's function. This means that propagation in corridors or tunnels can be calculated very efficiently with the presented Green's function.

2.6 Fields of a half-wave dipole antenna

Up to now, the electromagnetic fields inside a room generated by an electric point-source have been analysed. In practice, cellular radio systems consist of sophisticated equipment (for example base stations, mobile telephone transceivers and paging systems). The antennas mounted on these devices differ much compared to the electric point-source (which is only a theoretical modelling tool). One of the most widely used antennas for wireless handsets is the quarter wavelength monopole antenna. Several other antennas are used, such as planar inverted F antennas, patch antennas and half-wave dipoles. The electromagnetic fields inside a room caused by a half-wave dipole and combinations of half-wave dipoles will be subject of study in this section.

Remember that the electric field in a room can be obtained for prescribed currents on the source (equation (2.110)). The assumption will be made that the current on the dipole resembles a cosine distribution. Normally, this current distribution is used for a dipole with an infinitely thin radius and operating in a free-space environment. In [Leersum 95], it is shown that this assumption is valid for dipoles very close to a perfectly conducting wall. For arbitrary current distributions, the calculation of the integrals in (2.110) must be done numerically. In case of a half-wave dipole, this integration is performed analytically, which reduces the computation time significantly. If the coupling between various transmitting antennas is negligible, superposition can be used for calculating the fields of several transmitters (e.g. arrays and diversity systems).

The electric field is given by

$$\vec{E}_i(\vec{r}) = -j\omega \int\int\int \bar{\bar{G}}_{Ei}(\vec{r},\vec{r}_s) \cdot \vec{J}_e(\vec{r}_s) dV_s. \tag{2.153}$$

The current distribution (using the above mentioned assumptions) of a half-wave dipole is given by

$$\vec{J}_e = I_0 \cos(k_2(x - x_s))\delta(y - y_s)\delta(z - z_s)\vec{e}_x, \qquad -\frac{\lambda}{4} \leq x - x_s \leq \frac{\lambda}{4}, \tag{2.154}$$

for an x-directed dipole located in region 2 (this region is depicted in figures 2.1 and 2.2). The strength of the current at the feed-point of the transmitting antenna is denoted by the symbol I_0. Only the field E_{ix} (parallel to the source) will be considered for the sake of brevity. The other electric field components can be obtained in a similar manner. Substitution of (2.154) in (2.153) gives

$$E_{ix} = -j\omega I_0 \int_{x_s-\frac{\lambda}{4}}^{x_s+\frac{\lambda}{4}} G_{Eixx} \cos(k_2(x_s - x'))dx'. \tag{2.155}$$

To illustrate the procedure for deriving E_{ix}, we will calculate E_{ix} in the interval $0 \leq x \leq d_1$ (interval 1). The electric field in the intervals 2 - 4 can be obtained in a similar way. The component G_{E1xx} of the Green's dyad is presented in the appendix by equation (A.1). Substitution of (A.1) in (2.155) results in

$$E_{1x} = \frac{4j\omega I_0\mu_1}{bck_1^2} \int_{x_s-\frac{\lambda}{4}}^{x_s+\frac{\lambda}{4}} \sum_{m=1}^{\infty}\sum_{n=1}^{\infty}(k_1^2 - k_{1x}^2)\sin(k_{ym}y)\sin(k_{ym}y_s)\sin(k_{zn}z)\sin(k_{zn}z_s)\cdot \frac{\cos(k_{1x}x)\left[Z_{2mn}\sin(k_{2x}(x' - d_2)) + k_{2x}\cos(k_{2x}(x' - d_2))\right]\cos(k_2(x' - x_s))}{D_{mn}\cos(k_{1x}d_1)}dx'. \tag{2.156}$$

Assuming that term by term integration is permissible, we may write

$$E_{1x} = \frac{4j\omega I_0\mu_1}{bck_1^2} \sum_{m=1}^{\infty}\sum_{n=1}^{\infty}\alpha(m,n)\left[\int_{x_s-\frac{\lambda}{4}}^{x_s+\frac{\lambda}{4}} Z_{2mn}\sin(k_{2x}(x' - d_2))\cos(k_2(x' - x_s))dx' + \int_{x_s-\frac{\lambda}{4}}^{x_s+\frac{\lambda}{4}} k_{2x}\cos(k_{2x}(x' - d_2))\cos(k_2(x' - x_s))dx'\right], \tag{2.157}$$

with $\alpha(m,n) = (k_1^2 - k_{1x}^2)\sin(k_{ym}y)\sin(k_{ym}y_s)\sin(k_{zn}z)\sin(k_{zn}z_s)\cos(k_{1x}x)/(D_{mn}\cos(k_{1x}d_1))$.

Solving the first integral in the right-hand side of equation (2.157) and using some algebraic manipulations results in

$$Z_{2mn}\int_{x_s-\frac{\lambda}{4}}^{x_s+\frac{\lambda}{4}} \sin(k_{2x}(x' - d_2))\cos(k_2(x' - x_s))dx' = \frac{-2Z_{2mn}k_2\sin(k_{2x}(x_s - d_2))\cos(k_{2x}\frac{\lambda}{4})}{k_{2x}^2 - k_2^2}. \tag{2.158}$$

The same procedure can be used for the calculation of the second integral in (2.157). In this way, the following formula for the electric field in the x-direction due to a half-wave dipole transmitter in the same direction is obtained

$$E_{1x} = -\frac{8j\omega I_0 k_2\mu_1}{bck_1^2} \sum_{m=1}^{\infty}\sum_{n=1}^{\infty}\left[k_1^2 - k_{1x}^2\right]\sin(k_{ym}y)\sin(k_{ym}y_s)\sin(k_{zn}z)\sin(k_{zn}z_s)\cdot \frac{\cos(k_{1x}x)\cos(k_{2x}\frac{\lambda}{4})\left[Z_{2mn}\sin(k_{2x}(x_s - d_2)) + k_{2x}\cos(k_{2x}(x_s - d_2))\right]}{D_{mn}\cos(k_{1x}d_1)(k_{2x}^2 - k_2^2)} \tag{2.159}$$

The current on the half-wave dipole antenna has a more 'distributed nature' compared to a point-source current. Therefore, it could be expected that the numerical convergence of the double series has been improved. Attention will be paid in the remainder of this section to the differences of the numerical convergence between the point-source and the half-wave dipole antenna computations. The above assumption will be verified for a receiver positioned nearby (singularity at the source) and far away from the source. The numerical truncation error will be calculated as a function of the size of the grid β_{min} (see section 2.5 for details). This error will be presented as a percentage of the 'exact' field value.

The following room configuration has been used

- Dimensions of the perfectly conducting room: $a = 5.13$m, $b = 4.04$m, $c = 3.02$m
- Locations of the point-source and feed-point of the $\frac{\lambda}{2}$ dipole: $(x_s, y_s, z_s) = (0.75\text{m}, 0.2\text{m}, 0.4\text{m})$
- Locations of the observations points:

  Near the source $(x, y, z) = (0.77\text{m}, 0.22\text{m}, 0.42\text{m})$ (position A)

  Further away from the source $(x, y, z) = (2\text{m}, 1\text{m}, 2.3\text{m})$ (position B)
- Frequency is 2.0 GHz, which corresponds to the wavenumber $k_0 = 41.89\ \text{m}^{-1}$
- 'Exact' fields are calculated with $\beta_{max} = 250$

The truncation error (half-wave dipole transmitter) at position B is presented in figure 2.10.

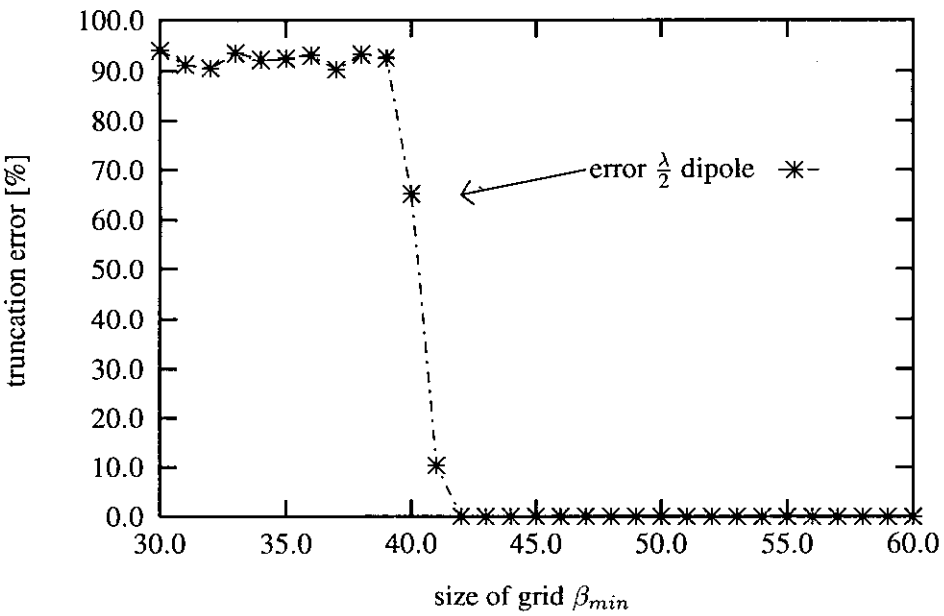

Figure 2.10: *Truncation error for $\frac{\lambda}{2}$ dipole at position B*

Figure 2.10 shows clearly that the error becomes negligible in case β_{min} exceeds the wave number k_0. This can be explained by the fact that the terms of the series decay exponentially in this region. The truncation error using a point-source (same dimensions of the room) is shown in figure 2.11. Again, the error becomes negligible for $\beta > k_0$. At $\beta = 42$, the truncation errors for a half-wave dipole and a point source are 0.051% and 0.056%, respectively. It can be concluded that the numerical

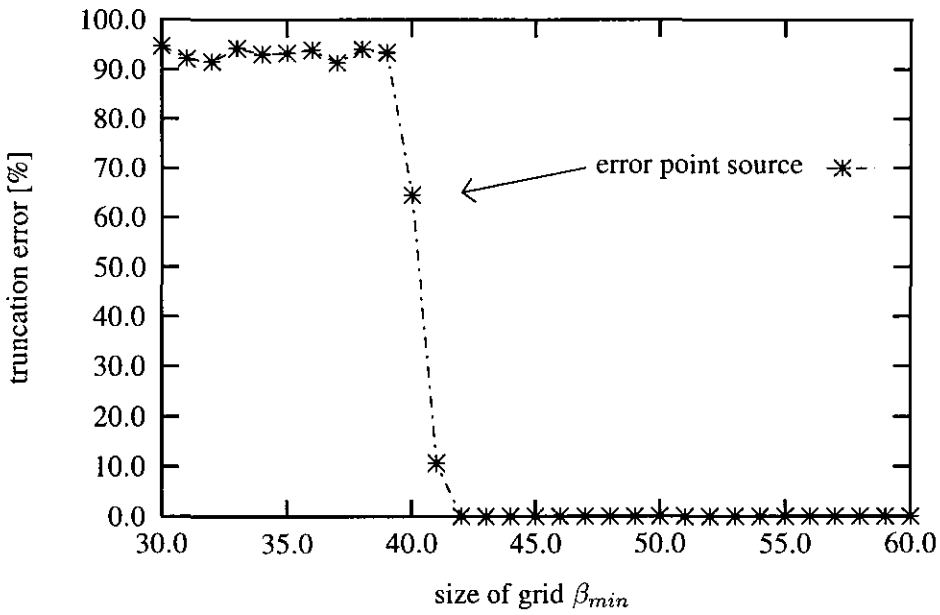

Figure 2.11: *Truncation error for point source at position B*

errors for the truncation of the series of the two types of sources are comparable.

We will now investigate the numerical convergence for a receiver positioned near the transmitter (position A). The truncation error will be increased due to the singular behaviour of the transmitted electromagnetic fields. The truncation errors are shown in figure 2.12 and 2.13.

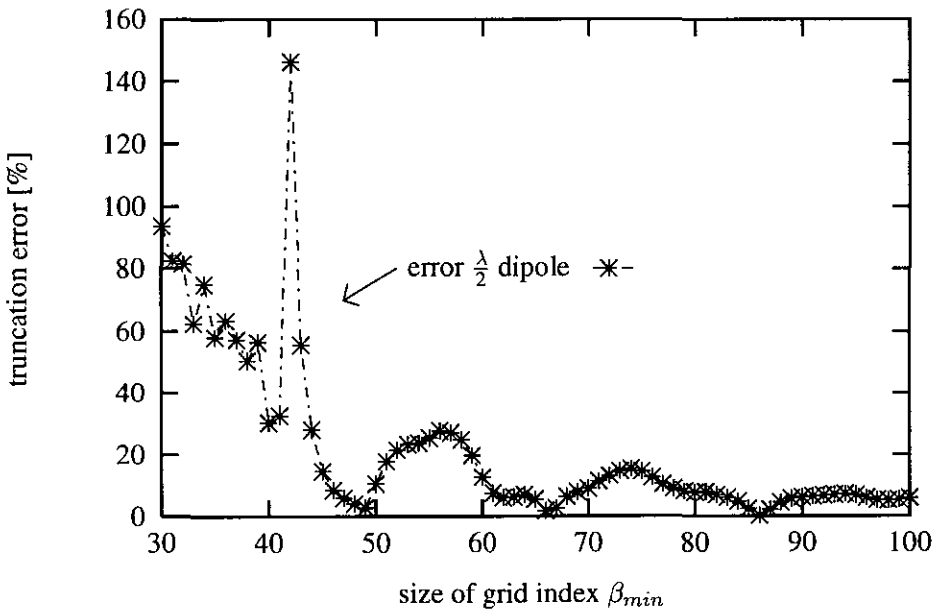

Figure 2.12: *Truncation error $\frac{\lambda}{2}$ dipole at position A*

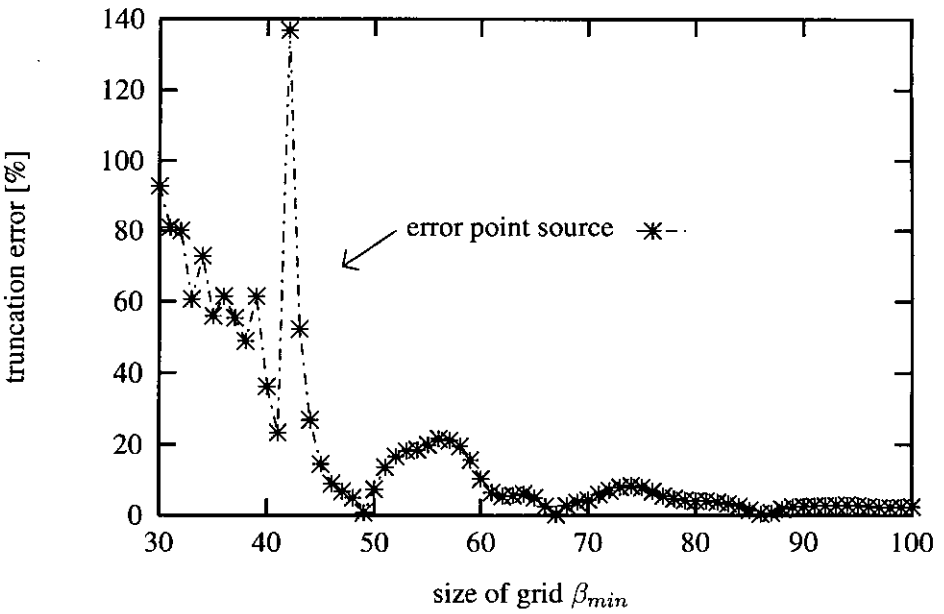

Figure 2.13: *Truncation error point source at position A*

Although the numerical errors are increased, the errors for the two types of sources are comparable to each other.

For multiple sources, the electric field can be found by using the superposition principle. In order to use this principle, it will be assumed that there is no coupling between the sources. For example, the electric field due to two sources is given by

$$\vec{E}_i(\vec{r}) = -j\omega \int\int\int \bar{\bar{G}}_{Ei}(\vec{r},\vec{r}_{s1})dV_{s1} - j\omega \int\int\int \bar{\bar{G}}_{Ei}(\vec{r},\vec{r}_{s2})dV_{s2}, \tag{2.160}$$

for two sources located at the coordinates $(x_s, y_s, z_s) = (x_{s1}, y_{s1}, z_{s1})$ and (x_{s2}, y_{s2}, z_{s2}).

The following conclusions can be drawn

- In this section the electromagnetic fields due to a half-wave dipole antenna have been presented. These fields are obtained by solving the integrals analytically. In this way, a computationally efficient software program has been developed.
- The convergence properties of the double series describing the fields for the two types of sources have been compared to each other. It has been found that the differences in numerical convergence are negligible.

Several results of the electromagnetic fields due to a half-wave dipole or combinations of half-wave dipoles are presented in chapter 3.

2.7 Port voltage, signal-to-noise ratio and bit error rate

In the previous sections, the electromagnetic fields due to a point-source or a half-wave dipole have been discussed. It is important to study the fields inside an indoor environment in order to understand the problems that can arise in such an environment. It will be shown in chapter 3 that the fields in a room are very irregular compared to the more uniform fields in free-space. However, it is not sufficient to calculate electromagnetic fields only. To design an optimal receiver, it is necessary to model the interaction between the electromagnetic fields and the type of receiving antenna. For this purpose, a Thévenin representation of the receiving antenna system will be derived using Lorentz reciprocity theorem. Depending on the type of the antenna system, some antennas will operate better in an indoor communication link than other types of antennas. In this section, the induced port voltage of a receiving antenna will be calculated by using the results of the previous sections. The antenna terminals will be modeled as an accessible port for which a voltage and a current is defined in the network sense. The received voltage will be calculated analytically for a half-wave dipole receiver by integration of the electromagnetic fields weighted by the current on the receiver. The voltage at the terminals of the antenna will become the most important parameter for designing an optimal receiving antenna unit. In chapter 3, the voltages of several diversity systems (selection diversity, optimal gain combining and linear combining) will be obtained and compared to each other.

The presence of noise degrades the performance of the indoor communication link. If the noise power at the receiver input is in the same order of magnitude as the signal power, inferior performance will occur. A measure for the signal quality is given by the signal-to-noise ratio. This ratio can be calculated from the signal and the noise power levels. The signal power is obtained by calculating the voltage and the current at the receiver terminals (obtained from the indoor electromagnetic fields). The noise will be presented by a zero mean stationary Gaussian bandlimited process. The noise power is obtained by multiplying the constant of Boltzman, the noise temperature and the noise bandwidth. The bandwidth of the noise will be assumed to be the same as the bandwidth of the signal.

The amount of noise has an impact on the maximum errorless rate of data transmission over a channel. The bit error rate depends on the signal-to-noise ratio of the telecommunication link. The relationship between the signal-to-noise ratio and the bit error rate is determined by the modulation scheme. In section 2.7.3, the probability of error for a DECT receiver will be described in terms of the signal and noise power at the receiver input.

In the sections 2.7.1, 2.7.2 and 2.7.3, the voltage, the signal-to-noise ratio and the bit-error rate will be theoretically analysed for a half-wave dipole receiver. In chapter 3, the performances of several diversity systems will be compared to each other by using the results of this section.

2.7.1 Thévenin representation of a receiving antenna

Most of the work presented here has been published in [Leyten/Dolmans 95]. The analysis presented in [Leyten/Dolmans 95] was very briefly. In this subsection some of the missing details have been added. Furthermore, the voltage of a half-wave dipole operating in a room with two dielectric walls will be calculated analytically. This will improve the computation time significantly.

To obtain a Thévenin representation of the receiving antenna, we need a reciprocity relation between the transmitting and receiving properties of an antenna. This relation can be obtained by using Lorentz's reciprocity theorem for electromagnetic fields. The following figure shows the configuration under consideration.

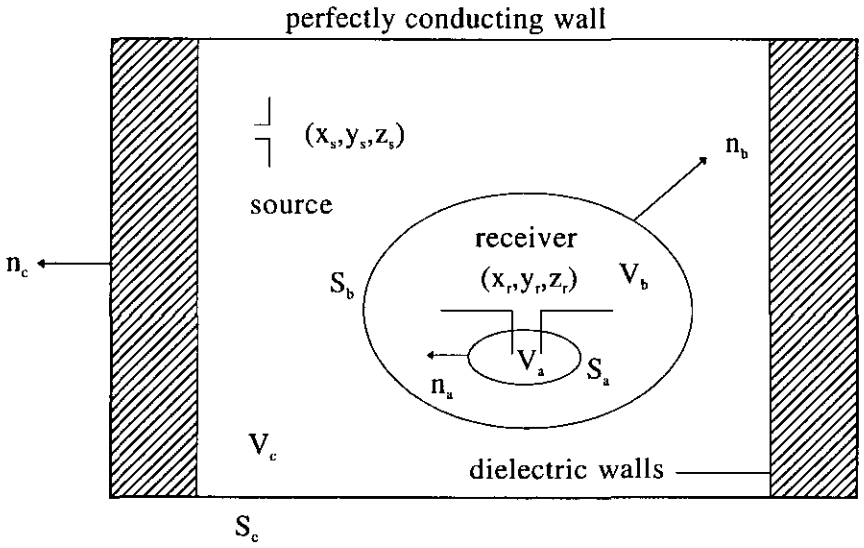

Figure 2.14: *Receiving antenna in an indoor environment*

The perfectly conducting walls of the room are depicted by S_c. The source is present in volume V_c which is enclosed by the surfaces S_b and S_c. The receiving antenna consists of two parts: the susceptible part and the terminal domain. In this way, the parts of the receiving system that are susceptible to electromagnetic radiation are separated from the parts that are not susceptible to electromagnetic radiation. The susceptible part of the receiving antenna is present in the volume V_b bounded by the closed surfaces S_a and S_b. The surface S_a is considered as the termination of the antenna system. Normal to S_a and S_b the unit vectors $\vec{n}_a$ and $\vec{n}_b$ are defined.

The antenna operates in two different states: the receiving state and the transmitting state. In the transmitting state, the accessible port of the antenna is fed by a source. This source is contained inside the volume V_a. The electromagnetic fields due to this source will be denoted by the symbols $(\vec{E}^T, \vec{H}^T)$. The voltage across the port and the current fed into the port are given by v^T and i^T, respectively. In the receiving state, the electromagnetic fields generated by the transmitting antenna (denoted by 'source' in figure 2.14) are incident upon the receiving antenna. These electromagnetic fields are represented by $(\vec{E}^R, \vec{H}^R)$. The induced voltage and current at the accessible port are given by v^R and i^R, respectively.

We will consider the vector function $\vec{E}^T \times \vec{H}^R - \vec{E}^R \times \vec{H}^T$ for the volume V_b. Taking the divergence of the vector function $\vec{E}^T \times \vec{H}^R$ and using Maxwell's equations results in

$$\nabla \cdot \left(\vec{E}^T \times \vec{H}^R\right) = -j\omega\mu_2 \vec{H}^T \cdot \vec{H}^R - j\omega\epsilon_2 \vec{E}^T \cdot \vec{E}^R, \tag{2.161}$$

where μ_2 and ϵ_2 are the permeability and permittivity of the materials in V_b. We have used the assumption that the volume V_b contains no sources. Interchanging the states 'R' and 'T', we can derive the divergence of a second vector function $\vec{E}^R \times \vec{H}^T$. Combination of these two vector functions and using the theorem of Gauss gives

$$\int\int_{S_a} \left(\vec{E}^R \times \vec{H}^T - \vec{E}^T \times \vec{H}^R\right) \cdot \vec{n}_a dS = \int\int_{S_b} \left(\vec{E}^R \times \vec{H}^T - \vec{E}^T \times \vec{H}^R\right) \cdot \vec{n}_b dS. \tag{2.162}$$

The next step is to introduce the voltages v^R, v^T and the currents i^R, i^T in the left-hand side of (2.162). The terminal domain V_a is assumed to be very small compared to the wavelength. Therefore the static form of the Maxwell's equations will be used. The electric field on the surface S_a is defined by a scalar potential $\Phi^{R,T}$

$$\vec{E}^{R,T} = -\nabla\Phi^{R,T}. \tag{2.163}$$

This expression is substituted in the left-hand side of (2.162).

$$\begin{aligned}&\int\int_{S_a}(\Phi^R\nabla\times\vec{H}^T-\Phi^T\nabla\times\vec{H}^R)\cdot\vec{n}_a dS+\int\int_{S_a}(\nabla\times(\Phi^T\vec{H}^R)-\nabla\times(\Phi^R\vec{H}^T))\cdot\vec{n}_a dS=\\&\int\int_{S_b}(\vec{E}^R\times\vec{H}^T-\vec{E}^T\times\vec{H}^R)\cdot\vec{n}_b dS.\end{aligned} \tag{2.164}$$

The relationship $(\nabla b)\times\vec{A}=\nabla\times(b\vec{A})-b\nabla\times\vec{A}$ has been used. The second integral in the left-hand side of (2.164) can be solved by using Green's theorem. The closed surface S_a is divided in two surfaces $S_{a'}$ and $S_{a''}$. Green's theorem can be written as

$$\int\int_S(\nabla\times\vec{A})\cdot\vec{n}dS=\int_C\vec{A}\cdot d\vec{l}, \tag{2.165}$$

where the integration is taken along the entire boundary C of S such that S is on the left as one advances in the direction of integration. Because the closed surface S_a is divided in two surfaces with opposite directions of integration, the second integral in the left-hand side of (2.164) vanishes. The following expression is obtained

$$\int\int_{S_a}(\Phi^R\nabla\times\vec{H}^T-\Phi^T\nabla\times\vec{H}^R)\cdot\vec{n}_a dS=\int\int_{S_b}(\vec{E}^R\times\vec{H}^T-\vec{E}^T\times\vec{H}^R)\cdot\vec{n}_b dS. \tag{2.166}$$

The electric and magnetic fields are predominantly concentrated around the conductors which are connected to the susceptible part. Hence, the integration over S_a is reduced to an integration over the terminals of the antenna. Then, the port voltage across the terminals of the antenna is equal to the scalar potential Φ at the terminal surface. The port current is equal to the integration of the curl of the magnetic field $\vec{H}$ along the terminal surface. Equation (2.166) is now written as

$$v^R i^T - v^T i^R = \int\int_{S_b}(\vec{E}^R\times\vec{H}^T-\vec{E}^T\times\vec{H}^R)\cdot\vec{n}_b dS. \tag{2.167}$$

The right-hand side of this equation is reduced to a more useful expression by decomposing the field in the receiving state into the incident field $(\vec{E}^I,\vec{H}^I)$ and scattered field $(\vec{E}^S,\vec{H}^S)$.

$$\begin{aligned}\vec{E}^R&=\vec{E}^I+\vec{E}^S,\\\vec{H}^R&=\vec{H}^I+\vec{H}^S.\end{aligned} \tag{2.168}$$

The incident field is defined as the field of the source inside V_c when the receiving antenna is not present. This incident field can be written as

$$\vec{E}^I(\vec{r})=-j\omega\int\int\int\bar{\bar{G}}_{Ei}(\vec{r},\vec{r_s})\cdot\vec{J}_e(\vec{r_s})dV_s. \tag{2.169}$$

Several components of the Green's dyad $\bar{\bar{G}}_{Ei}$ have been presented in the appendix. These components have been written in terms of a double series. The electric fields due to a point source or a half-wave dipole antenna have been discussed in the previous sections. These fields are incident upon the receiving antenna.

The scattered field can be associated with the currents induced by the incident fields on the susceptible part of the antenna. Substitution of (2.168) in (2.167) results in

$$\begin{aligned} v^R i^T - v^T i^R &= \int\int_{S_b} (\vec{E}^I \times \vec{H}^T - \vec{E}^T \times \vec{H}^I) \cdot \vec{n}_b dS \\ &+ \int\int_{S_b} (\vec{E}^S \times \vec{H}^T - \vec{E}^T \times \vec{H}^S) \cdot \vec{n}_b dS. \end{aligned} \tag{2.170}$$

Now, Lorentz reciprocity theorem will be applied to volume V_c. The sources of the scattered fields are located outside this volume, therefore we can write

$$\int\int_{S_b} (\vec{E}^S \times \vec{H}^T - \vec{E}^T \times \vec{H}^S) \cdot \vec{n}_b dS = \int\int_{S_c} (\vec{E}^S \times \vec{H}^T - \vec{E}^T \times \vec{H}^S) \cdot \vec{n}_c dS. \tag{2.171}$$

The right-hand side can be rewritten in a more useful form

$$\int\int_{S_c} (\vec{E}^S \times \vec{H}^T - \vec{E}^T \times \vec{H}^S) \cdot \vec{n}_c dS = \int\int_{S_c} (\vec{H}^T \cdot (\vec{n}_c \times \vec{E}^S) - \vec{H}^S \cdot (\vec{n}_c \times \vec{E}^T)) dS. \tag{2.172}$$

The tangential components of the electric field $\vec{E}^T$ (field generated by a source connected to the terminals of the receiving antenna) must vanish at the perfectly conducting walls at S_c. The tangential components of the electric field in the receiving state can be written as

$$\vec{n}_c \times \vec{E}^R = \vec{n}_c \times \vec{E}^I + \vec{n}_c \times \vec{E}^S = \vec{0}, \qquad \text{on } S_c. \tag{2.173}$$

The first expression in the right-hand side of this equation, namely $\vec{n}_c \times \vec{E}^I$, is equal to zero (see equation (2.8)). Therefore, the tangential components of the scattered electric field are also zero at the perfectly conducting surface S_c. This means that the second integral in the right-hand side of (2.170) vanishes. We arrive at the following expression

$$v^R i^T - v^T i^R = \int\int_{S_b} (\vec{E}^I \times \vec{H}^T - \vec{E}^T \times \vec{H}^I) \cdot \vec{n}_b dS. \tag{2.174}$$

The transmitted field is proportional to the input current i^T, provided that the antenna is linear with respect to the electromagnetic field quantities. Normalisation of the transmitted field to the input current results in the normalised field $(\vec{e}^T, \vec{h}^T)$. These normalised fields would be emitted if the antenna was fed with a unit current. Accordingly, equation (2.174) is rewritten as

$$\mathcal{E}^R = v^R - \mathrm{z} i^R = \int\int_{S_b} (\vec{E}^I \times \vec{h}^T - \vec{e}^T \times \vec{H}^I) \cdot \vec{n}_b dS, \tag{2.175}$$

where the impedance z of the antenna is given by the quotient of the port voltage and the port current in the transmitting state.

This equation can be interpreted as the Thévenin representation of the receiving antenna. The antenna is modelled as an ideal voltage source $\mathcal{E}^R$, represented by the integral over S_b, in series with the antenna impedance z. The Thévenin representation is presented by figure 2.15.

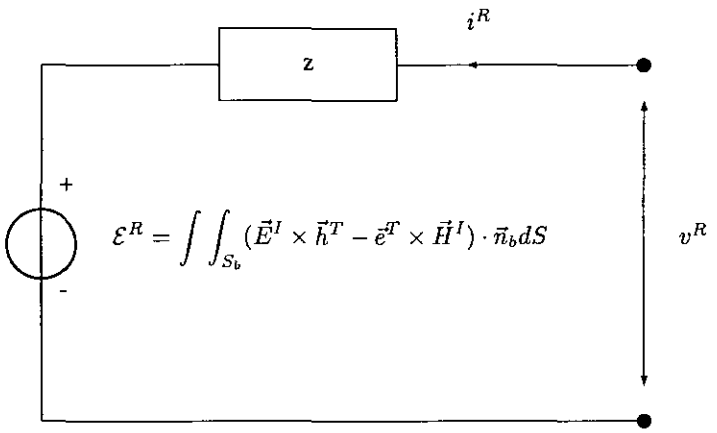

Figure 2.15: *The Thévenin representation for a receiving antenna*

In case multiple antennas are used at the receiving unit, the equivalent Thévenin representation is given by a N-port with internal voltage sources $\mathcal{E}_N^R$ and an internal impedance matrix Z_N.

In general, the integral in (2.175) must be evaluated in a numerical way. However, the received voltage of a half-wave dipole antenna will be calculated analytically. For this purpose, the surface S_b is chosen to coincide with the conductors of the antenna. In free space, the magnetic field on the conductors of a dipole connected to a source is known. Here, the same behaviour of the magnetic field is used for a receiving antenna placed inside a room with two dielectric walls. In [Leersum 95], it is shown that the current distribution of a half-wave dipole very close to a perfectly conducting wall resembles the free-space current distribution. The tangential part of the normalised magnetic field for an x-directed receiving antenna with wire radius ρ is

$$\vec{n}_b \times \vec{h}^T = \frac{\cos(k_2(x - x_r))}{2\pi\rho}\vec{e}_x, \tag{2.176}$$

with $-\lambda/4 \leq x - x_r \leq \lambda/4$. The coordinates of the centre of the antenna are given by (x_r, y_r, z_r).

Equation (2.175) can be rewritten as follows

$$\mathcal{E}^R = v^R - \mathrm{z}i^R = \int\int_{S_b} ((-\vec{n}_b \times \vec{h}^T) \cdot \vec{E}^I - (\vec{n}_b \times \vec{e}^T) \cdot \vec{H}^I) dS. \tag{2.177}$$

Using the boundary conditions on the perfect conductors of the receiving antenna gives $\vec{n}_b \times \vec{e}^T = \vec{0}$. Substitution of (2.177) in (2.176) results in

$$\mathcal{E}^R = v^R - \mathrm{z}i^R = -\int_{x_r-\lambda/4}^{x_r+\lambda/4} E_x^I \cos(k_2(x - x_r))dx. \tag{2.178}$$

The open circuit voltages will be calculated, this implies that the dipoles are not connected to a load or circuit; $i^R = 0$. We will assume that the transmitting antenna can be represented by a point source at the coordinates (x_s, y_s, z_s). This source is directed in the x-direction. Received voltages for other

directions of the source can be obtained in a similar way. Furthermore, we will only calculate v^R in the interval $0 \leq x \leq d_1$ (interval 1). The received voltages in the intervals 2 - 4 can be obtained in a similar manner. For a point source, the incident field upon the receiver is given by

$$E^I_{ix}(\vec{r}) = -j\omega G_{Eixx}(\vec{r}, \vec{r}_s). \tag{2.179}$$

Using equation (A.1), we can write

$$v^R = \frac{-4j\omega\mu_1}{bck_1^2} \int_{x_r-\lambda/4}^{x_r+\lambda/4} \sum_{m=1}^{\infty}\sum_{n=1}^{\infty} (k_1^2 - k_{1x}^2)\sin(k_{ym}y)\sin(k_{ym}y_s)\sin(k_{zn}z)\sin(k_{zn}z_s)\cdot \frac{\cos(k_{1x}x')\left[Z_{2mn}\sin(k_{2x}(x_s-d_2)) + k_{2x}\cos(k_{2x}(x_s-d_2))\right]\cos(k_2(x'-x_r))}{D_{mn}\cos(k_{1x}d_1)}dx'. \tag{2.180}$$

Assuming that term by term integration is permissible, we may write

$$v^R = \frac{-4j\omega\mu_1}{bck_1^2} \sum_{m=1}^{\infty}\sum_{n=1}^{\infty} \gamma(m,n) \int_{x_r-\lambda/4}^{x_r+\lambda/4} \cos(k_{1x}x')\cos(k_2(x'-x_r))dx', \tag{2.181}$$

with

$$\gamma(m,n) = (k_1^2 - k_{1x}^2)\sin(k_{ym}y)\sin(k_{ym}y_s)\sin(k_{zn}z)\sin(k_{zn}z_s)\cdot \frac{\left[Z_{2mn}\sin(k_{2x}(x_s-d_2)) + k_{2x}\cos(k_{2x}(x_s-d_2))\right]}{D_{mn}\cos(k_{1x}d_1)}. \tag{2.182}$$

Solving the integral in (2.181) and using some algebraic manipulations results in

$$v^R = \frac{8j\omega\mu_1 k_2}{bck_1^2} \sum_{m=1}^{\infty}\sum_{n=1}^{\infty} \gamma(m,n)\frac{\cos(k_{1x}x_r)\cos(k_{1x}\lambda/4)}{k_{1x}^2 - k_2^2}. \tag{2.183}$$

At this point, the received voltage of a half-wave dipole antenna due to a point source transmitter is obtained. Even though it will not be presented here, the received voltage due to a half-wave dipole transmitter can be calculated in a similar manner. In this case, the electric field which is described in section 2.6 must be substituted in (2.178). Thus, we are now able to calculate the electromagnetic fields caused by point-sources or half-wave dipoles. Furthermore, we are able to calculate the received voltages of point-sources and half-wave dipole receivers. If other antennas will be used, the voltage can be obtained by numerical integration in case the current on the antenna is known. The received voltage as a function of the receiver position inside the room will be presented in chapter 3. Furthermore, the voltages for multiple receiving antennas (diversity systems) will be shown in chapter 3. For this configuration, the equivalent Thévenin representation is given by a 2-port. We will neglect the mutual coupling between the antennas. This means that we will use the same current distribution on the multiple antennas.

2.7.2 Signal-to-noise ratio

In chapter 3 it will be shown that the electromagnetic fields vanish at some points inside the room. This can be explained by the fact that a standing-wave pattern will occur inside a room. If the receiving antenna is positioned at one of these points, the presence of even low level noise can seriously degrade the performance of the system. A measure of performance is given by the signal-to-noise ratio at the receiver output. This signal-to-noise ratio is a function of the position of the receiver inside the room.

By visualising the signal-to-noise ratio, it can be shown in which areas of the room problems might occur. The signal-to-noise ratio can be spatially averaged over all possible receiver locations. This value of the signal-to-noise ratio will be used as the basis for comparing the performances of various receivers inside the room.

The signal-to-noise ratio is calculated from the signal and the noise power levels. The signal power is obtained by calculating the received voltage at the receiver terminals. The noise power will be calculated at the load of the receiver. This can be explained by the fact that the signal is very weak at this point in the system. Thus, the additive noise at the receiver input will have considerable influence on the quality of the output signal. Further amplification of signal power will increase noise power also. We will assume that this noise can be modeled by a zero mean stationary , Gaussian random process.

We will calculate the time-average power that is fed into the receiving antenna system. Up to now we have obtained the open circuit voltages of a receiver. Because in this situation no current flows into the circuit, the delivered electromagnetic power is zero. Therefore we will terminate the antenna system with a perfectly matched load. In this way, there is a maximum power transfer from the transmission line into its load. The equivalent Thévenin representation is shown in figure 2.16.

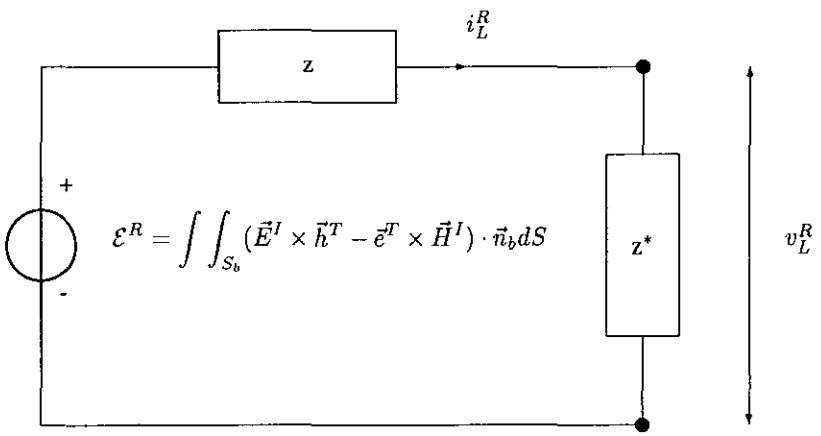

Figure 2.16: *The Thévenin representation for a receiving antenna with a characteristic load*

The current i_L^R is defined as the current flowing into the load. Therefore the currents i^R and i_L^R are related by $i_L^R = -i^R$. The time-average power that is dissipated in the load is given by

$$P_L = \frac{1}{2} Re\left\{v_L^R (i_L^R)^*\right\} = \frac{|\mathcal{E}^R|^2}{8Re(\mathrm{z})} = \frac{|\int\int_{S_b}((\vec{n}_b \times \vec{h}^T) \cdot \vec{E}^I + (\vec{n}_b \times \vec{e}^T) \cdot \vec{H}^I) dS|^2}{8Re(\mathrm{z})}. \tag{2.184}$$

Remember that the received voltage depends on the position of the receiver inside the room. Therefore, the received signal power is a function of the receiver position also.

The noise limits the rate of information transmission. The noise is an unwanted signal that can arise from a variety of sources. We will restrict the analysis to thermal noise, which is caused by the thermal motion of electrons in conducting media. The assumption is made that the noise may be described by a Gaussian process, which means that the amplitude-time distribution is Gaussian in nature. In many communication systems, this assumption is justifiable.

The power spectral density of thermal noise across the terminals of a resistor of value R is given by [Shanmugam 85]

$$G_v(f) = 4RkT \qquad \left[\frac{\mathrm{V}^2}{\mathrm{Hz}}\right]. \tag{2.185}$$

where k is the constant of Boltzman. The temperature of the resistor is denoted by T. In (2.185), the assumption is made that the power spectral density does not depend on the frequency f. This is valid for $|f| \leq 10^3$GHz, which is inside the range of the frequency used for our communication system. The noise power delivered to the characteristic load is written as

$$P_n = kTB, \tag{2.186}$$

where B is the noise bandwidth, which is taken the same as the bandwidth of the signal.

It is assumed that the message component and the noise component in the received signal are mutually independent. Then we may define the local signal-to-noise ratio as the local time-average signal power divided by the time-average noise power.

$$\frac{S}{N} = 10\log\frac{S_0}{N_0} = 10\log\frac{P_L}{P_n} = 10\log\frac{|\int\int_{S_b}((\vec{n}_b \times \vec{h}^T)\cdot\vec{E}^I + (\vec{n}_b \times \vec{e}^T)\cdot\vec{H}^I)dS|^2}{8kTBRe(\mathrm{z})}. \tag{2.187}$$

Note that we assume a Gaussian distribution for the noise component of the received signal. The message component of the signal is calculated by using the Green's function technique which is described in the previous sections. The received signal-to-noise ratio depends on the exact location of the receiving antenna which is shown clearly by measurements [Bot 93].

2.7.3 Bit error rate

Our primary goal is to develop antenna systems which will operate well in indoor environments. We will focus our attention on digital communication systems. Digital communication provides many advantages for transmitting and processing information such as improved quality of the signal. Furthermore, many services can be offered which are not available on an analogue system. For digital cordless systems many standards exist, for example [White 94]:

- CT2. This standard describes the second generation of cordless telephones. With this system, calls are made within 200 metres of a base station. The frequency is 865 MHz and the bit rate of this system is 72 kb/s.
- PCN (Personal Communication Network). The new standard for PCN based on GSM is known as DCS 1800. PCN is intended for both speech and data services at home and in business. The frequency is 1.8 GHz and the bit rate is 270.8 kb/s.
- PHS (Personal Handy Phone System). This standard is used in Japan. The frequency is 1.9 GHz and the bit rate is 384 kb/s.
- DECT (Digital European Cordless Telephone System). DECT is specified to provide a wide area of applications such as voice, data and ISDN services. DECT is also intended for indoor communication. The frequency is 1.9 GHz and it uses a bit rate of 1.152 Mb/s.

The performance of these systems are measured by the probability of error. We will calculate the bit error rate for DECT systems operating in an indoor environment.

The DECT receiver is based on noncoherent FSK (frequency-shift keying) [Wittneben 94]. The frequency of the carrier is changed to switch between the various waveforms. In the FSK modulation scheme, two waveforms are used to represent the binary digits '0' and '1'. These waveforms are given by

$$s_1(t) = A\cos(\omega_c t - \omega_d t), \qquad s_2(t) = A\cos(\omega_c t + \omega_d t). \tag{2.188}$$

For coherent detection, a phase coherent local carrier is needed to receive the signal. Noncoherent detection systems do not require a phase coherent local oscillator signal. The signal will be detected in the receiver by using two bandpass filters with center frequencies $f_c + f_d$ and $f_c - f_d$. In this way, the two signals $s_1(t)$ and $s_2(t)$ can be distinguished. In FSK systems, the filter bandwidth B is usually $2r_b$, in which r_b denotes the bit rate [Shanmugam 85]. However, in DECT systems Gaussian-filtered frequency shift keying is used with a bandwidth of half the bit-rate. Thus, the filter bandwidth is $\frac{1}{2}r_b$. The noncoherent FSK receiver is shown in figure 2.17.

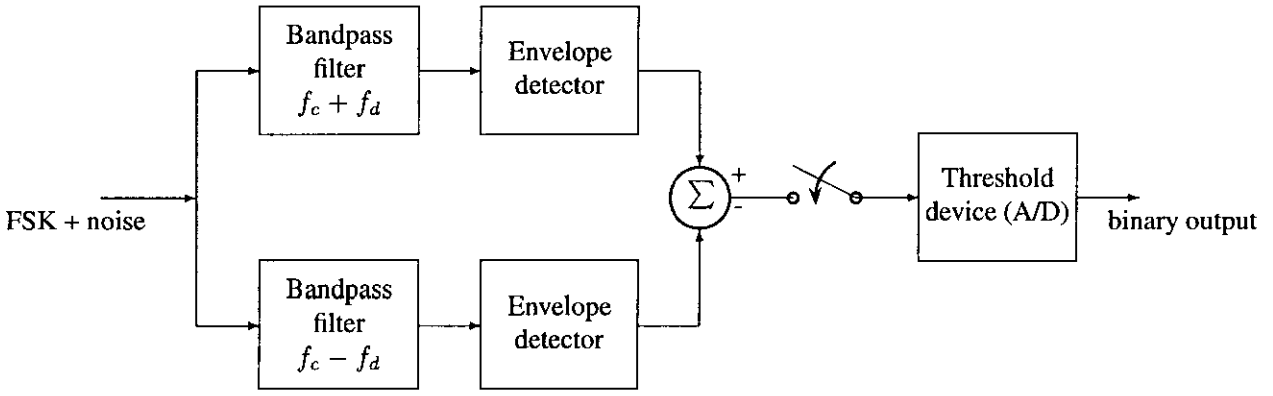

Figure 2.17: *Noncoherent demodulation of binary FSK signals*

Due to symmetry, the threshold is set at zero. The bit error rate is given by [Shanmugam 85]

$$P_e = \frac{1}{2}\exp -\frac{A^2}{4kTB}. \tag{2.189}$$

This formula will be rewritten using the definition of the signal-to-noise ratio. In (2.189), the average signal power is $A^2/2$. In our description, the average received power in the characteristic load of the antenna is $|\mathcal{E}^R|^2/8Re(\mathrm{z})$. We may write

$$P_e = \frac{1}{2}\exp -\frac{|\mathcal{E}^R|^2}{16kTBRe(\mathrm{z})} = \frac{1}{2}\exp \frac{-S_0}{2N_0}, \tag{2.190}$$

where the local signal-to-noise ratio S_0/N_0 is defined in section 2.7.2. Substitution of (2.187) in (2.190) gives

$$P_e = \frac{1}{2}\exp \frac{-|\int\int_{S_b}((\vec{n}_b \times \vec{h}^T)\cdot\vec{E}^I + (\vec{n}_b \times \vec{e}^T)\cdot\vec{H}^I)dS|^2}{16kTBRe(\mathrm{z})}. \tag{2.191}$$

The bit error rate depends on the location of the receiving antenna. The calculation of the bit error rates for diversity systems is carried out in such a way that the voltages of the multiple antennas are combined. The signal-to-noise ratio and the bit error rate are calculated using the voltages and the noise power.

The following figure shows the probability of error P_e of a noncoherent GFSK (Gaussian frequency shift keying) receiver versus the signal-to-noise ratio for a non-fading environment.

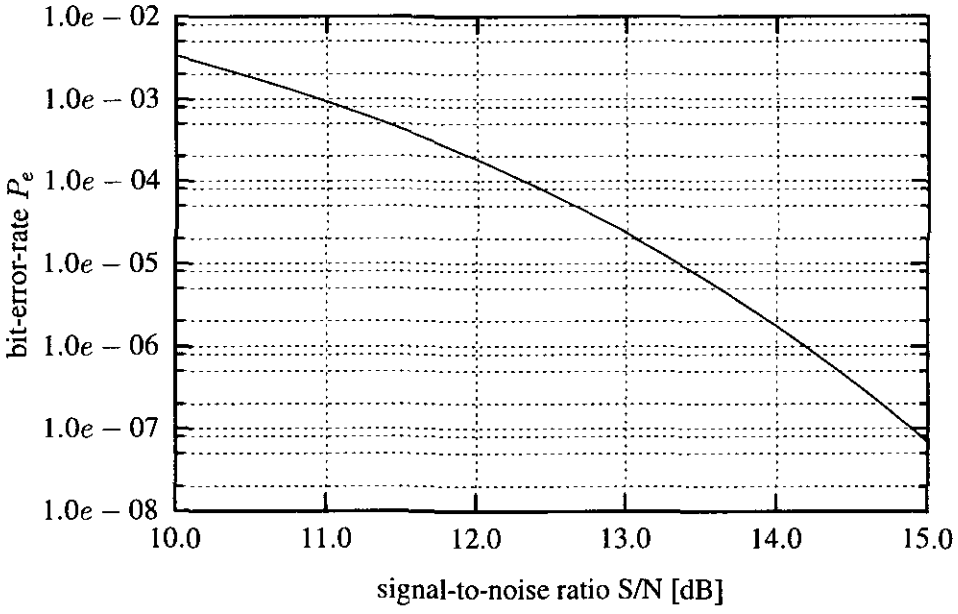

Figure 2.18: *Bit error rate versus signal-to-noise ratio for FSK*

The voltages and signal-to-noise ratios of various diversity receivers are calculated in chapter 3.

Chapter 3

Results

3.1 Introduction

Four quantities will be calculated in this chapter; electric fields, received port voltages, signal-to-noise ratios and bit error rates.

The electric field due to a point-source and a half-wave dipole antenna are presented in this chapter. The field pattern inside a room with perfectly conducting walls is compared to the electromagnetic field inside a room with two dielectric walls.

The received voltage of a half-wave dipole antenna will be presented as a function of the position of the receiver inside the room. It will be shown that the received voltages can be very low at some points inside the room. Space diversity can be used to improve the performance of a receiving system. The voltages received by a space diversity receiver, which combines the voltages in several ways (e.g. equal gain combining, maximal ratio combining, selection diversity and switch diversity), are shown in section 3.6.

Finally, the signal-to-noise ratios and the bit error rates of the various diversity receivers are compared to each other.

3.2 Electromagnetic fields inside a room due to a point source

Our main interest concerns the analysis of the fundamental processes of wave propagation inside a room. The fields inside a room will be subject of study in order to obtain insight in the problems that can arise in an indoor environment. In [Dolmans 95], the electromagnetic fields inside a room with perfectly conducting walls have been discussed. In such a configuration, the amplitudes of the electromagnetic fields change rapidly. This means that the electromagnetic fields vanish at some points inside the room. However, the mean value of the electromagnetic fields in a highly reflecting room is larger than the corresponding value in a room with lossy, dielectric walls. These high electric fields can be used to enhance internal communications, therefore, it is reported that some buildings are now being built with shielding materials embedded in their structure [Moriyama 92]. We will make a comparison between the fields inside a highly reflecting room and inside a room with lossy, dielectric walls. In this way, the effect of absorption and scattering of the electromagnetic fields at a dielectric wall can be examined. The first configuration consists of a room with perfectly conducting walls. The dimensions of the room, the location of the source, the observation line and the frequency are given in table 3.1.

dimensions	location point source	observation line	frequency
$a = 5$ m	$x_s = 0.752$ m	$0 \leq x \leq 5$ m	$f = 2$ GHz
$b = 4$ m	$y_s = 0.202$ m	$y = 1.6$ m	
$c = 3$ m	$z_s = 0.4$ m	$z = 2.26$ m	

Table 3.1: *Parameters perfectly conducting room*

An x-directed electric point source is used as transmitting antenna. The absolute values of the electric field in the orthogonal directions are presented in the following figures.

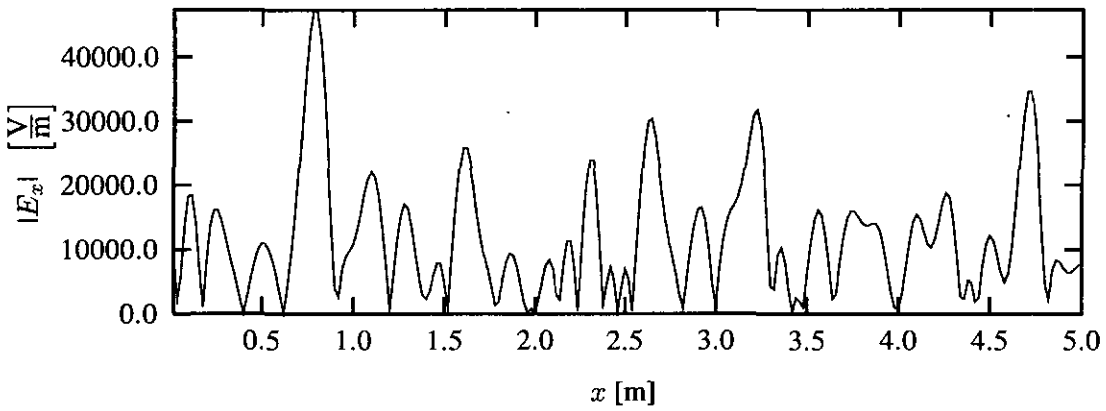

Figure 3.1: *Electric field* $|E_x|$

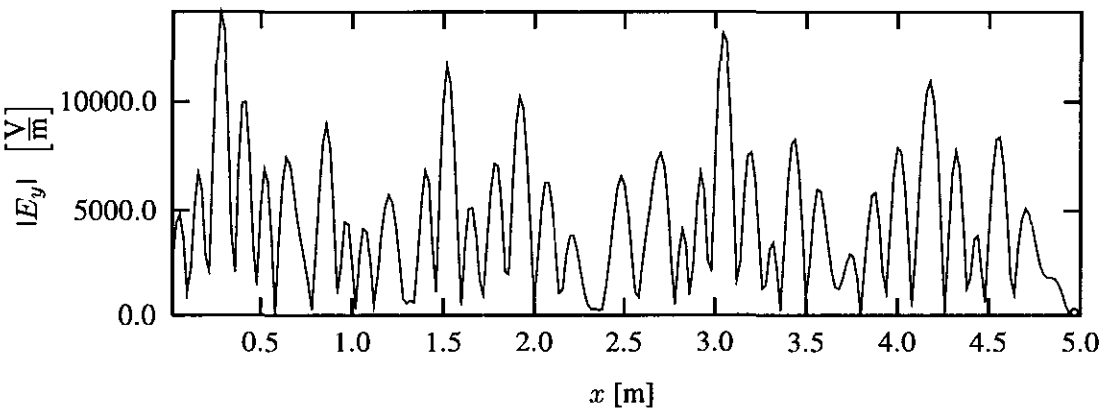

Figure 3.2: *Electric field* $|E_y|$

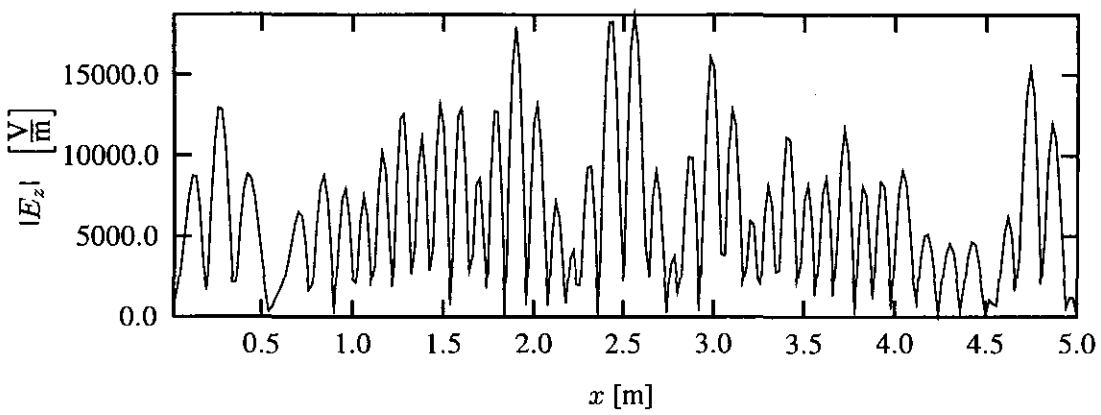

Figure 3.3: *Electric field* $|E_z|$

The three figures show clearly that the absolute value of the electric field changes rapidly. It is obvious that the electric fields vanish at some points inside the room. Similar to wave propagation in free space, the electric field in the same direction as the source (in this case x- direction) is very strong. The magnetic field and the vector of Poynting have been presented in [Dolmans 95] and [Kant 94].

The electric field inside a room with two dielectric walls will be presented. The electric fields of the two configurations are compared to each other. In this way, the scattering and the absorption of the electromagnetic fields at the dielectric walls can be investigated. The configuration which is described in table 3.1 will be used. At the two walls, dielectric layers are present with thicknesses d_1 and $a - d_2$. The dielectric materials described in [Kant 94] have been used. The real part and the imaginary part of the relative permittivities of the dielectric walls are equal to 4.5 and 0.13, respectively.

dimensions	point source	observation line	dielectric walls	frequency
$a = 5$ m	$x_s = 0.752$ m	$0 \leq x \leq 5$ m	$\epsilon_1' = 4.5$, $\epsilon_1'' = 0.13$, $d_1 = 40$ cm	$f = 2$ GHz
$b = 4$ m	$y_s = 0.202$ m	$y = 1.6$ m	$\epsilon_2' = 4.5$, $\epsilon_2'' = 0.13$, $a - d_2 = 40$ cm	
$c = 3$ m	$z_s = 0.4$ m	$z = 2.26$ m		

Table 3.2: *Parameters room with two dielectric walls*

The electric field due to a point source in the x-direction is presented in the following figures. The maximal values of the electric fields inside the dielectric walls are much lower than the maximal values of the field inside the room. Just like in free-space propagation, the electric field in the x-direction is larger than the electric fields in the other two directions. The maximal values of the electric field in the dielectric configuration are much lower than the corresponding peak values in the perfectly conducting room. Furthermore, the number of points inside the room where the electric fields completely vanish is decreased considerably. It can be concluded that the dynamic range (difference between maximal and minimal field values) is reduced due to the presence of the dielectric walls.

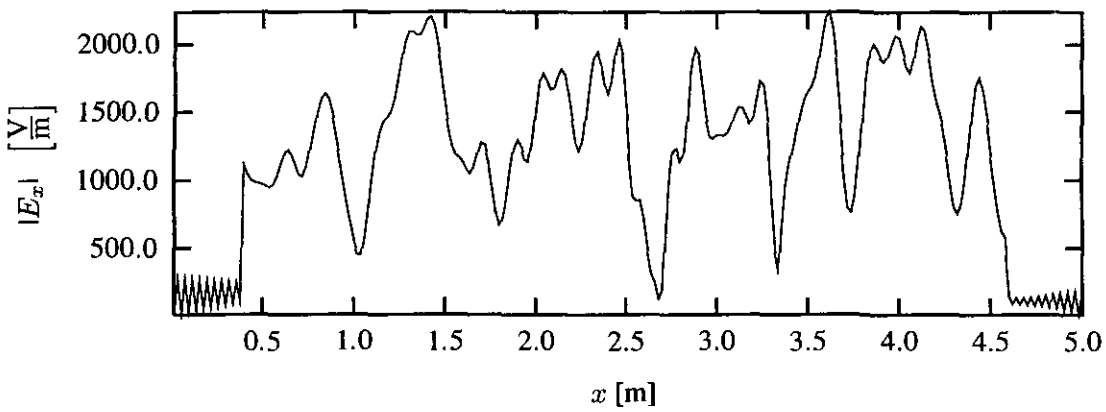

Figure 3.4: *Electric field* $|E_x|$

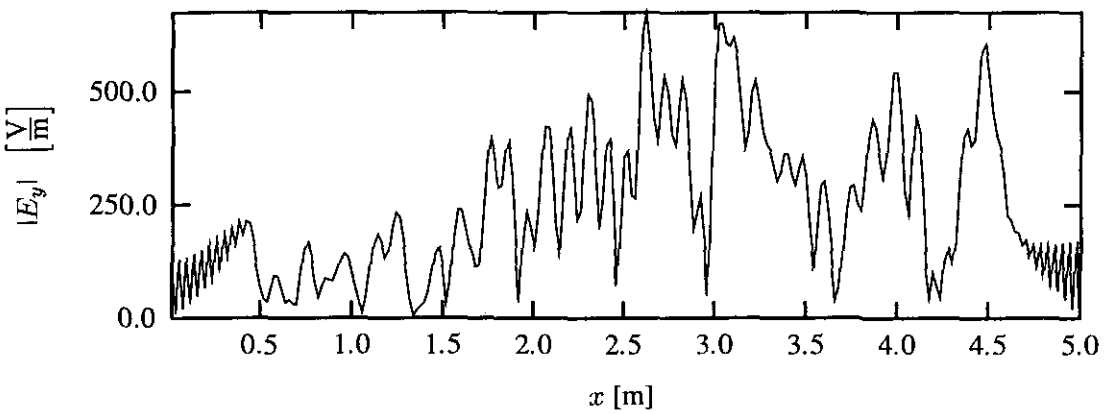

Figure 3.5: *Electric field* $|E_y|$

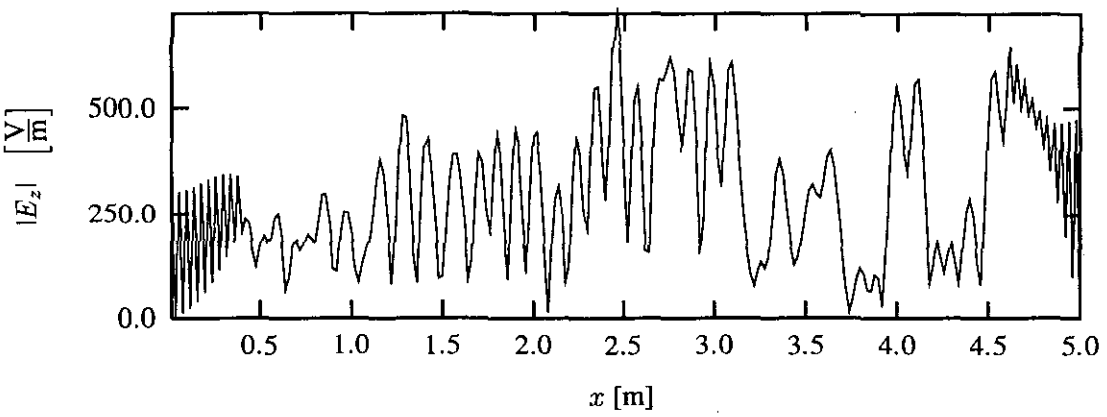

Figure 3.6: *Electric field* $|E_z|$

The next comparison will be made between the electric fields of the two configurations in an observation plane. The dimensions of the room and the location of the source are not changed. The observation plane is given by $0 \leq x \leq 5$m, $0 \leq y \leq 4$m, $z = 2.26$m. The maximal and mean values of the three components of the electric field inside the observation plane are given in table 3.3.

field component	mean value	maximal value
$\|E_x\|$	13131 V/m	65887 V/m
$\|E_y\|$	3794 V/m	19826 V/m
$\|E_z\|$	7057 V/m	29369 V/m

Table 3.3: *Mean and maximal electric field inside a perfectly conducting room*

The same calculation is done for the electric field inside the room with two dielectric walls. The maximal and mean values are presented in table 3.4.

field component	mean value	maximal value
$\|E_x\|$	1334 V/m	6294 V/m
$\|E_y\|$	236 V/m	1100 V/m
$\|E_z\|$	272 V/m	1550 V/m

Table 3.4: *Mean and maximal electric field inside a room with two dielectric walls*

Notice that the electric fields are very high inside the room, caused by the moment of the dipole which is equal to unity. We are only interested in comparing the various responses of the configurations, therefore the strength of the source is not important for our analysis. The dimensions of the observation plane are very large compared to the wavelength (33 λ x 27 λ). Due to the irregular field pattern, it is difficult to show the electric field inside such a large observation plane. For this purpose, colour graphs are used for plotting the absolute value of the dominant electric field E_x. The electric field in the observation plane of a room with perfectly conducting walls is shown in figure 3.7. The electric field inside a room with two lossy, dielectric walls is presented in figure 3.8. In these pictures, the colour represents the amplitude of the electric field. A receiver located in a blue region of the picture suffers from the fact that the electromagnetic energy is very low. For several applications, the quality of the received signal can be too low in these regions. The field pattern is normalised to the peak value. In the two pictures, the electric fields are normalised to the peak values E_x = 65887 V/m and E_x = 6294 V/m, respectively. The low values of the field inside a dielectric wall are shown clearly in figure 3.8. Furthermore, it is evident from the two colour graphs that the field inside a perfectly conducting room is much more irregular than the field inside a room with two dielectric walls.

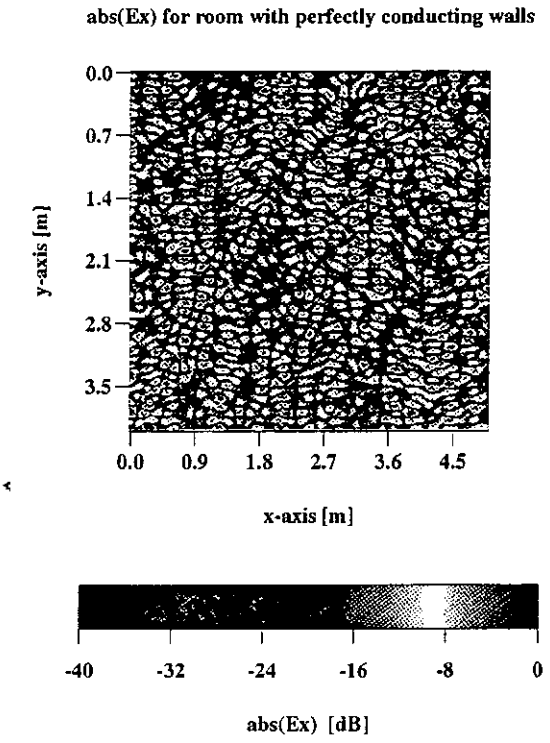

Figure 3.7: $|E_x|$ *in a room with perfectly conducting walls*

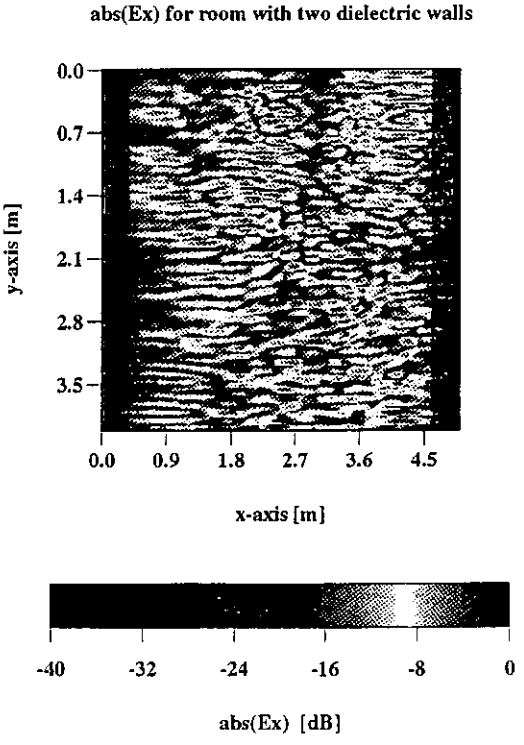

Figure 3.8: $|E_x|$ *in a room with two dielectric walls*

3.3 Electromagnetic fields inside a room due to a half-wave dipole

In the previous section, the electromagnetic fields due to a point-source transmitter have been investigated. A more realistic source is the half-wave dipole antenna. The fields of this transmitter inside a room with two dielectric walls are obtained by using the results of section 2.6.

The configuration is presented by table 3.1. The centre of the half-wave dipole is given by the coordinates (x_s, y_s, z_s) and the length of the antenna is 7.5 cm. The location of the centre of the antenna will be called 'position A'. The antenna is directed in the x-direction. The y-component of the electric field is shown in figure 3.9.

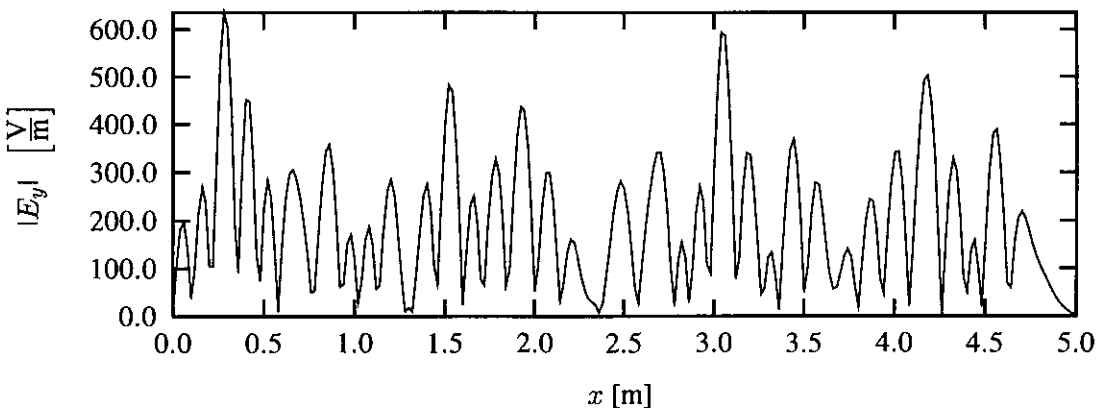

Figure 3.9: *Electric field $|E_y|$ caused by a half-wave dipole at position A*

Note that the figures 3.9 and 3.2 are very similar, only the amplitudes differ from each other. The similarity between the two figures can be explained from the fact that the room is very resonant. This means that only a few terms of the double series contribute to the electric field. Furthermore, the formulas for the two types of sources (for example 2.159 and A.1) are comparable. Consequently, the electric fields generated by the two types of sources can be the same, even for non-resonant structures.

The differences between the amplitudes of the figures 3.9 and 3.2 are caused by the differences in radiated power levels. The current density on the point-source is 1 A/m^2. According to [Jeuken 88], the radiated power is 10 k_0^2 Watt (k_0 is the wave number in free space). This formula is only valid for free-space propagation and it makes use of the assumption that the observation point is located in the far field region. However, the total radiated power in a large room can be approximated by the free-space radiated power. For our configuration, the total radiated power of a point source is 17545 Watt. The total power radiated by a half-wave antenna is $\frac{1}{2}|I_0|^2 \mathrm{R_a}$. The real part of the antenna impedance is denoted by $\mathrm{R_a}$. For our configuration, the amplitude of the current I_0 is 1 A and the total radiated power is 36.5 Watt. It can be concluded that the point source radiates 480 times more power than the half-wave dipole. The average electric field in the room caused by a half-wave dipole will be $\sqrt{480} = 22$ times less than the average field caused by a point source. This is the reason that the figures 3.9 and 3.2 differ much in the amplitudes of the electric fields.

The field caused by multiple transmitters can be found by using the superposition principle. For example, the field caused by one source will be added with the field caused by another source. In order to use this principle, it will be assumed that the coupling is negligible between the two sources.

This means that the same current on the two antennas will be used. Diversity at the base station can be used to reduce performance loss. In this way, the mobile receiving system can be kept simple. For DECT systems, this can be realised by signal measurements in preceding time slots. Using the two antennas simultaneously, the transmitting power will be increased. Therefore, it is common practice to use the antenna with the largest signal strength for transmission in the next time slot [Wittneben 94]. The selection of the antenna is based on the observations of the received signals at the different antennas. The effect of diversity will be demonstrated by using a second antenna spaced $\lambda/2$ apart from the first antenna. The y-component of the electric field is shown in figure 3.10.

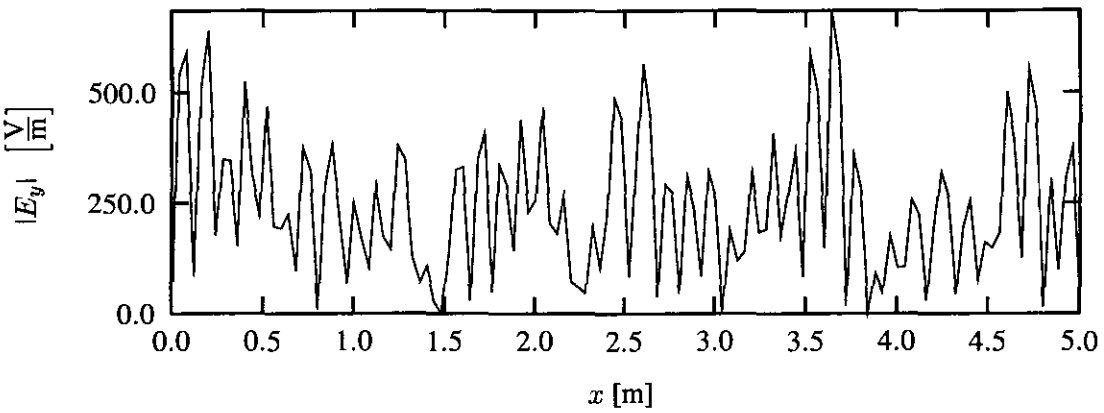

Figure 3.10: *Electric field $|E_y|$ caused by a half-wave dipole at position B*

Notice that in general the fades in figure 3.9 do not correspond to the fades in figure 3.10. Thus, the performance can be improved by using transmit antenna selection diversity. However, we will not focus on this kind of diversity. In section 3.6, the performance of diversity systems at the receiving part of the communication link will be discussed.

3.4 Port voltage of a half-wave dipole antenna

It has been shown that the electromagnetic fields are very irregular inside a room. Some buildings are now being built with shielding materials embedded in their structure to enhance internal communications [Moriyama 92]. However, most manufacturers want to provide indoor communication systems with an acceptable quality in conventional buildings. For this purpose, it is necessary to investigate methods for reducing the rapid signal variations in the mobile radio transmission path. The quality of the telecommunication link can be improved by developing new antenna systems, for example multi-element antenna arrays. To design new antenna systems, the interaction between the electromagnetic fields and the type of antenna must be modelled. In section 2.7, a Thévenin representation is obtained by using the Lorentz reciprocity theorem. The received voltage is calculated using the Thévenin representation. The induced voltage on the antenna port is not only a function of the electromagnetic field in the room. The voltage depends on the polarisation of the antenna and the current distribution on the antenna also.

The received voltage of a half-wave dipole antenna, positioned inside a room with two dielectric walls, will be calculated in a vertical plane inside the room. The radiated power of the transmitter (point source) is 200 mW and the frequency is 2 GHz.

The configuration is presented in figure 3.11 and table 3.5. The point source and the half-wave dipole receiver are directed into the x-direction. The received voltage changes rapidly in the observation plane. The absolute values of the mean and maximal received voltage in the observation plane are 0.28 Volt and 1.87 Volt, respectively. The voltage in a part of the observation plane, namely $1\text{m} < x < 3\text{m}$, $1.5\text{m} < z < 2\text{m}$, is presented in figure 3.12.

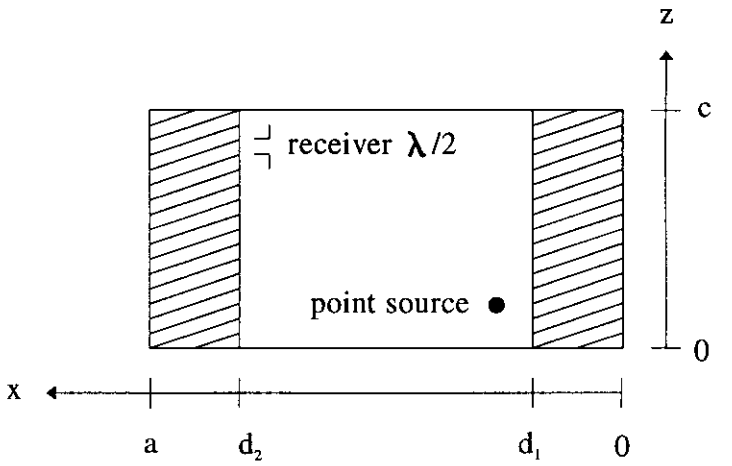

Figure 3.11: *Side view*

dimensions	point source	observation plane	dielectric walls
$a = 5.13$ m	$x_s = 0.752$ m	$0 \leq x \leq a$	$\epsilon_1' = 4.5$, $\epsilon_1'' = 0.13$, $d_1 = 40$ cm
$b = 4.04$ m	$y_s = 0.202$ m	$y = 0.35$ m	$\epsilon_2' = 4.5$, $\epsilon_2'' = 0.13$, $a - d_2 = 40$ cm
$c = 3.02$ m	$z_s = 0.4$ m	$0 \leq z \leq c$	

Table 3.5: *Parameters room with two dielectric walls*

It is obvious from figure 3.12 that the received voltage almost vanishes at some points inside the room. As indicated in chapter 2, the received voltage is proportional to the integral over the antenna surface of the total incident field at each location. Unfortunately, very small antennas must be used for indoor communication in order to minimize the size of the mobile unit, therefore, multipath fading is a severe problem in mobile telecommunication links. An antenna system located in a fade will not function properly. The rapid signal variations can be reduced by using multiple antenna systems. In the next section, diversity techniques for improving the average signal strength inside an indoor environment will be discussed.

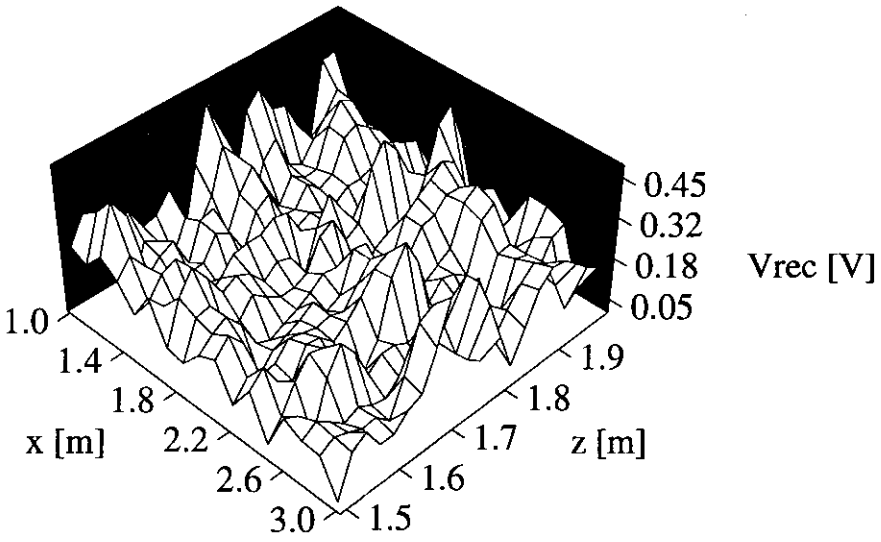

Figure 3.12: *Received voltage*

3.5 Classification of diversity systems

The previous sections have shown that there are rapid variations in electromagnetic fields and received voltages inside a room. We will now consider methods of reducing these signal fluctuations in such a way that acceptable transmission of data is obtained. The classical way for reducing the effect of fading is to transmit a signal from a single antenna to a number of receiving antennas. The distance is made large enough to ensure independent fading. This kind of diversity is called space-diversity reception. The transmitting and receiving antennas can be interchanged, resulting in space-diversity transmission (shown in section 3.3). Other diversity techniques than spaced antennas have been invented. The basic diversity classifications are given by [Jakes 93]

- Space diversity. The spacing of the multiple antennas is often larger than $\lambda/2$ for obtaining uncorrelated signals at the receiver. Space diversity will be extensively studied in this chapter.
- Polarisation diversity. Signals which are transmitted on two orthogonal polarisations can be received separately with this kind of diversity. The spacing between the antennas may be minimized by the fact that orthogonality is sufficient to obtain uncorrelated signals.
- Angle diversity. The receiver consists of highly directive antennas pointing in different directions.
- Frequency diversity. Several frequencies are used to achieve uncorrelated signals. The number of antennas can be reduced; on the other hand a greater part of the frequency spectrum will be used. Furthermore, multiple transmitters will be required to generate the various frequencies.
- Time diversity. The samples will be separated sufficiently in time in order to obtain uncorrelated signals.

Space, polarisation and angle diversity schemes require multiple antennas. The received voltage (or current) of each antenna can be combined in many different ways. We may distinguish between [Jakes 93], [Lee 82], [Freeman 87]

Selection diversity

This is a simple method for combining the received voltages of multiple antennas. The output of one antenna at a time will be used. The antenna having the highest signal-to-noise ratio is connected to the remainder of the circuit. In practice, the antenna with the largest signal plus noise power level is used, since it is difficult to measure the signal-to-noise ratio. The selection combiner is presented in figure 3.13.

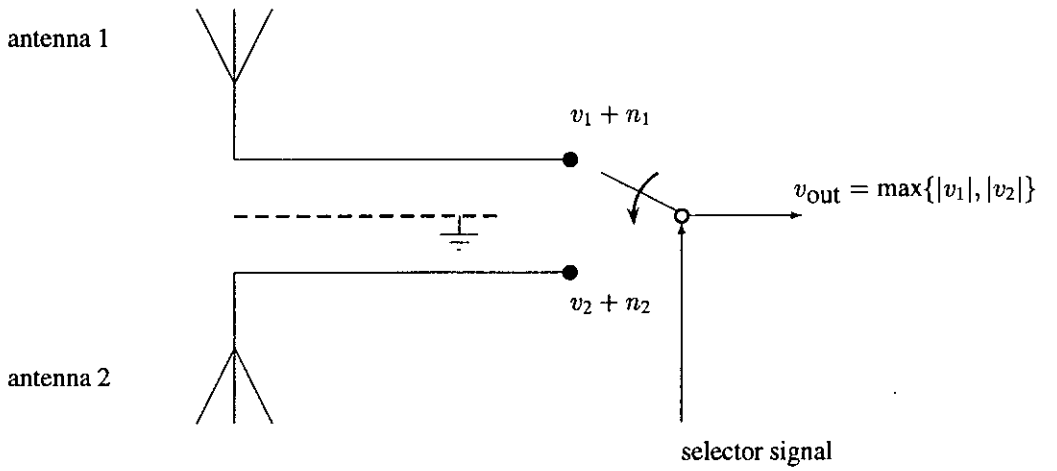

Figure 3.13: *Selection diversity*

Using selection diversity, the received voltage is equal to the maximal value of the voltages of the two antennas. Selective combining is difficult to implement, because a floating threshold level is needed. A more practical technique is switched combining [Lee 82].

Switch diversity

This kind of diversity makes use of a switch-and-stay strategy. One antenna with an output voltage v_1 or v_2 is used until the signal level drops below a predetermined threshold A. Then, the antenna switch is activated, selecting the other antenna. If this antenna is also positioned in a fade, the switch is not activated again in order to avoid excessive switching. If rapid switching is tolerated, the strategy will be called switch-and-examine strategy. The switched-combined signal performs worse than the selective combined signal, except at the threshold level. The switch combiner is presented in figure 3.14. The switch strategy is shown in the right part of the figure. Depending on the previous state of the switch and the strength of the received signal in the two branches, the switch can be activated.

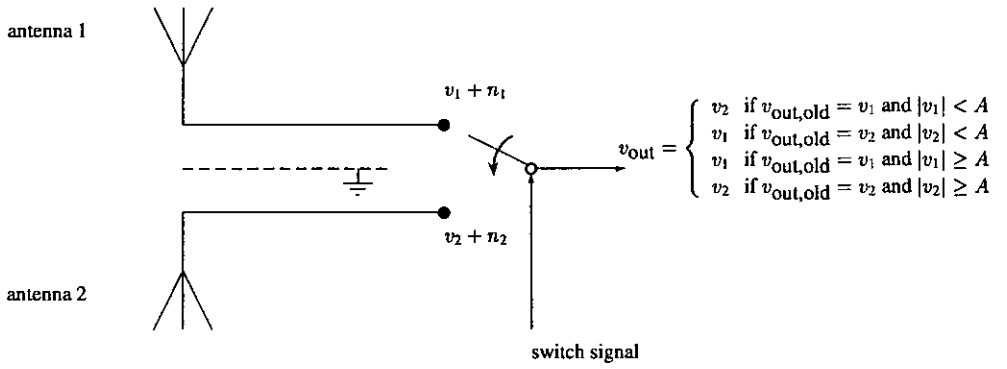

Figure 3.14: *Switch diversity*

Maximal-ratio combining

In maximal-ratio combining, the signals are added up, each weighted with the complex conjugate of the received signals. This combining technique is presented in figure 3.15.

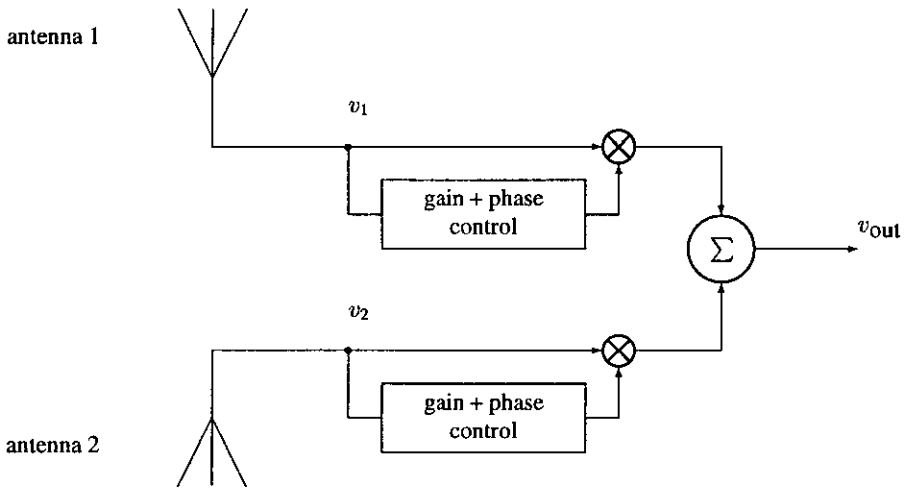

Figure 3.15: *Maximal ratio combining*

The output of the diversity receiver can be written as

$$v_{out}^2 = (v_1 + n_1)v_1^* + (v_2 + n_2)v_2^*, \tag{3.1}$$

where v_i^* denotes the complex conjugate of the received voltage at the receiving antenna i. The noise component of the signal in branch i is represented by n_i. This combining technique is an optimal technique; however, it is difficult to achieve the correct weighting factors. It is difficult to realize a cophasing circuit having a precise and stable tracking performance in a rapidly changing, random-phase, multipath fading environment [Feher 95]. Therefore, costly design is required for using this technique. If no gain control can be used, equal gain combining may be a solution to this problem.

Equal-gain combining

The gains of the maximal ratio combiner are all set to a constant value of unity, resulting in an equal-gain combiner. The detection of the signals is obtained by using a simple phase-locked summing circuit. The output of the receiver is given by

$$v_{\text{out}} = \frac{(v_1 + n_1)v_1^*}{|v_1|} + \frac{(v_2 + n_2)v_2^*}{|v_2|}. \tag{3.2}$$

There are many other combining techniques; for example using pilot signals, scanning diversity, etc. These techniques are not mentioned here for the sake of brevity. In the next section, the received voltages for the four combining techniques will be calculated as a function of the location of the receiver.

3.6 Received voltage of four space-diversity receivers

In this section, the four diversity receivers will be compared to each other. The received voltages (without load) in a room with two dielectric walls will be calculated using the analysis described in chapter two. The configuration is presented in table 3.6.

dimensions	point source	observation plane	dielectric walls
$a = 5.13$ m	$x_s = 0.752$ m	$0 \leq x \leq a$	$\epsilon_1' = 4.5$, $\epsilon_1'' = 0.13$, $d_1 = 40$ cm
$b = 4.04$ m	$y_s = 0.202$ m	$y = 0.35$ m	$\epsilon_2' = 4.5$, $\epsilon_2'' = 0.13$, $a - d_2 = 40$ cm
$c = 3.02$ m	$z_s = 0.4$ m	$0 \leq z \leq c$	

Table 3.6: *Parameters room with two dielectric walls*

The observation plane is given by $0 < x < a$, $y = 0.35$m, $0 < z < c$. The received voltages of the diversity receivers are normalised to the port voltage of the x-directed point-source transmitter. The radiated power of the transmitter is 200 mW and the frequency is 2 GHz. The absolute value of the received voltage of a single half-wave dipole antenna is shown in the first figure. Although the voltages are calculated in the entire observation plane, only a section of this plane is presented, namely $1\text{m} < x < 3\text{m}$, $y = 0.35\text{m}$ and $1.5\text{m} < z < 2\text{m}$.

The received voltage is more than 55 dB below the voltage of the transmitter in the black regions. There is a great possibility that an antenna located in such a region does not function properly. Using a space-diversity antenna system, the second antenna might receive a better signal. The received voltages of four diversity systems (x-directed antennas spaced $\lambda/2$ apart) are shown in the following figures. It is assumed that the coupling between the antennas is negligible. Thus, the same current distribution is used on both antennas.

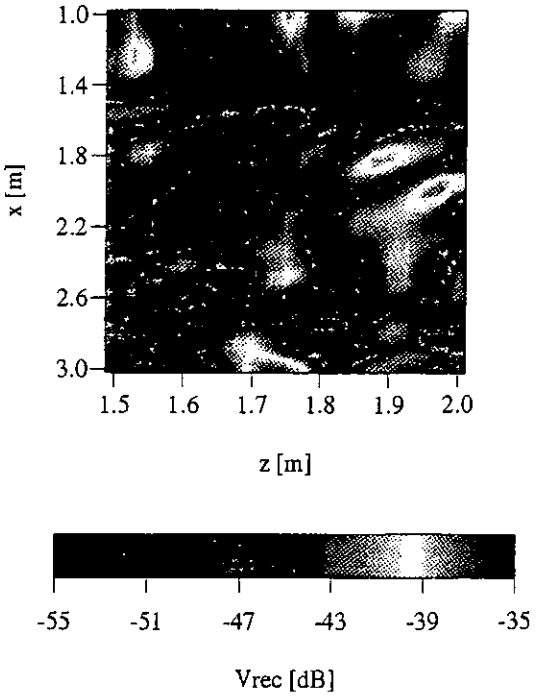

Figure 3.16: *Voltage of half wave dipole antenna*

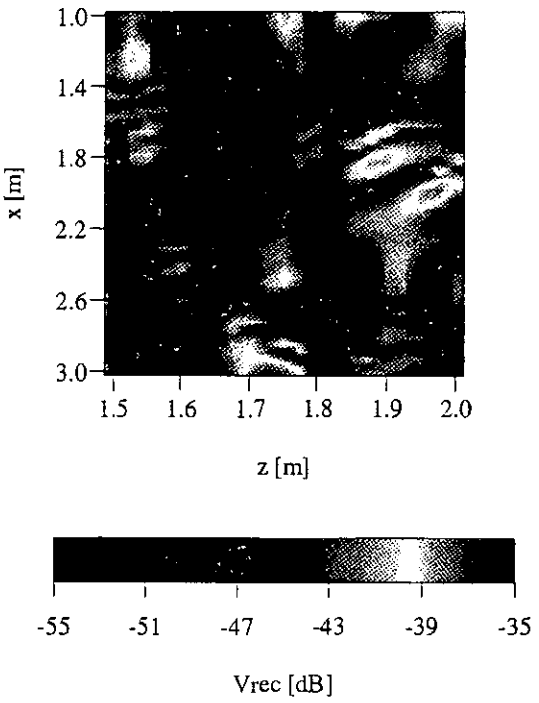

Figure 3.17: *Switch diversity*

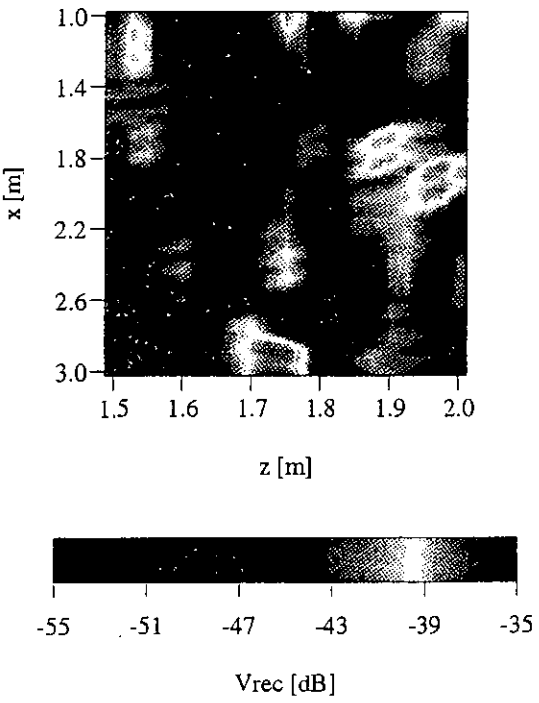

Figure 3.18: *Selection diversity*

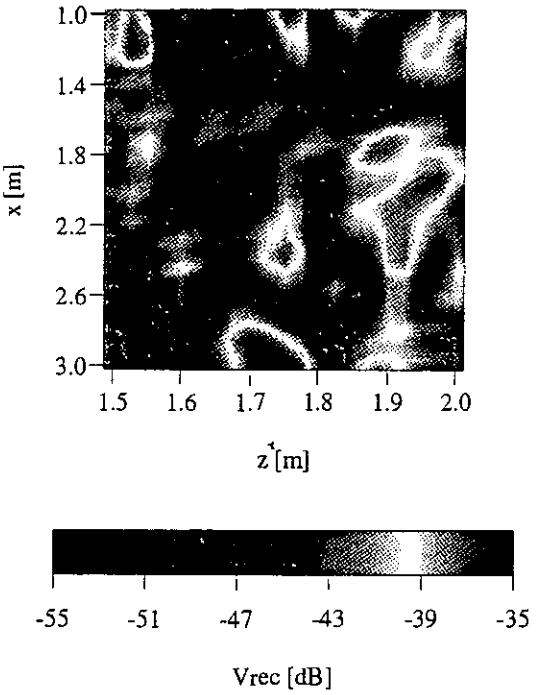

Figure 3.19: *Equal gain combining*

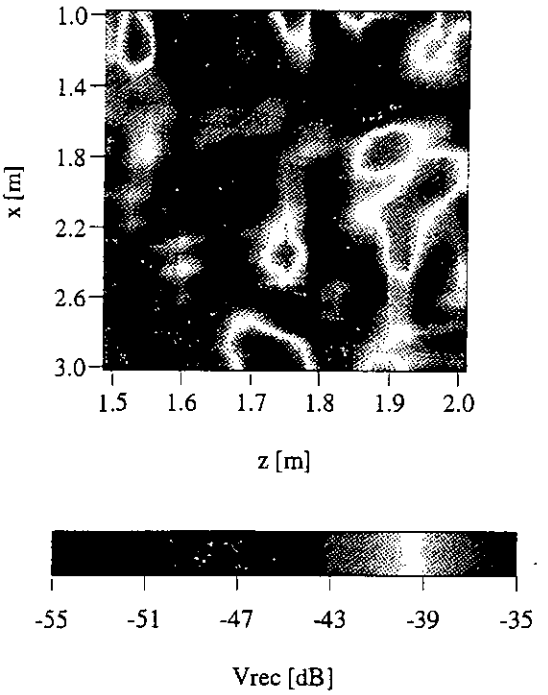

Figure 3.20: *Maximal ratio combining*

The total noise power of the equal gain combiner and the maximal ratio combiner exceeds the noise power of a single antenna receiver. The differences in noise power have been subtracted from the received voltage. In this way, the four figures can be compared to each other.

The received voltage has been calculated for all receiver positions in the observation plane. The average signal level is improved by using diversity systems. The gains obtained by the four diversity techniques are shown in table 3.7.

switch diversity	selection diversity	equal gain combining	maximal ratio combining
1.01 dB	1.87 dB	3.22 dB	3.53 dB

Table 3.7: *Gains of the four diversity techniques*

As expected, the optimal combining method is the maximal ratio combiner. The slightest improvement is obtained by using switch diversity compared to the other three diversity systems ; however, switch diversity is easy to implement. The performances of the four diversity techniques calculated by the Green's function technique and the Lorentz reciprocity theorem resemble the results of [Jakes 93, p. 317].

Although the average signal level is improved by only a few decibels, the number of regions with a signal level below -50 dB is decreased. The sizes of these regions as a percentage of the size of the observation plane are presented in table 3.8.

single antenna	switch diversity	selection diversity	equal gain combining	max. ratio combining
23.5 %	14 %	7.7 %	4.7 %	3.4 %

Table 3.8: *Sizes of the regions with* $|v| <$ *-50 dB*

3.7 Bit error rates and signal-to-noise ratios in a large room

The average signal-to-noise ratio is very high in a small room with a line of sight connection between the transmitter and the receiver. Due to this fact, the average quality of the telecommunication link inside such a small room is excellent. However, an antenna positioned in a deep fade inside the room can still receive too less electromagnetic energy to function properly.

The indoor signal strength and the bit error rate inside a large room (with an obstacle) have been presented in [Lawton 93]. Using a ray-tracing technique, the authors found that even with diversity techniques very high error rates were obtained. To compare these results with our model, we will consider the electromagnetic fields and the received voltages inside a large room. Remember that in section 2.5 the conclusion was drawn that the truncation error for the Green's function is not depending on the length of the room. This means that we are able to calculate the fields inside a large room without any extra computational effort.

The dimensions of the room, the location of the source, the observation line and the frequency are presented in table 3.9.

dimensions	location point source	observation line	frequency
$a = 25$ m	$x_s = 3.5$ m	10 m $\leq x \leq$ 11.5 m	$f = 2$ GHz
$b = 4$ m	$y_s = 0.2$ m	$y = 2.5$ m	
$c = 3$ m	$z_s = 0.4$ m	$z = 1.8$ m	

Table 3.9: *Room configuration*

The thicknesses of the two walls are 1 m and the permittivities of the walls are $\epsilon_r = 4.5 - j0.13$. Due to the perfectly conducting walls, no energy will flow outside the room. It can be expected that the mean signal strength will exceed the signal strength presented in [Lawton 93]. Therefore, the dielectric walls are very thick in order to simulate the losses for an indoor telecommunication link.

The room consists of free space with permittivity ϵ_0 and permeability μ_0. The radiated power P_t of the x-directed transmitter is 200 mW. The strength of the point source is $\sqrt{\frac{P_t}{10k_0^2}} = 3.376 \text{ x } 10^{-3}$ [Am]. The absolute value of the received voltage along the observation line is given in figure 3.21.

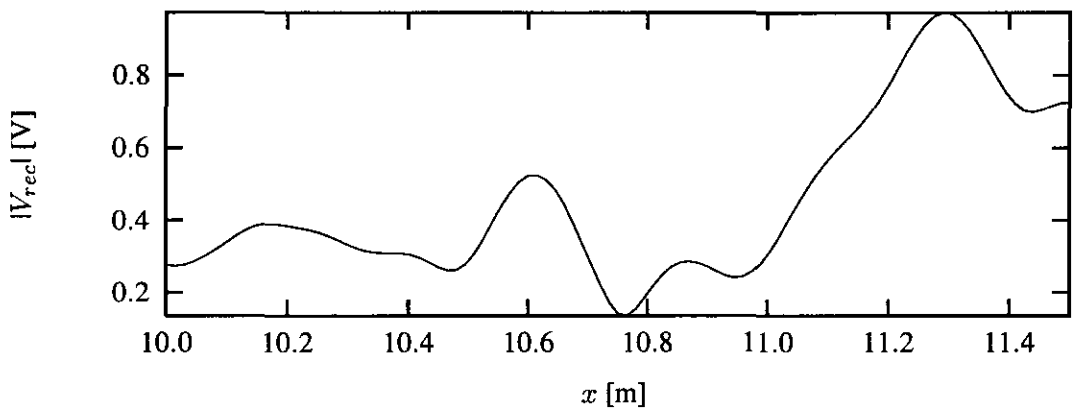

Figure 3.21: *Received voltage*

The received voltage will be used to calculate the signal-to-noise ratio along the observation line. The signal power is given by $|v_{rec}|^2/(8Re(z))$. The impedance z of the receiving half-wave dipole antenna is 73 Ohm. The noise bandwidth will be taken equal to the channel spacing, which is 1.7 MHz for DECT systems. The noise temperature is 300 K. Thus, the noise power is -141.5 dBW. The signal-to-noise ratio will be calculated using the signal power and the noise power. The signal-to-noise ratio along the observation line is presented in figure 3.22.

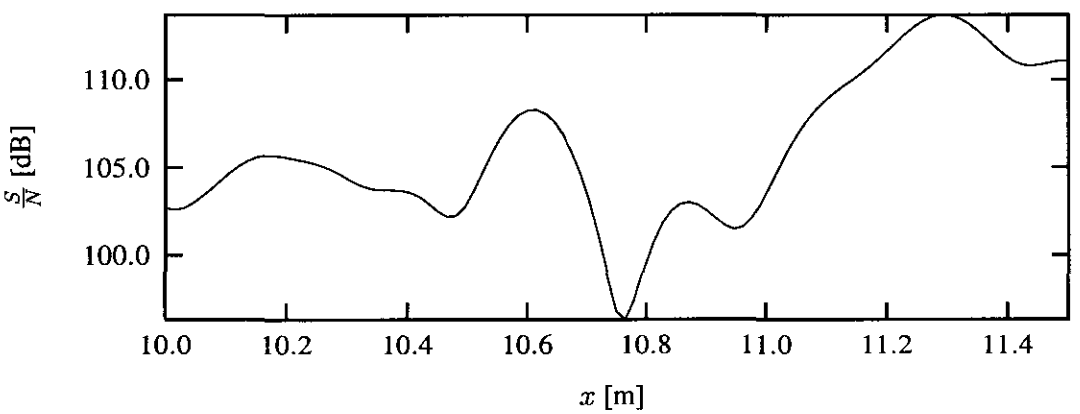

Figure 3.22: *Signal-to-noise ratio*

The signal-to-noise ratio is very high, this means that the bit error rate will be very low inside the room. However, very high bit error rates are reported in [Lawton 93]. In this paper, the predicted signal-to-noise ratio is larger than 45 dB when source and receiver are 10 meters apart. Such a large signal-to-noise ratio would also result in a high-quality telecommunication link. This means that the high error rates in [Lawton 93] must be caused by another fading phenomenon, for example frequency selective fading (delay spread).

Up to now, we have only taken into account the relationship between signal-to-noise ratio and bit error rate. Using wide-band pulse transmission, a series of delayed and attenuated pulses (echoes) will be received inside a room. These unwanted echoes, which will cause intersymbol interference, can be characterised by the RMS delay spread. It can be expected that the delay spread in a perfectly conducting room will be very high. Time-domain electromagnetic fields are needed for evaluating the RMS delay spread inside a room. The time-domain electromagnetic fields generated by a Gaussian current source will be investigated in a future report.

Chapter 4

Conclusions

This report describes the variations of electric fields, received voltages, signal-to-noise ratios and bit error rates in an indoor environment. The signal received by a mobile system can be very weak at some points in the room, caused by destructive interference of the electromagnetic fields. A model has been developed to obtain insight in the fundamental processes of wave propagation in a room.

The Green's function technique has been used for modelling the electromagnetic fields in a room with two dielectric walls. With this model, the effect of absorption and scattering of electromagnetic waves at a dielectric wall can be examined. The Green's functions are described by double series. An estimate is given for the accuracy of the electromagnetic fields. Furthermore, it has been found that the truncation error of the series is independent of one dimension of the room. This means that wave propagation in a large room can be described very efficiently with the presented Green's function. The electromagnetic fields are calculated for point sources and half-wave dipole transmitters. The electromagnetic fields generated by a half-wave dipole antenna are obtained by performing an integration analytically, which reduces the computation time.

The interaction between the electromagnetic fields and the mobile receiver is modelled by a Thévenin representation. The received voltage of a half-wave dipole antenna can be calculated analytically. The induced voltage on the receiver is not only a function of the electromagnetic field but also depends on the current distribution of the receiving antenna. The received voltage changes rapidly inside the room.

Diversity receivers can be used for reducing the rapid signal variations in the mobile transmission path. Four diversity receivers have been investigated for improving the average signal level inside the room. The four diversity techniques (categorized by increasing gains compared to a single antenna) are: switch diversity, selection diversity, equal gain combining and maximal ratio combining. It has been shown that space diversity can be used to reduce the sizes of the regions with low values of the electromagnetic field components.

Finally, the signal-to-noise ratio along an observation line inside the room has been presented. It can be concluded that the quality of the received signal depends greatly on the location of the receiver.

Appendix A

Electromagnetic fields inside a room

Electric field in the x-direction due to a point-source in the x-direction.

Interval 1: $0 \leq x \leq d_1$

$$G_{E1xx} = -\frac{4\mu_1}{bck_1^2} \sum_{m=1}^{\infty} \sum_{n=1}^{\infty} \left[k_1^2 - k_{1x}^2\right] \sin(k_{ym}y) \sin(k_{ym}y_s) \sin(k_{zn}z) \sin(k_{zn}z_s) \cdot \frac{\cos(k_{1x}x)\left[Z_{2mn} \sin(k_{2x}(x_s - d_2)) + k_{2x} \cos(k_{2x}(x_s - d_2))\right]}{D_{mn} \cos(k_{1x}d_1)} \tag{A.1}$$

Interval 2: $d_1 < x \leq x_s$

$$G_{E2xx}^1 = -\frac{4\mu_2}{bck_2^2} \sum_{m=1}^{\infty} \sum_{n=1}^{\infty} \left\{ \left[k_2^2 - k_{2x}^2\right] \sin(k_{ym}y) \sin(k_{ym}y_s) \sin(k_{zn}z) \sin(k_{zn}z_s) \frac{1}{k_{2x}D_{mn}} \cdot \cos(k_{2x}(x_s - d_2)) \left[k_{2x}Z_{1mn} \sin(k_{2x}(x - d_1)) + k_{2x}^2 \cos(k_{2x}(x - d_1))\right] + \sin(k_{2x}(x_s - d_2)) \left[Z_{1mn}Z_{2mn} \sin(k_{2x}(x - d_1)) + k_{2x}Z_{2mn} \cos(k_{2x}(x - d_1))\right] \right\} - \frac{\mu_2}{k_2^2}\delta(\vec{r} - \vec{r}_s) \tag{A.2}$$

Interval 3: $x_s < x \leq d_2$

$$G_{E2xx}^2 = -\frac{4\mu_2}{bck_2^2} \sum_{m=1}^{\infty} \sum_{n=1}^{\infty} \left[k_2^2 - k_{2x}^2\right] \sin(k_{ym}y) \sin(k_{ym}y_s) \sin(k_{zn}z) \sin(k_{zn}z_s) \frac{1}{k_{2x}D_{mn}} \cdot \cos(k_{2x}(x - d_2)) \left[k_{2x}Z_{1mn} \sin(k_{2x}(x_s - d_1)) + k_{2x}^2 \cos(k_{2x}(x_s - d_1))\right] + \sin(k_{2x}(x - d_2)) \left[Z_{1mn}Z_{2mn} \sin(k_{2x}(x_s - d_1)) + k_{2x}Z_{2mn} \cos(k_{2x}(x_s - d_1))\right] \tag{A.3}$$

Interval 4: $d_2 < x \leq a$

$$G_{E3xx} = -\frac{4\mu_3}{bck_3^2}\sum_{m=1}^{\infty}\sum_{n=1}^{\infty}\left[k_3^2 - k_{3x}^2\right]\sin(k_{ym}y)\sin(k_{ym}y_s)\sin(k_{zn}z)\sin(k_{zn}z_s)\cdot \frac{\cos(k_{3x}(x-a))\left[Z_{1mn}\sin(k_{2x}(x_s-d_1)) + k_{2x}\cos(k_{2x}(x_s-d_1))\right]}{D_{mn}\cos(k_{1x}(d_2-a))} \tag{A.4}$$

with

$$\begin{aligned} k_{1x} &= \sqrt{k_1^2 - \left(\tfrac{m\pi}{b}\right)^2 - \left(\tfrac{n\pi}{c}\right)^2} \\ k_{2x} &= \sqrt{k_2^2 - \left(\tfrac{m\pi}{b}\right)^2 - \left(\tfrac{n\pi}{c}\right)^2} \\ k_{3x} &= \sqrt{k_3^2 - \left(\tfrac{m\pi}{b}\right)^2 - \left(\tfrac{n\pi}{c}\right)^2} \\ Z_{1mn} &= -\tfrac{\varepsilon_2 k_{1x}}{\varepsilon_1}\tan(k_{1x}d_1) \\ Z_{2mn} &= -\tfrac{\varepsilon_2 k_{3x}}{\varepsilon_3}\tan(k_{3x}(d_2-a)) \\ D_{mn} &= \sin(k_{2x}(d_2-d_1))(-k_{2x}^2 - Z_{1mn}Z_{2mn}) + \cos(k_{2x}(d_2-d_1))(k_{2x}Z_{1mn} - k_{2x}Z_{2mn}) \end{aligned} \tag{A.5}$$

Electric field in the x direction due to a point source in the z direction

Interval 1: $0 \leq x \leq d_1$

$$G_{E1xz} = \frac{4\mu_1}{bck_1^2}\sum_{m=1}^{\infty}\sum_{n=1}^{\infty}\frac{n\pi}{c}\sin(k_{ym}y)\sin(k_{ym}y_s)\sin(k_{zn}z)\cos(k_{zn}z_s)\cdot \frac{k_{1x}Y_{1mn}\cos(k_{1x}x)\left[\sin(k_{2x}(x_s-d_2)) + k_{2x}Y_{2mn}\cos(k_{2x}(x_s-d_2))\right]}{J_{mn}\sin(k_{1x}d_1)} + \frac{\left[k_1^2 - k_{1x}^2\right]\cos(k_{1x}x)\mu_1}{K_{mn}}\Big\{\left[k_2^2 - k_1^2\right]M_{mn} \tag{A.6}$$

$$\left[k_{2x}k_3^2\mu_2\cos(k_{3x}(d_2-a))\cos(k_{2x}(d_1-d_2)) - k_{3x}k_2^2\mu_3\sin(k_{3x}(d_2-a))\sin(k_{2x}(d_1-d_2))\right] +$$

$$\left[k_3^2 - k_2^2\right]\mu_2 L_{mn}\cos(k_{3x}(d_2-a))k_{2x}k_1^2\mu_2\Big\}$$

Interval 2: $d_1 < x \leq x_s$

$$G^1_{E2xz} = \frac{4\mu_2}{bck_2^2} \sum_{m=1}^{\infty} \sum_{n=1}^{\infty} \frac{n\pi}{c} \sin(k_{ym}y) \sin(k_{ym}y_s) \sin(k_{zn}z) \cos(k_{zn}z_s) \cdot$$
$$\frac{[k_{2x}Y_{2mn} \cos(k_{2x}(x_s - d_2)) + \sin(k_{2x}(x_s - d_2))] \, [\cos(k_{2x}(x - d_1)) - k_{2x}Y_{1mn} \sin(k_{2x}(x - d_1))]}{J_{mn}} +$$
$$\frac{[k_2^2 - k_{2x}^2]}{K_{mn}} \left\{ \left[k_2^2 - k_1^2\right] M_{mn} \cos(k_{1x}d_1) \right. \tag{A.7}$$
$$[k_{2x}k_3^2\mu_2 \cos(k_{3x}(d_2 - a)) \cos(k_{2x}(x - d_2)) - k_{3x}k_2^2\mu_3 \sin(k_{3x}(d_2 - a)) \sin(k_{2x}(x - d_2))] +$$
$$\left[k_3^2 - k_2^2\right] \mu_2 L_{mn} \cos(k_{3x}(d_2 - a)) \left[k_{1x}k_2^2\mu_1 \sin(k_{1x}d_1) \sin(k_{2x}(d_1 - x)) + \right.$$
$$\left. k_{2x}k_1^2\mu_2 \cos(k_{1x}d_1) \cos(k_{2x}(d_1 - x))\right]$$

Interval 3: $x_s < x \leq d_2$

$$G^2_{E2xz} = \frac{4\mu_2}{bck_2^2} \sum_{m=1}^{\infty} \sum_{n=1}^{\infty} \frac{n\pi}{c} \sin(k_{ym}y) \sin(k_{ym}y_s) \sin(k_{zn}z) \cos(k_{zn}z_s) \cdot$$
$$\frac{[k_{2x}Y_{1mn} \cos(k_{2x}(x_s - d_1)) + \sin(k_{2x}(x_s - d_1))] \, [\cos(k_{2x}(x - d_2)) - k_{2x}Y_{2mn} \sin(k_{2x}(x - d_2))]}{J_{mn}} +$$
$$\frac{[k_2^2 - k_{2x}^2]}{K_{mn}} \left\{ \left[k_2^2 - k_1^2\right] M_{mn} \cos(k_{1x}d_1) \right. \tag{A.8}$$
$$[k_{2x}k_3^2\mu_2 \cos(k_{3x}(d_2 - a)) \cos(k_{2x}(x - d_2)) - k_{3x}k_2^2\mu_3 \sin(k_{3x}(d_2 - a)) \sin(k_{2x}(x - d_2))] +$$
$$\left[k_3^2 - k_2^2\right] \mu_2 L_{mn} \cos(k_{3x}(d_2 - a)) \left[k_{1x}k_2^2\mu_1 \sin(k_{1x}d_1) \sin(k_{2x}(d_1 - x)) + \right.$$
$$\left. k_{2x}k_1^2\mu_2 \cos(k_{1x}d_1) \cos(k_{2x}(d_1 - x))\right]$$

Interval 4: $d_2 < x \leq a$

$$G_{E3xz} = \frac{4\mu_3}{bck_3^2} \sum_{m=1}^{\infty} \sum_{n=1}^{\infty} \frac{n\pi}{c} \sin(k_{ym}y) \sin(k_{ym}y_s) \sin(k_{zn}z) \cos(k_{zn}z_s) \cdot$$
$$\frac{[k_{2x}Y_{1mn} \cos(k_{2x}(x_s - d_1)) + \sin(k_{2x}(x_s - d_1))] \, k_{3x}Y_{2mn} \cos(k_{3x}(x - a))}{J_{mn} \sin(k_{3x}(d_2 - a))} +$$
$$\frac{[k_3^2 - k_{3x}^2] \cos(k_{3x}(x - a))}{K_{mn}} \left[k_2^2 - k_1^2\right] M_{mn} \cos(k_{1x}d_1) k_{2x}k_3^2\mu_2 + \tag{A.9}$$
$$\left[k_3^2 - k_2^2\right] \mu_2 L_{mn} \left[k_{1x}k_2^2\mu_1 \sin(k_{1x}d_1) \sin(k_{2x}(d_1 - x)) + k_{2x}k_1^2\mu_2 \cos(k_{1x}d_1) \cos(k_{2x}(d_1 - d_2))\right]$$

with

$$
\begin{aligned}
k_{1x} &= \sqrt{k_1^2 - \left(\tfrac{m\pi}{b}\right)^2 - \left(\tfrac{n\pi}{c}\right)^2} \\
k_{2x} &= \sqrt{k_2^2 - \left(\tfrac{m\pi}{b}\right)^2 - \left(\tfrac{n\pi}{c}\right)^2} \\
k_{3x} &= \sqrt{k_3^2 - \left(\tfrac{m\pi}{b}\right)^2 - \left(\tfrac{n\pi}{c}\right)^2} \\
Y_{1mn} &= \frac{\mu_1}{\mu_2 k_{1x}} \tan(k_{1x} d_1) \\
Y_{2mn} &= \frac{\mu_3}{\mu_2 k_{3x}} \tan(k_{3x}(d_2 - a))
\end{aligned}
\tag{A.10}
$$

$$J_{mn} = \cos(k_{2x}(d_2 - d_1))(k_{2x} Y_{2mn} - k_{2x} Y_{1mn}) - \sin(k_{2x}(d_2 - d_1))(1 + k_{2x}^2 Y_{1mn} Y_{2mn})$$

$$M_{mn} = Y_{1mn}[\sin(k_{2x}(x_s - d_2)) + k_{2x} Y_{2mn} \cos(k_{2x}(x_s - d_2))]/J_{mn}$$

$$L_{mn} = Y_{2mn}[\sin(k_{2x}(x_s - d_1)) + k_{2x} Y_{1mn} \cos(k_{2x}(x_s - d_1))]/J_{mn}$$

$$
\begin{aligned}
K_{mn} &= k_{3x} k_2^2 \mu_3 \sin(k_{3x}(a - d_2)) \cdot \\
&[k_{2x} k_1^2 \mu_2 \cos(k_{1x} d_1) \cos(k_{2x}(d_2 - d_1)) - k_{1x} k_2^2 \mu_1 \sin(k_{1x} d_1) \sin(k_{2x}(d_2 - d_1))] \\
&+ k_{2x} k_3^2 \mu_2 \cos(k_{3x}(a - d_2)) \cdot \\
&[k_{2x} k_1^2 \mu_2 \cos(k_{1x} d_1) \sin(k_{2x}(d_2 - d_1)) + k_{1x} k_2^2 \mu_1 \sin(k_{1x} d_1) \cos(k_{2x}(d_2 - d_1))]
\end{aligned}
\tag{A.11}
$$

Magnetic field in the z-direction due to a point-source in the x-direction.

Interval 1: $0 \leq x \leq d_1$

$$
\begin{aligned}
G_{H1zx} = &\frac{4}{bc} \sum_{m=1}^{\infty} \sum_{n=1}^{\infty} \frac{m\pi}{b} \cos(k_{ym} y) \sin(k_{ym} y_s) \sin(k_{zn} z) \sin(k_{zn} z_s) \cdot \\
&\frac{\cos(k_{1x} x)\,[Z_{2mn} \sin(k_{2x}(x_s - d_2)) + k_{2x} \cos(k_{2x}(x_s - d_2))]}{D_{mn} \cos(k_{1x} d_1)}
\end{aligned}
\tag{A.12}
$$

Interval 2: $d_1 < x \leq x_s$

$$
\begin{aligned}
G^1_{H2zx} = &\frac{4}{bc} \sum_{m=1}^{\infty} \sum_{n=1}^{\infty} \frac{m\pi}{b} \cos(k_{ym} y) \sin(k_{ym} y_s) \sin(k_{zn} z) \sin(k_{zn} z_s) \frac{1}{k_{2x} D_{mn}} \cdot \\
&\cos(k_{2x}(x_s - d_2)) \left[k_{2x} Z_{1mn} \sin(k_{2x}(x - d_1)) + k_{2x}^2 \cos(k_{2x}(x - d_1))\right] + \\
&\sin(k_{2x}(x_s - d_2))\,[k_{2x} Z_{2mn} \cos(k_{2x}(x - d_1)) + Z_{1mn} Z_{2mn} \sin(k_{2x}(x - d_1))]
\end{aligned}
\tag{A.13}
$$

Interval 3: $x_s < x \leq d_2$

$$G^2_{H2zx} = \frac{4}{bc}\sum_{m=1}^{\infty}\sum_{n=1}^{\infty}\frac{m\pi}{b}\cos(k_{ym}y)\sin(k_{ym}y_s)\sin(k_{zn}z)\sin(k_{zn}z_s)\frac{1}{k_{2x}D_{mn}}\cdot$$
$$\cos(k_{2x}(x-d_2))\left[k_{2x}Z_{1mn}\sin(k_{2x}(x_s-d_1)) + k_{2x}^2\cos(k_{2x}(x_s-d_1))\right] + \tag{A.14}$$
$$\sin(k_{2x}(x-d_2))\left[k_{2x}Z_{2mn}\cos(k_{2x}(x_s-d_1)) + Z_{1mn}Z_{2mn}\sin(k_{2x}(x_s-d_1))\right]$$

Interval 4: $d_2 < x \leq a$

$$G_{H3zx} = \frac{4}{bc}\sum_{m=1}^{\infty}\sum_{n=1}^{\infty}\frac{m\pi}{b}\cos(k_{ym}y)\sin(k_{ym}y_s)\sin(k_{zn}z)\sin(k_{zn}z_s)\frac{1}{D_{mn}\cos(k_{3x}(d_2-a))}\cdot \tag{A.15}$$
$$\cos(k_{3x}(x-a))\left[Z_{1mn}\sin(k_{2x}(x_s-d_1)) + k_{2x}\cos(k_{2x}(x_s-d_1))\right]$$

with

$$\begin{aligned}
k_{1x} &= \sqrt{k_1^2 - \left(\tfrac{m\pi}{b}\right)^2 - \left(\tfrac{n\pi}{c}\right)^2}\\
k_{2x} &= \sqrt{k_2^2 - \left(\tfrac{m\pi}{b}\right)^2 - \left(\tfrac{n\pi}{c}\right)^2}\\
k_{3x} &= \sqrt{k_3^2 - \left(\tfrac{m\pi}{b}\right)^2 - \left(\tfrac{n\pi}{c}\right)^2}\\
Z_{1mn} &= -\tfrac{\varepsilon_2 k_{1x}}{\varepsilon_1}\tan(k_{1x}d_1)\\
Z_{2mn} &= -\tfrac{\varepsilon_2 k_{3x}}{\varepsilon_3}\tan(k_{3x}(d_2-a))\\
D_{mn} &= \sin(k_{2x}(d_2-d_1))(-k_{2x}^2 - Z_{1mn}Z_{2mn}) + \cos(k_{2x}(d_2-d_1))(k_{2x}Z_{1mn} - k_{2x}Z_{2mn})
\end{aligned} \tag{A.16}$$

Magnetic field in the y-direction due to a point-source in the z-direction.

Interval 1: $0 \leq x \leq d_1$

$$G_{H1yz} = \frac{2\mu_1}{bc\mu_3} \sum_{m=1}^{\infty} \sum_{n=1}^{\infty} \epsilon_{0n} \sin(k_{ym}y) \sin(k_{ym}y_s) \cos(k_{zn}z) \cos(k_{zn}z_s) \cdot$$
$$\frac{k_{1x}Y_{1mn} \cos(k_{1x}x) \left[\sin(k_{2x}(x_s - d_2)) + k_{2x}Y_{2mn} \cos(k_{2x}(x_s - d_2))\right]}{J_{mn} \sin(k_{1x}d_1)} +$$
$$\left(\frac{n\pi}{c}\right)^2 \cos(k_{1x}x) \frac{\mu_1}{\mu_2} \frac{1}{K_{mn}} \cdot \qquad \text{(A.17)}$$
$$\left[k_2^2 - k_1^2\right] M_{mn} \left[k_{2x}k_3^2\mu_2 \cos(k_{3x}(d_2 - a)) \cos(k_{2x}(d_1 - d_2))\right.$$
$$-k_{3x}k_2^2\mu_3 \sin(k_{3x}(d_2 - a)) \sin(k_{2x}(d_1 - d_2))] +$$
$$\left.\left[k_3^2 - k_2^2\right] \mu_2 L_{mn} \cos(k_{3x}(d_2 - a))k_{2x}k_1^2\mu_2\right\}$$

Interval 2: $d_1 < x \leq x_s$

$$G^1_{H2yz} = \frac{2\mu_2}{bc\mu_3} \sum_{m=1}^{\infty} \sum_{n=1}^{\infty} \epsilon_{0n} \sin(k_{ym}y) \sin(k_{ym}y_s) \cos(k_{zn}z) \cos(k_{zn}z_s) \cdot$$
$$\left[\sin(k_{2x}(x_s - d_2)) + k_{2x}Y_{2mn} \cos(k_{2x}(x_s - d_2))\right] \cdot$$
$$\frac{\left[\cos(k_{2x}(x - d_1)) - k_{2x}Y_{1mn} \sin(k_{2x}(x - d_1))\right]}{J_{mn}} +$$
$$\left(\frac{n\pi}{c}\right)^2 \frac{1}{K_{mn}} \cdot \qquad \text{(A.18)}$$
$$\left[k_2^2 - k_1^2\right] M_{mn} \cos(k_{1x}d_1) \left[k_{2x}k_3^2\mu_2 \cos(k_{3x}(d_2 - a)) \cos(k_{2x}(x - d_2))\right.$$
$$-k_{3x}k_2^2\mu_3 \sin(k_{3x}(d_2 - a)) \sin(k_{2x}(x - d_2))] +$$
$$\left[k_3^2 - k_2^2\right] \mu_2 L_{mn} \cos(k_{3x}(d_2 - a)) \left[k_{1x}k_2^2\mu_2 \sin(k_{1x}d_1) \sin(k_{2x}(d_1 - x)) + \right.$$
$$\left.k_{2x}k_1^2\mu_2 \cos(k_{1x}d_1) \cos(k_{2x}(d_1 - x))\right]$$

Interval 3: $x_s < x \leq d_2$

$$G^2_{H2yz} = \frac{2}{bc}\sum_{m=1}^{\infty}\sum_{n=1}^{\infty}\epsilon_{0n}\sin(k_{ym}y)\sin(k_{ym}y_s)\cos(k_{zn}z)\cos(k_{zn}z_s)\cdot$$
$$\frac{[\sin(k_{2x}(x_s-d_1))+k_{2x}Y_{1mn}\cos(k_{2x}(x_s-d_1))]\,[\cos(k_{2x}(x-d_2))-k_{2x}Y_{2mn}\sin(k_{2x}(x-d_2))]}{J_{mn}}+$$
$$\left(\frac{n\pi}{c}\right)^2\frac{1}{K_{mn}}\cdot$$
$$[k_2^2-k_1^2]\,M_{mn}\cos(k_{1x}d_1)\,[k_{2x}k_3^2\mu_2\cos(k_{3x}(d_2-a))\cos(k_{2x}(x-d_2)) \tag{A.19}$$
$$-k_{3x}k_2^2\mu_3\sin(k_{3x}(d_2-a))\sin(k_{2x}(x-d_2))]+$$
$$\left[k_3^2-k_2^2\right]\mu_2 L_{mn}\cos(k_{3x}(d_2-a))\left[k_{1x}k_2^2\mu_2\sin(k_{1x}d_1)\sin(k_{2x}(d_1-x))+\right.$$
$$\left.k_{2x}k_1^2\mu_2\cos(k_{1x}d_1)\cos(k_{2x}(d_1-x))\right]$$

Interval 4: $d_2 < x \leq a$

$$G_{H3yz} = \frac{2}{bc}\sum_{m=1}^{\infty}\sum_{n=1}^{\infty}\epsilon_{0n}\sin(k_{ym}y)\sin(k_{ym}y_s)\cos(k_{zn}z)\cos(k_{zn}z_s)\cdot$$
$$\frac{k_{3x}Y_{2mn}\cos(k_{3x}(x-a))\,[\sin(k_{2x}(x_s-d_1))+k_{2x}Y_{1mn}\cos(k_{2x}(x_s-d_1))]}{J_{mn}\sin(k_{3x}(d_2-a))}+$$
$$\frac{\mu_3}{\mu_2}\left(\frac{n\pi}{c}\right)^2\frac{\cos(k_{3x}(x-a))}{K_{mn}}\cdot \tag{A.20}$$
$$[k_2^2-k_1^2]\,M_{mn}k_{2x}k_3^2\mu_2\cos(k_{1x}d_1)+$$
$$\left[k_3^2-k_2^2\right]\mu_2 L_{mn}\left[k_{1x}k_2^2\mu_1\sin(k_{1x}d_1)\sin(k_{2x}(d_1-d_2))+k_{2x}k_1^2\mu_2\cos(k_{1x}d_1)\cos(k_{2x}(d_1-d_2))\right]$$

with

$$
\begin{aligned}
k_{1x} &= \sqrt{k_1^2 - \left(\tfrac{m\pi}{b}\right)^2 - \left(\tfrac{n\pi}{c}\right)^2} \\
k_{2x} &= \sqrt{k_2^2 - \left(\tfrac{m\pi}{b}\right)^2 - \left(\tfrac{n\pi}{c}\right)^2} \\
k_{3x} &= \sqrt{k_3^2 - \left(\tfrac{m\pi}{b}\right)^2 - \left(\tfrac{n\pi}{c}\right)^2} \\
Y_{1mn} &= \frac{\mu_1}{\mu_2 k_{1x}} \tan(k_{1x} d_1) \\
Y_{2mn} &= \frac{\mu_3}{\mu_2 k_{3x}} \tan(k_{3x}(d_2 - a))
\end{aligned}
\tag{A.21}
$$

$$
J_{mn} = \cos(k_{2x}(d_2 - d_1))(k_{2x} Y_{2mn} - k_{2x} Y_{1mn}) - \sin(k_{2x}(d_2 - d_1))(1 + k_{2x}^2 Y_{1mn} Y_{2mn})
$$

$$
M_{mn} = Y_{1mn}[\sin(k_{2x}(x_s - d_2)) + k_{2x} Y_{2mn} \cos(k_{2x}(x_s - d_2))]/J_{mn}
$$

$$
L_{mn} = Y_{2mn}[\sin(k_{2x}(x_s - d_1)) + k_{2x} Y_{1mn} \cos(k_{2x}(x_s - d_1))]/J_{mn}
$$

$$
\begin{aligned}
K_{mn} &= k_{3x} k_2^2 \mu_3 \sin(k_{3x}(a - d_2)) \cdot \\
&[k_{2x} k_1^2 \mu_2 \cos(k_{1x} d_1) \cos(k_{2x}(d_2 - d_1)) - k_{1x} k_2^2 \mu_1 \sin(k_{1x} d_1) \sin(k_{2x}(d_2 - d_1))] \\
&+ k_{2x} k_3^2 \mu_2 \cos(k_{3x}(a - d_2)) \cdot \\
&[k_{2x} k_1^2 \mu_2 \cos(k_{1x} d_1) \sin(k_{2x}(d_2 - d_1)) + k_{1x} k_2^2 \mu_1 \sin(k_{1x} d_1) \cos(k_{2x}(d_2 - d_1))]
\end{aligned}
\tag{A.22}
$$

References

[Dolmans 95] Dolmans, G.
ELECTROMAGNETIC FIELDS INSIDE A LARGE ROOM WITH PERFECTLY CONDUCTING WALLS.
Eindhoven: Eindhoven University of Technology, Faculty of Electrical Engineering, 1995.
EUT Report 95-E-286.

[Leyten/Dolmans 95] Dolmans, G. and L. Leyten
APPLICATION OF GREEN'S FUNCTION TECHNIQUE TO MODEL THE RECEIVED VOLTAGE OF AN ANTENNA IN A MULTI-PATH ENVIRONMENT.
In: Proc. ICAP'95, Eindhoven, The Netherlands, 4-7 April 1995.
London: IEE, 1995. P. 186-189.

[Harrington 61] Harrington, R.F.
TIME-HARMONIC ELECTROMAGNETIC FIELDS.
New York: McGraw-Hill, 1961.

[Kant 94] Kant, G.W.
DE VELDVERDELING TEN GEVOLGE VAN EEN ANTENNE GEPLAATST IN EEN CAVITY MET EEN BEKLEDE WAND (in Dutch).
Department of Electromagnetics, Faculty of Electrical Engineering, Eindhoven University of Technology, 1994.
Graduation Report EM-13-94.

[Morse 53] Morse, P.M. and H. Feshbach
METHODS OF THEORETICAL PHYSICS, PART II.
New York: McGraw-Hill, 1953.

[Signalen 1] SYLLABUS BIJ HET COLLEGE SIGNALEN 1 (in Dutch).
Faculty of Mathematics and Computing Science, Eindhoven University of Technology, 1988.
Lecture notes, no. 2372. P. 38-43.

[Sommerfeld 64] Sommerfeld, A.
PARTIAL DIFFERENTIAL EQUATIONS IN PHYSICS.
New York: Academic Press, 1964.

[Leersum 95] Leersum van, B.J.A.M.
ANALYSIS OF THE INTERACTION BETWEEN A DIPOLE ANTENNA AND A LARGE OBJECT USING THE METHOD OF MOMENTS AND THE FINITE DIFFERENCE TIME DOMAIN TECHNIQUE.
Philips Research Laboratories, Eindhoven, The Netherlands, May 1995.
Technical report UR 012/95.

[Shanmugam 85] Shanmugam, K.S.
DIGITAL AND ANALOG COMMUNICATION SYSTEMS.
New York: John Wiley & Sons, 1985.

[Bot 93] Bot, P.G.M. de
ANTENNA DIVERSITY FOR OFDM SYSTEMS.
In: Proceedings of the 14th Symposium on Information Theory in the Benelux, Veldhoven, The Netherlands, 17 and 18 May 1993.
Ed. by K.A. Schouhamer Immink and P.G.M. de Bot.
Enschede: Werkgemeenschap voor Inf.- en Com. theorie, 1993. P. 1-17.

[Lee 82] Lee, W.C.Y.
MOBILE COMMUNICATIONS ENGINEERING.
New York: McGraw-Hill, 1982.

[White 94] White, G.
MOBILE RADIO TECHNOLOGY.
Oxford: Butterworth-Heinemann, 1994.

[Jakes 93] Jakes, W.C.
MICROWAVE MOBILE COMMUNICATIONS.
New York: IEEE Press, 1993.

[Freeman 87] Freeman, R.L.
RADIO SYSTEM DESIGN FOR TELECOMMUNICATIONS (1-100 GHZ).
New York: John Wiley & Sons, 1987.

[Wittneben 94] Wittneben, A. and T. Kaltenschnee
TX SELECTION DIVERSITY WITH PREDICTION: SYSTEMATIC NONADAPTIVE PREDICTOR DESIGN.
In: Proc. IEEE Vehic. Techn. Conference, Stockholm, Sweden, 8-10 June, 1994.
Piscataway: IEEE, 1994. Vol. 2, P. 1246-1250.

[Jeuken 88] Jeuken, M.E.J.
ELEKTROMAGNETISCHE ANTENNAS 1, GRONDSLAGEN (in Dutch).
Department of Electromagnetics, Faculty of Electrical Engineering, Eindhoven University of Technology, 1988.
Lecture notes.

[Moriyama 92] Moriyama, E. et al.
2.6 GHZ MULTIPATH CHARACTERISTICS MEASUREMENT IN A SHIELDED BUILDING.
In: Proc. IEEE Vehic. Techn. Conference, Denver, Colorado, 10-13 May, 1992.
Piscataway: IEEE, 1992. Vol. 2, P. 621-624.

[Lawton 93] Lawton, M.C. and A.R. Nix, J.P. McGeehan
A PERFORMANCE EVALUATION OF SECTORISED ANTENNAS FOR INDOOR RADIO LANS.
In: Proc. ICAP'93, Edinburgh, UK, 30 March - 2 April 1993.
London: IEE, 1993. P. 150-154.

[Feher 95] Feher, K.
WIRELESS DIGITAL COMMUNICATIONS:
Modulation & Spread Spectrum Applications.
New Jersey: Prentice-Hall, 1995.

Eindhoven University of Technology Research Reports ISSN 0167-9708
Coden: TEUEDE

Faculty of Electrical Engineering

(271) Bloks, R.H.J.
CODE GENERATION FOR THE ATTRIBUTE EVALUATOR OF THE PROTOCOL ENGINE GRAMMAR PROCESSOR UNIT.
EUT Report 93-E-271. 1993. ISBN 90-6144-271-0

(272) Yan, Keping and E.M. van Veldhuizen
FLUE GAS CLEANING BY PULSE CORONA STREAMER.
EUT Report 93-E-272. 1993. ISBN 90-6144-272-9

(273) Smolders, A.B.
FINITE STACKED MICROSTRIP ARRAYS WITH THICK SUBSTRATES.
EUT Report 93-E-273. 1993. ISBN 90-6144-273-7

(274) Bollen, M.H.J. and M.A. van Houten
ON INSULAR POWER SYSTEMS: Drawing up an inventory of phenomena and research possibilities.
EUT Report 93-E-274. 1993. ISBN 90-6144-274-5

(275) Deursen, A.P.J. van
ELECTROMAGNETIC COMPATIBILITY: Part 5, installation and mitigation guidelines, section 3, cabling and wiring.
EUT Report 93-E-275. 1993. ISBN 90-6144-275-3

(276) Bollen, M.H.J.
LITERATURE SEARCH FOR RELIABILITY DATA OF COMPONENTS IN ELECTRIC DISTRIBUTION NETWORKS.
EUT Report 93-E-276. 1993. ISBN 90-6144-276-1

(277) Weiland, Siep
A BEHAVIORAL APPROACH TO BALANCED REPRESENTATIONS OF DYNAMICAL SYSTEMS.
EUT Report 93-E-277. 1993. ISBN 90-6144-277-X

(278) Gorshkov, Yu.A. and V.I. Vladimirov
LINE REVERSAL GAS FLOW TEMPERATURE MEASUREMENTS: Evaluations of the optical arrangements for the instrument.
EUT Report 93-E-278. 1993. ISBN 90-6144-278-8

(279) Creyghton, Y.L.M. and W.R. Rutgers, E.M. van Veldhuizen
IN-SITU INVESTIGATION OF PULSED CORONA DISCHARGE.
EUT Report 93-E-279. 1993. ISBN 90-6144-279-6

(280) Li, H.Q. and R.P.P. Smeets
GAP-LENGTH DEPENDENT PHENOMENA OF HIGH-FREQUENCY VACUUM ARCS.
EUT Report 93-E-280. 1993. ISBN 90-6144-280-X

(281) Di, Chennian and Jochen A.G. Jess
ON THE DEVELOPMENT OF A FAST AND ACCURATE BRIDGING FAULT SIMULATOR.
EUT Report 94-E-281. 1994. ISBN 90-6144-281-8

(282) Falkus, H.M. and A.A.H. Damen
MULTIVARIABLE H-INFINITY CONTROL DESIGN TOOLBOX: User manual.
EUT Report 94-E-282. 1994. ISBN 90-6144-282-6

(283) Meng, X.Z. and J.G.J. Sloot
THERMAL BUCKLING BEHAVIOUR OF FUSE WIRES.
EUT Report 94-E-283. 1994. ISBN 90-6144-283-4

(284) Rangelrooij, A. van and J.P.M. Voeten
CCSTOOL2: An expansion, minimization, and verification tool for finite state CCS descriptions.
EUT Report 94-E-284. 1994. ISBN 90-6144-284-2

Eindhoven University of Technology Research Reports ISSN 0167-9708
Coden: TEUEDE

Faculty of Electrical Engineering

(285) Roer, Th.G. van de
MODELING OF DOUBLE BARRIER RESONANT TUNNELING DIODES: D.C. and noise model.
EUT Report 95-E-285. 1995. ISBN 90-6144-285-0

(286) Dolmans, G.
ELECTROMAGNETIC FIELDS INSIDE A LARGE ROOM WITH PERFECTLY CONDUCTING WALLS.
EUT Report 95-E-286. 1995. ISBN 90-6144-286-9

(287) Liao, Boshu and P. Massee
RELIABILITY ANALYSIS OF AUXILIARY ELECTRICAL SYSTEMS AND GENERATING UNITS.
EUT Report 95-E-287. 1995. ISBN 90-6144-287-7

(288) Weiland, Siep and Anton A. Stoorvogel
OPTIMAL HANKEL NORM IDENTIFICATION OF DYNAMICAL SYSTEMS.
EUT Report 95-E-288. 1995. ISBN 90-6144-288-5

(289) Konieczny, Pawel A. and Lech Józwiak
MINIMAL INPUT SUPPORT PROBLEM AND ALGORITHMS TO SOLVE IT.
EUT Report 95-E-289. 1995. ISBN 90-6144-289-3

(290) Voeten, J.P.M.
POOSL: An object-oriented specification language for the analysis and design of hardware/software systems.
EUT Report 95-E-290. 1995. ISBN 90-6144-290-7

(291) Smeets, B.H.T. and M.H.J. Bollen
STOCHASTIC MODELLING OF PROTECTION SYSTEMS: Comparison of four mathematical techniques.
EUT Report 95-E-291. 1995. ISBN 90-6144-291-5

(292) Voeten, J.P.M. and A. van Rangelrooij
CCS AND TIME: A practical and comprehensible approach to a performance evaluation of finite state CCS descriptions.
EUT Report 95-E-292. 1995. ISBN 90-6144-292-3

(293) Voeten, J.P.M.
SEMANTICS OF POOSL: An object-oriented specification language for the analysis and design of hardware/software systems.
EUT Report 95-E-293. 1995. ISBN 90-6144-293-1

(294) Osch, A.W.H. van
MODELLING OF PRASEODYMIUM-DOPED FLUORIDE AND SULFIDE FIBRE AMPLIFIERS FOR THE 1.3 μM WAVELENGTH REGION.
EUT Report 95-E-294. 1995. ISBN 90-6144-294-X

(295) Bastiaans, Martin J.
GABOR'S EXPANSION AND THE ZAK TRANSFORM FOR CONTINUOUS-TIME AND DISCRETE-TIME SIGNALS: Critical sampling and rational oversampling.
EUT Report 95-E-295. 1995. ISBN 90-6144-295-8

(296) Blaschke, F. and A.J.A. Vandenput
REGELTECHNIEKEN VOOR DRAAIVELDMACHINES. (Control of AC machines, in Dutch)
2 Volumes. Vol. 1: TEKST (Text). Vol. 2: FIGUREN (Figures).
EUT Report 96-E-296. 1996. ISBN 90-6144-296-6

(297) Dolmans, G.
DIVERSITY SYSTEMS FOR MOBILE COMMUNICATION IN A LARGE ROOM.
EUT Report 96-E-297. 1996. ISBN 90-6144-297-4